

第 12 回 核燃焼プラズマ 統合コード研究会

12th Burning Plasma Simulation Initiative (BPSI) Meeting

日時：2014年12月11日(木)–12日(金)
場所：九州大学筑紫キャンパス
応用力学研究所 2階大会議室



第 12 回核燃焼プラズマ統合コード研究会

12th Burning Plasma Simulation Initiative (BPSI) Meeting

(Ver.2)

日時：2014年12月11日(木)–12日(金)

場所：九州大学筑紫キャンパス 応用力学研究所 2階大会議室

(18 min talk+7 min discuss or 15min talk+5min discuss)

12月11日(木)

9:00 – 9:10 はじめに 福山 (京大)

(座長：矢木)

9:10 – 9:35 講演 1-1 滝塚 (阪大)

On the Fluid Modeling of Neutral Particle Transport in a SOL Plasma

9:35 – 10:00 講演 1-2 河村 (核融合研)

Transport Modeling of Peripheral Plasma in the Open/Closed LHD
Divertor Configurations

10:00 – 10:25 講演 1-3 本間 (慶大)

Kinetic Modeling of Classical and Neo-Classical Transport for High-Z
impurities in Fusion SOL/Divertor Plasmas using Binary Collision
Method

10:25 – 10:45 講演 1-4 東郷 (東大)

Simulation Study of SOL-Divertor Plasmas Using a Virtual Divertor
Model

10:45 – 11:00 休憩

(座長：河村)

11:00 – 11:25 講演 1-5 登田 (核融合研)

How to Apply a Turbulent Transport Model Based on a Gyrokinetic
Simulation for Helical Plasmas

11:25 – 11:50 講演 1-6 村上 (京大)

Integrated Transport Simulation of High Ti LHD Plasmas by TASK3D

11:50 – 12:50 昼休み

(座長：福山)

12:50 – 13:15 講演 2-1 藤間 (原子力機構)

Integrated Simulation with the Fast Ion Fokker-Planck Modeling

Consistent with the Evolving Equilibrium in Tokamaks

13:15 – 13:40 講演 2-2 奴賀 (原子力機構)

Fokker-Planck Simulation of the Runaway Electron Generation in Tokamak Disruption

13:40 – 14:05 講演 2-3 Lesur (九大)

Hybrid, Reduced Modeling of Coupled Energetic-Particle Modes

14:05 – 14:30 講演 2-4 佐々木 (九大)

Formation Mechanism of Steep Wave Front in Magnetized Plasmas

14:30 – 14:45 休憩

(座長 : 村上)

14:45 – 15:10 講演 2-5 林 (原子力機構)

Integrated Modeling of JT-60SA Plasma Operation Scenarios with Model Validation and Verification

15:10 – 15:35 講演 2-6 糟谷 (九大)

Simulation Study of Hysteresis in the Flux-Gradient Relation Responding to a Source Modulation

15:35 – 16:00 講演 2-7 河野 (九工大)

Radio-Frequency Sheath-Plasma Interactions in a Semi-Realistic Tokamak Model

16:00 – 16:20 講演 2-8 山口 (京大)

NBI Heating Analysis in Multi-Ion Species Plasma in LHD

16:20 – 16:35 休憩

(座長 : 登田)

16:35 – 17:00 講演 2-9 瀬戸 (原子力機構)

Development of L-H Transition Simulation Framework with BOUT++ Code

17:00 – 17:25 講演 2-10 大澤 (九大)

Isotope Effect of Hydrogen in Tungsten

17:25 – 17:45 講演 2-11 服部 (九大)

Analysis of Ion-Temperature-Gradient Instabilities by Using a Gyro-Fluid Model in Cylindrical Plasmas

17:45 散会

19:30 – 22:00 懇親会 (浪漫座雑餉隈店にて)

12月12日(金)

9:00 – 9:05 事務連絡

(座長：糟谷)

9:05 – 9:30 講演 3-1 藤田 (名大)

Simulation on Tungsten Transport and Sawtooth Control in Tokamak Plasmas with TOTAL Code

9:30 – 9:55 講演 3-2 本多 (原子力機構)

Toroidal Rotation Modeling with the 3D Non-Local Drift-Kinetic Code and Boundary Models for JT-60U Analyses and Predictive Simulations

9:55 – 10:20 講演 3-3 小菅 (九大)

Density Peaking by Parallel Flow Shear Driven Instability

10:20 – 10:35 休憩

(座長：藤田)

10:35 – 11:00 講演 3-5 矢木 (原子力機構)

Progress on Disruption Research by Integrated Simulation

11:00 – 11:25 講演 3-6 福山 (京大)

Progress of Integrated Modeling Code TASK

11:25 – 11:50 講演 3-7 横山 (核融合研)

Statistical Approach for Predicting Energy Transport in LHD Plasmas Based on the TASK3D-a Analyses Database

11:50 – 12:00 まとめ 矢木

12:00 – 13:00 昼休み

13:00 – 17:00 核融合エネルギーフォーラムサブクラスター会合

17:00 散会

On the Fluid Modeling of Neutral Particle Transport in a SOL Plasma

T. Takizuka¹, S. Togo², Y. Ogawa²

¹ Graduate School of Engineering, Osaka University

² Graduate School of Frontier Sciences, University of Tokyo

Comprehensive divertor simulation codes generally employ the kinetic Monte-Carlo model for neutral particles. Although the fluid model is much cheaper in the computational cost, benchmarking between kinetic and fluid models has shown remarkable discrepancy. We study how the diffusion coefficient of neutrals is determined in the fluid modeling, and propose a reduction of diffusion due to the spatial loss of neutrals. The reduced diffusion can explain the difference between kinetic and fluid models in the previous benchmarking.

1. Introduction

Divertor simulations are inevitable to design divertor systems with the reliable particle and heat control in magnetic fusion DEMO reactors. The edge plasma including SOL-divertor region in DEMO reactors will become much higher in temperature, density and heat flux compared with that in present machines. Therefore simulations bear an important role to extrapolate plasma conditions from the present machines to the DEMO reactors. Divertor simulation codes have been developed and widely utilized for the above sake. Comprehensive divertor codes generally couple the fluid modeling for edge plasma and the kinetic Monte-Carlo (MC) modeling for neutral particles, e.g., SOLPS combines B2 and EIRENE [1], and SONIC combines SOLDOR and NEUT2D [2,3].

Although the kinetic MC modeling is able to describe well behaviors of neutral particles in an edge plasma, the computational cost is rather expensive compared with the fluid modeling for edge plasma itself. The MC noise is also a delicate matter. When a simulation shows interestingly an oscillating phenomenon in SOL-divertor plasmas, we are sometimes in doubt whether this phenomenon is really based on physics or only derived by numerical noises. It is worth to apply another modeling without MC technique for neutral particles. The fluid modeling for neutral particles is much cheaper than the kinetic MC modeling or the Boltzmann-equation modeling. In an edge plasma, neutral particles suffer various collisions; elastic collision, excitation collision, ionization collision, and charge-exchange collision. Considering the nature of charge-exchange collision, the transport of neutral particles has been approximated by the diffusion model, $\partial N_0/\partial t = \nabla(D_0 \nabla N_0) - \nu_{iz} N_0 + S$, where N_0 is the neutral density, D_0 is the diffusion coefficient, ν_{iz} is the ionization frequency, and S is the source [4]. First-flight neutrals emitted from the wall can be separately modeled as $\partial N_0^{(1)}/\partial t + V_{FC} \nabla N_0^{(1)} = -\nu_{iz} N_0^{(1)} - \nu_{cx} N_0^{(1)}$, where the superscript (1) denotes the first-flight neutral component, V_{FC} is a Frank-Condon speed, and the charge-exchange sink term $-\nu_{cx} N_0^{(1)}$ is transposed to a part of the source term S for the diffused neutrals (ν_{cx} is the charge-exchange frequency) [5].

Benchmarking of the kinetic MC model and the fluid model for neutral transport in tokamak SOL-divertor region has been carried out. Unexpectedly large differences of the benchmark results have been found [6,7]. Neutral particles for the fluid modeling spread broader in the radial direction near the divertor plate compared with those for the kinetic modeling, as was shown by Fig. 3(d) in [6].

In the present paper, we study how the diffusion coefficient D_0 is determined, and propose a reduction of diffusion due to the spatial loss of neutrals. The reduced diffusion can explain the difference between kinetic and fluid models in the previous benchmarking.

2. Diffusion equation for the neutral particle transport

Neutral particles suffer charge-exchange (CX) collisions between back-ground ions with temperature

T_i , and their velocities are distributed randomly at every CX collision. Resultantly the nature of neutral particle transport becomes diffusive. At first we consider the following random-walk model in a one-dimensional (1D) system;

$$N_0(x, t + \tau_{cx}) = \exp(-v_{iz}\tau_{cx}) \{N_0(x + \lambda_{cx}, t) + N_0(x - \lambda_{cx}, t)\}/2. \quad (1)$$

Here the density of neutrals N_0 is counted discretely in time t and space x with a time step of the CX collision time $\tau_{cx} = 1/v_{cx}$ and a step size of the CX mean-free path $\lambda_{cx} = v_0\tau_{cx}$ ($m_i v_0^2 = T_i$). The ionization process is described by the exponential decay during τ_{cx} . This equation is approximately translated into a diffusion equation;

$$\partial N_0/\partial t = D_0 \partial^2 N_0/\partial x^2 - v_{iz}N_0 \quad (2)$$

where a diffusion coefficient is given as

$$D_0 = D_0^{(RW)} = v_0^2/2(v_{iz} + v_{cx}). \quad (3)$$

Note that the diffusion coefficient $D_0^{(RW)}$ is given not as $\lambda_{cx}^2/2\tau_{cx}$ but as $\lambda_{cx}^2/2\tau_{cx}(1 + v_{iz}\tau_{cx})$.

Next we consider a two-component model similar to the model in Ref. [8]. The number densities for two groups, F_+ and F_- are treated; F_+ has a positive velocity v_0 and F_- has a negative velocity $-v_0$;

$$\partial F_+/\partial t + v_0 \partial F_+/\partial x = -v_{iz}F_+ - v_{cx}F_+ + v_{cx}(F_+ + F_-)/2 \quad (4a)$$

$$\partial F_-/\partial t - v_0 \partial F_-/\partial x = -v_{iz}F_- - v_{cx}F_- + v_{cx}(F_+ + F_-)/2 \quad (4b)$$

where F_+ and F_- are randomly re-distributed by the CX reactions. Using a relation $N_0 = F_+ + F_-$ and introducing $\Delta F = F_+ - F_-$, we rewrite Eqs. (4a) and (4b) as $\partial N_0/\partial t + v_0 \partial \Delta F/\partial x = -v_{iz}N_0$ and $\partial \Delta F/\partial t + v_0 \partial N_0/\partial x = -(v_{iz} + v_{cx})\Delta F$. Assuming $\partial \Delta F/\partial t \ll (v_{iz} + v_{cx})\Delta F$, we obtain a diffusion equation of the same form as Eq. (2). The diffusion coefficient in this case, however, is derived two times larger than $D_0^{(RW)}$;

$$D_0 = D_0^{(TC)} = v_0^2/(v_{iz} + v_{cx}) \quad (5)$$

We examine which is reliable $D_0^{(RW)}$ or $D_0^{(TC)}$ for the neutral transport model. The momentum equation is considered in addition to the continuity equation [9,10];

$$\partial N_0/\partial t + \partial(N_0V)/\partial x = -v_{iz}N_0 \quad (6a)$$

$$\partial(N_0V)/\partial t + \partial(N_0V^2)/\partial x = -\partial(N_0v_0^2)/\partial x - (v_{iz} + v_{cx})N_0V \quad (6b)$$

where V is the mean flow velocity of neutrals but the back-ground-ion flow is supposed zero for simplicity. Adopting major terms in Eq. (6b), $(v_{iz} + v_{cx})N_0V = -v_0^2 \partial N_0/\partial x$, we again obtain a diffusion equation of the same form as Eq. (2). For this case, the diffusion coefficient is just the same as that for two-component model;

$$D_0 = D_0^{(mom)} = v_0^2/(v_{iz} + v_{cx}). \quad (7)$$

We easily find that the two-component model and the fluid model with momentum equation are equivalent to each other, when putting $v_0 \Delta F = N_0V$. Some paper proposed a little smaller $D_0 = 8v_0^2/3\pi(v_{iz} + v_{cx})$ [11]. In order to find a correct value for $D_0 = C_D T_i/m_i(v_{iz} + v_{cx})$, benchmark calculations between the diffusion model and the kinetic MC model in a 1D slab system will be required.

3. Loss term in the diffusion equation

Loss term is very important in the diffusion equation for neutral particle transport;

$$\partial N_0/\partial t = \nabla(D_0 \nabla N_0) - v_{iz}N_0 - v_L N_0. \quad (8)$$

The loss term, $-v_L N_0$, works as fully the same as the ionization term, $-v_{iz}N_0$. Therefore the diffusion coefficient can be given by

$$D_0 = v_0^2 / (v_L + v_{iz} + v_{cx}) . \quad (9)$$

When the spatial loss rate is larger than the ionization loss rate and the CX rate, $v_L > v_{iz} + v_{cx}$, the diffusion becomes very small compared with the small-loss case. Note that particles are lost from the plasma surface, and there is no sink in a plasma except for the ionization. Loss term can be introduced for the reduced dimension.

We study the loss term for the reduced 1D system (x direction) by introducing a four-component model in two-dimensional (2D) system;

$$\partial F_{\pm\pm} / \partial t \pm v_0 \partial F_{\pm\pm} / \partial x \pm v_0 \partial F_{\pm\pm} / \partial y = -v_{iz} F_{\pm\pm} - v_{cx} F_{\pm\pm} + v_{cx} (F_{++} + F_{+-} + F_{-+} + F_{--}) / 4 \quad (10)$$

where subscript \pm corresponds to a group of positive/negative velocity. First subscript denotes x direction and second one denotes y direction as shown in Fig. 1. Four components $F_{\pm\pm}$ are randomly re-distributed by the CX reactions. Neutral particles escape from the plasma surface at $y = \pm d$. Averaging $F_{\pm\pm}$ inside $-d < y < d$ without reflection at the boundary, i.e., $F_{++} = 0$ at $y = -d$ and $F_{+-} = 0$ at $y = d$, Eq. (10) becomes 1D equations for averaged four components $F_{\pm\pm}$;

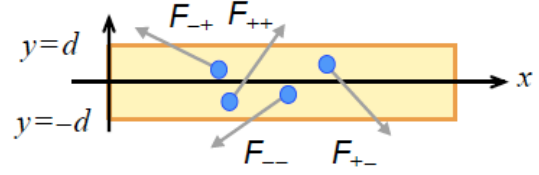


Fig. 1 Four components, F_{++} , F_{+-} , F_{-+} and F_{--} of neutrals in a SOL-divertor plasma.

$$\partial F_{\pm\pm} / \partial t \pm v_0 \partial F_{\pm\pm} / \partial x + (v_0 / 2d) F_{\pm\pm}(\pm d) = -v_{iz} F_{\pm\pm} - v_{cx} F_{\pm\pm} + v_{cx} (F_{++} + F_{+-} + F_{-+} + F_{--}) / 4 \quad (11)$$

Summing up y -direction components, $F_+ = F_{++} + F_{+-}$ and $F_- = F_{-+} + F_{--}$, Eq. (11) becomes two-component equations;

$$\partial F_+ / \partial t + v_0 \partial F_+ / \partial x + (v_0 / 2d) \{F_{++}(d) + F_{+-}(-d)\} = -v_{iz} F_+ - v_{cx} F_+ + v_{cx} (F_+ + F_-) / 2 \quad (12a)$$

$$\partial F_- / \partial t - v_0 \partial F_- / \partial x + (v_0 / 2d) \{F_{-+}(d) + F_{--}(-d)\} = -v_{iz} F_- - v_{cx} F_- + v_{cx} (F_+ + F_-) / 2 \quad (12b)$$

These equations are reduced to a diffusion equation with the same procedure in Section 2.

$$\partial N_0 / \partial t = D_0 \partial^2 N_0 / \partial x^2 - v_{iz} N_0 - (v_0 / 2d) \{F_{++}(d) + F_{+-}(-d) + F_{-+}(d) + F_{--}(-d)\} \quad (13)$$

The last term in RHS of Eq. (13) corresponds to the loss term $-v_L N_0$.

Now we estimate the loss rate v_L based on a simple continuity equation in the y -direction;

$$v_0 \partial F / \partial y = -v_{iz} F + S \quad (14)$$

For the case of point source S at $y = 0$, the profile of F is $F(0) \exp(-\kappa y)$ with a ionization decay length $\kappa^{-1} = v_0 / v_{iz}$, the average density is $N_0 = F(0) \{1 - \exp(-\kappa d)\} / \kappa d$, and the loss flux at $y = d$ is $\Gamma_L = F(0) v_0 \exp(-\kappa d)$. The loss rate defined by $v_L = \Gamma_L / N_0 d$ is then estimated as

$$v_L = (v_0 / d) (\kappa d) \exp(-\kappa d) / \{1 - \exp(-\kappa d)\} . \quad (15a)$$

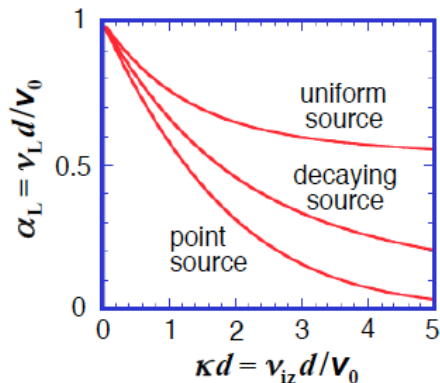


Fig. 2 Coefficient α_L of the loss rate as a Function of ionization decay factor κd for various source distribution.

When the source is uniform inside $-d < y < d$, the profile is $F = (S/\kappa v_0)\{1 - \exp(-\kappa(y + d))\}$ and the loss rate is estimated as

$$v_L = (v_0/d)(\kappa d)\{1 - \exp(-\kappa d)\}/[2\kappa d - \{1 - \exp(-2\kappa d)\}]. \quad (15b)$$

When the source is decaying linearly, $S_0(1 + y/d)$ inside $-d < y < 0$ and $S_0(1 - y/d)$ inside $0 < y < d$, the loss rate is estimated as

$$v_L = (v_0/d)\{1 - \exp(-\kappa d)\}^2/[\kappa d - (1/\kappa d)\{1 - \exp(-\kappa d)\}^2]. \quad (15c)$$

The loss rate can be described by a form $v_L = \alpha_L(v_0/d)$, and has to be added in the diffusion equation for neutral particle transport. The coefficient α_L is shown in Fig. 2 as a function of the ionization decay factor κd for the above three cases of source distribution. The reduction of D_0 due to this loss rate (see Eq. (9)) has also to be taken into account [12].

4. Discussion

In Section 3, the loss rate is studied for the 1D system. Even for the 2D system, D_0 could be smaller, and could have an anisotropic property. Simple consideration gives the following 2D diffusion model;

$$\partial N_0/\partial t = \partial/\partial x (D_x \partial N_0/\partial x) + \partial/\partial y (D_y \partial N_0/\partial y) - v_{iz}N_0 \quad (16)$$

where $D_x = v_0^2/(v_{Ly} + v_{iz} + v_{cx})$ and $D_y = v_0^2/(v_{Lx} + v_{iz} + v_{cx})$ with different loss rate $v_{Ly} = \alpha_{Ly}(v_0/d_y)$ and $v_{Lx} = \alpha_{Lx}(v_0/d_x)$. Diffusion of fluid neutrals is overestimated at the previous benchmarking, and N_0 near the strike point becomes lower while broadened outward compared with that calculated by the kinetic MC model. If D_0 is modeled smaller including the v_L effect, the fluid-modeling result could become similar to the kinetic-modeling result.

Acknowledgements

This work was partly supported by the Grant-in-Aid for Scientific Research (B) 24360382 from Japan Society for the Promotion of Science. The authors thank Dr. M. Nakamura, Dr. K. Hoshino, and Dr. K. Ibano for fruitful discussion about SOL-divertor simulations. One of authors, TT, is grateful to Prof. Y. Ueda of Osaka University for his continuous encouragement.

References

- [1] R. Schneider et al., *Contrib. Plasma Phys.* **46**, 3 (2006).
- [2] H. Kawashima, K. Shimizu, T. Takizuka, et al., *Plasma Fusion Res.* **1**, 031 (2006);
- [3] K. Shimizu, T. Takizuka, et al., *Nucl. Fusion* **49**, 065028 (2009).
- [4] E.L. Vold et al., *J. Nucl. Mater.* **176-177**, 570 (1990).
- [5] A.K. Prinja et al., *J. Nucl. Mater.* **196-198**, 340 (1992).
- [6] K. Hoshino et al., *Contrib. Plasma Phys.* **48**, 136 (2008).
- [7] D.P. Coster et al., *J. Nucl. Mater.* **337-339**, 366 (2005).
- [8] G. Kawamura et al., 7th BPSI meeting, Kasuga, 2008; 8th BPSI meeting, Kasuga, 2009.
- [9] F. Wising et al., *Contrib. Plasma Phys.* **36**, 309 (1996).
- [10] D.A. Knoll et al., *Phys. Plasmas* **3**, 293 (1996).
- [11] M. Honda, T. Takizuka, et al., *J. Plasma Fusion Res. SERIES* **9**, 529 (2010).
- [12] S. Togo, T. Takizuka, et al., "Simulation study using a virtual divertor model on the supersonic flow in SOL-divertor plasmas considering the anisotropic ion temperature", *proc. Plasma Conference 2014, Niigata (2014)* <http://www.jspf.or.jp/PLASMA2014/PLACON2014/pdf/20pC2-4.pdf>; "Simulation study of SOL-divertor Plasmas Using Virtual Divertor Model", in this *proc. 12th BPSI Meeting, Kasuga, 2014 (2015)*.

LHD 開ノ閉ダイバータに対する
周辺プラズマ輸送シミュレーションモデリング
Transport modeling of peripheral plasma
in the open/closed LHD divertor configurations

河村学思, 小林政弘, 庄司主, 森崎友宏, 増崎貴, 冯玉和*
Gakushi Kawamura, Masahiro Kobayashi, Mamoru Shoji,
Tomohiro Morisaki, Suguru Masuzaki, Yuhe Feng

核融合科学研究所 〒509-5292 岐阜県土岐市下石町 322-6
National Institute for Fusion Science, 322-6 Oroshi-cho Toki, Gifu 509-5292, Japan
*Max-Planck-Institut für Plasmaphysik, Greifswald Germany

Simulation modeling of the ergodic and divertor plasmas of the Large Helical Device (LHD) and its application to analysis of neutral particles, plasma, and impurity transport is presented. EMC3-EIRENE simulation with a new calculation mesh system is employed to evaluate effects of different divertor configurations: the open and the closed divertor. Effects of gas pumping were investigated to understand recycling. Difference of particle source which compensates the gas pumping is elucidated. Particle deposition in the core by NBI and palette causes significantly lower electron density in divertor regions than gas puffing. Impurity accumulation and impurity screening in the ergodic region were investigated and differences caused by the configurations are evaluated. The closed configuration causes large impurity accumulation but the impurity screening effect suppresses the accumulation at the same level as the open configuration.

Divertor configuration of Large Helical Device (LHD) has been modified to the closed one to control neutral transport and achieve efficient pumping. Evaluation of its effects on the plasma is an urgent issue. Different configurations lead to different transport and recycling and therefore investigations of global transport in realistic configuration are essential for understanding and control of the plasma. We employ EMC3-EIRENE code [1,2], which is a fluid code with Monte-Carlo technique and has the capability of resolving perpendicular transport across a magnetic field line in 3D space.

The peripheral plasma of the LHD has been modeled by EMC3-EIRENE code and simulation studies have been performed [3-5]. Modeling of LHD peripheral plasmas by fluid-description of parallel transport and diffusive terms of perpendicular transport are discussed in Ref. [3]. Extension of the simulation model to the closed divertor configuration [6] is realized. Effect of different divertor configurations on neutral gas pressure is investigated in Ref. [5]. We modeled a 1/20 toroidal block of the LHD plasma. The simulation region consists of plasma and vacuum regions and they cover every cross section of the vacuum vessel. The plasma mesh system of EMC3 covers the peripheral plasma which has long connection length, roughly >10m. The core region is excluded from the simulation and modeled as boundary conditions at the last closed flux surface (LCFS). The magnetic axis is located at $R_{ax}=3.6\text{m}$ and the vacuum field, i.e., zero beta value, is employed to make the mesh.

Cryopumps have been installed under the dome structure of the LHD and evaluation of their efficiency started in the 2013 experiment campaign. In order to know the effect of the gas pumping, we carried out simulations with pumps. We introduced pumping panels with zero reflection probability on the backside of the dome plates. We ignore the effect of wall-pumping to focus on the pumps. Particle source and sink must be balanced in the simulation box, and therefore we model two types of sources: gas-puffing and core fueling. In the actual device,

both of them exist in a discharge, but we employ the two extreme conditions of 100% gas-puffing and 100% core fueling. The gas puffing is implemented as an increase of recycling flux from the divertor plates in the code. Approximately 20% of neutral gas input is pumped out in both cases. That rate is roughly the maximum performance of the pumps determined by geometrical factors. Simulation parameters are as follows: input power, $P=8\text{MW}$, perpendicular particle and heat transport coefficients, $D=1\text{m}^2/\text{s}$, $c_e=c_i=3\text{m}^2/\text{s}$, electron density at LCFS, $n_e=2\times 10^{19}/\text{m}^3$.

Neutral gas pressure distribution in the closed configuration is given in Fig.1: (a) no pumping, (b) pumping and gas-puffing and (c) pumping and core fueling. The most obvious difference between them is the significant reduction of the pressure when the source is core fueling. That change is linked to the boundary condition of electron density. The core fueling increases the LCFS density directly if the perpendicular transport coefficient D is constant. The density is fixed as a boundary condition and therefore ionization source in the ergodic/divertor regions must be reduced. The difference between no pumping and pumping with gas-puffing is not clear in pressure distribution except under the dome, where the pressure is reduced to approximately 1/5.

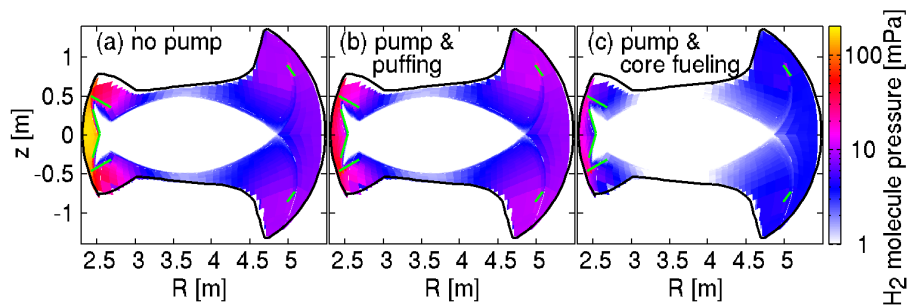


Fig. 1: Distribution of H₂ molecule pressure of the closed divertor configuration.

Figures 2(a) and (b) show distribution of electron density and temperature along $z=0$ line for three cases; without pump (red line), with pump and gas-puffing (green line), and with pump and core fueling (blue line). The gas-puffing condition causes almost the same plasma distribution as without the pump. That is a reasonable result because neutral particles pumped out are injected again and therefore the recycling flux does not change to sustain the same electron density at the LCFS. On the other hand, the core fueling condition causes significantly lower density and higher temperature by a factor of two in the outer region, $R>4.6\text{m}$. This is understood by increasing the plasma source in the core and decreasing recycling flux.

Figures 2(c) and (d) show distribution of H₂ molecules and H atoms. The difference between conditions without pump and with gas-puffing is not significant. Molecule and atom densities increase a little in this case, but how the density increases depends on measurement position. In fact, we observe an opposite result at a different position. This subtle difference arises from the different distribution of the neutral source. The change caused by core fueling is clear and not dependent on the measurement position. Molecule density decreases due to less recycling. Since the electron density becomes low, molecules can penetrate deeper into the ergodic plasma, and that causes increase of molecule density in the inner ergodic region, $R<4.8\text{m}$. The atom density and the total ionization source decrease.

We carried out a series of simulations in both configurations with carbon impurity. Gas pumping is switched off. We use a constant chemical sputtering yield, 1%, independent of plasma parameters and surface temperature. A sputtered carbon particle is a neutral atom and traced until it is ionized in the plasma. The impurity ion of each charge state is solved by fluid equation and the impurity temperature is the same as ion temperature.

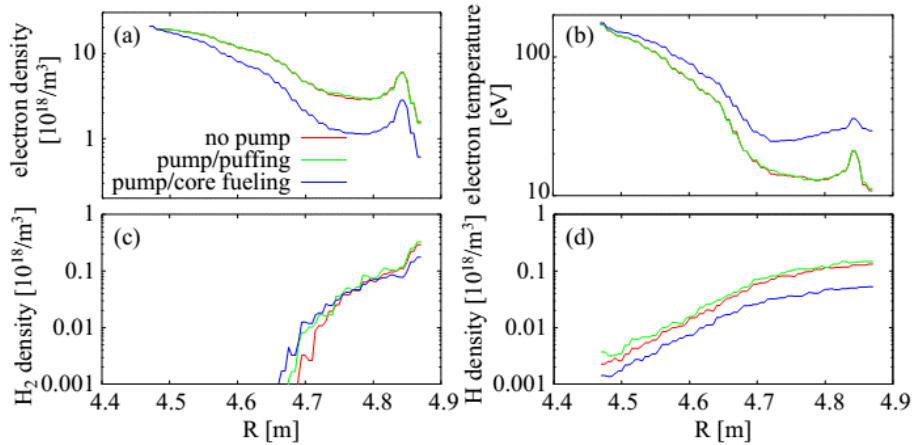


Fig. 2: Distributions of (a) electrons density, (b) temperature, (c) H₂ molecule density, and (d) H atom density along $z=0$ line on the horizontally elongated plane.

Figure 3 shows density distribution of carbon ions in low and high-density plasma with the same heating power. The carbon density is significantly reduced near the core in the high-density condition. That reduction is called “impurity screening” [4] in the ergodic region. The dominant forces acting on an impurity ion are friction force and thermal force. The former is proportional to particle parallel flux of the background plasma and normally has the direction toward divertor plates. The latter is proportional to temperature gradient of the plasma and normally has the direction toward upstream, i.e., the ergodic region. Flow distribution of impurity ions is determined by the balance of these forces in the plasma.

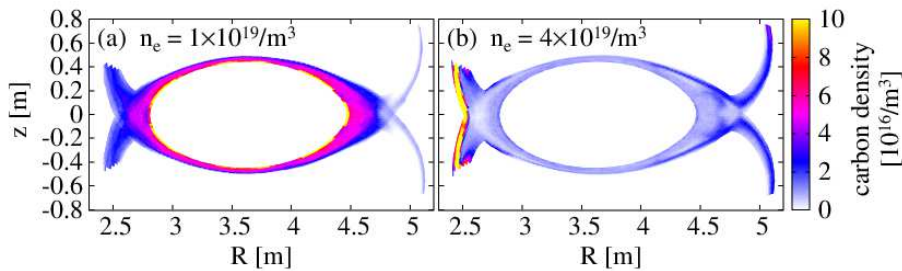


Fig. 3: Density distribution of carbon ions: (a) $n_e=1 \times 10^{19} \text{m}^{-3}$ (b) $n_e=4 \times 10^{19} \text{m}^{-3}$ at the LCFS. All the charge states of carbon are included.

The sputtering yield is fixed in simulations and therefore the amount of the erosion is proportional to the plasma flux on divertor plates. The impurity source in the plasma becomes large for high-density plasma and large carbon density is observed in divertor leg regions in our simulation. The impurity transport in the ergodic region is dominated by the force balance, as we mentioned. The closed configuration causes larger impurity generation due to large particle flux, but the transport toward the core region can be at the same level as the open configuration when the impurity screening occurs.

References

- [1] Y. Feng et al., *Contrib. Plasma Phys.* 44 (2004) 57.
- [2] D. Reiter et al., *Nucl. Fusion* 47 (2005) 172.
- [3] M. Kobayashi, et al., *Fusion Sci. Technol.* 58 (2010) 220.
- [4] M. Kobayashi et al., *Nucl. Fusion* 53 (2013) 033011.
- [5] G. Kawamura, et al., *Contrib. Plasma Phys.* 54 (2014) 437.
- [6] T. Morisaki, et al., *Nucl. Fusion* 53 (2013) 063014.

Kinetic modeling of classical and neo-classical transport for high-Z impurities in fusion SOL/Divertor plasmas using Binary Collision Method

12th Burning Plasma Simulation Initiative Meeting
(11-12, December, 2014.)

九州大学 筑紫キャンパス 応用力学研究所

Yuki Homma^{1,2}, Yu Sawada¹, Shohei Yamoto¹, Akiyoshi Hatayama¹

本間裕貴^{1,2}, 澤田悠¹, 矢本昌平¹, 畑山明聖¹

¹ Graduate School of Science and Technology, Keio University
3-14-1 Hiyoshi, Kohoku-ku, Yokohama, 223-8522, Japan

慶應義塾大学大学院理工学研究科 〒223-8522 神奈川県横浜市港北区日吉 3-14-1

² Research Fellowships for Young Scientists, Japan Society for the Promotion of Science
日本学術振興会特別研究員

Effects of the classical and neo-classical impurity transport across the magnetic \mathbf{B} -field in the Scrape-Off Layer (SOL) of fusion plasmas, have been studied with a new kinetic model using Binary Collision method (BCM). Our model is able to simulate the following two effects, which have been theoretically predicted but neglected in all the existing kinetic impurity transport simulations in the SOL/Divertor plasmas: (1) the inward pinch (IWP) due to density gradient of background plasmas and (2) the temperature screening effect (TSE, outward transport) caused by temperature gradient.

1. Introduction

Understanding of impurity transport in the SOL is one of the most important issues for developing fusion plasma devices, because of its strong influences (both negative/positive) on plasmas such as the radiation cooling. In our recent work [1-3], kinetic Monte Carlo models of IWP and TSE have been developed in the classical limit without toroidicity.

In this presentation, we have extended our model to be able to simulate the neo-classical inward pinch (NC IWP) and temperature screening effect (NC TSE) in a torus geometry. Such neoclassical (NC) radial transport is considered as one of the most important processes to determine impurity distribution in the plasma.

Then, the effect of open magnetic \mathbf{B} -field on the NC impurity transport has been investigated.

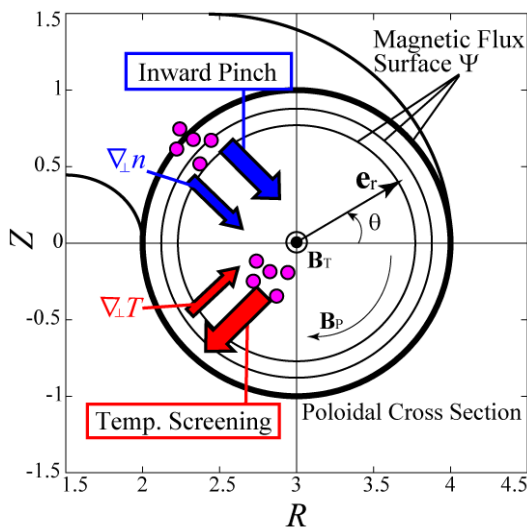


Fig. 1. A simple torus magnetic configuration

2. Neoclassical Transport Theory

In this study, we always suppose a simple torus \mathbf{B} -field: $B_T = -B_0 R_0 / R$, $B_P = \mu_0 I_p R_0 / 2\pi r R$, where B_T and B_P are the toroidal and poloidal component. Other symbols are conventional. Under such closed \mathbf{B} -field (i.e. the field line does not intersect with wall boundary), the radial flow velocity $\mathbf{v}_\perp^{\text{NC}}$ of impurity is estimated, from the neoclassical (NC) theory[4], as

$$\mathbf{v}_\perp^{\text{NC}} = (2q^2 n_z \nu_z T_i / e^2 B^2 Z) \cdot [K(n_i' / n_i - Z n_z' / n_z) + H T_i' / T_i] \cdot \mathbf{e}_r \quad (1)$$

The prime mark means the radial derivative.

Other symbols are conventional. In typical fusion plasmas, the numerical coefficients K and H are estimated as $K \sim 1$ and $H \sim (-1/2)$. In SOL/divertor region, radial gradients n_i' and T_i' are not always in the same direction, e.g. in detachment plasmas.

The IWP and TSE are not always canceled out each

other.

3. Numerical Model for Test Impurity Particle

Basic characteristics of the model are summarized as follows: (1) Full orbit of each test impurity particle is exactly solved by the equation of motion. (2) Coulomb collisions between impurities and background plasma ions are modeled by the Binary Collision Model (BCM) [5]. (3) In our BCM algorithm, the background ion velocities are randomly sampled from a distorted Maxwellian distribution representing the Pfirsch-Schluter regime which is typical in the SOL. Gradients of the background plasma density and temperature, which have been neglected in the conventional models, are included in our collision model.

4. Impurity Transport in the SOL plasma

Prior to the case of SOL plasma with open **B**-field, the model validation has been done by checking the IWP and TSE in a simple torus with closed **B**-field in Fig. 1. Background plasma ion is the deuterium (D^+) and impurity is the tungsten ion (W^{4+}). As a result (Fig. 2 (a)), it has been confirmed that impurity radial flow agrees well with the neo-classical theory Eq. (1).

Next, as shown in Fig. 2 (b,c,d), a limiter has been introduced in different position, inner / top / bottom, which produces the SOL region. We have applied our model to investigate whether the impurity transport in the SOL obeys the neo-classical law. It is not obvious because the **B**-field is *open* in the SOL (i.e. intersection with wall boundary).

A systematic test simulation of impurity transport across **B**-field has been performed for different limiter position and different gradients. Figure 2 (a,b,c,d) are the snapshots of simulated impurity profiles showing the TSE, without IWP. In the top and inner limiter case (Fig. 2 (b, d)), the average radial velocities are almost the same as in the closed magnetic flux case in Fig. 2 (a). This means that even in the open magnetic field, impurity transport across the magnetic field can be explained by NC theory. On the other hand, the average radial velocity and therefore flux disappears in case (c), i.e., outward TSE effect is very small in this case.

We have also performed similar test simulations for the IWP case, and confirmed that the IWP has been weakened with the top limiter. Such discrepancy between the simulation and the theory can be explained by the mechanisms of NC IWP and NC TSE.

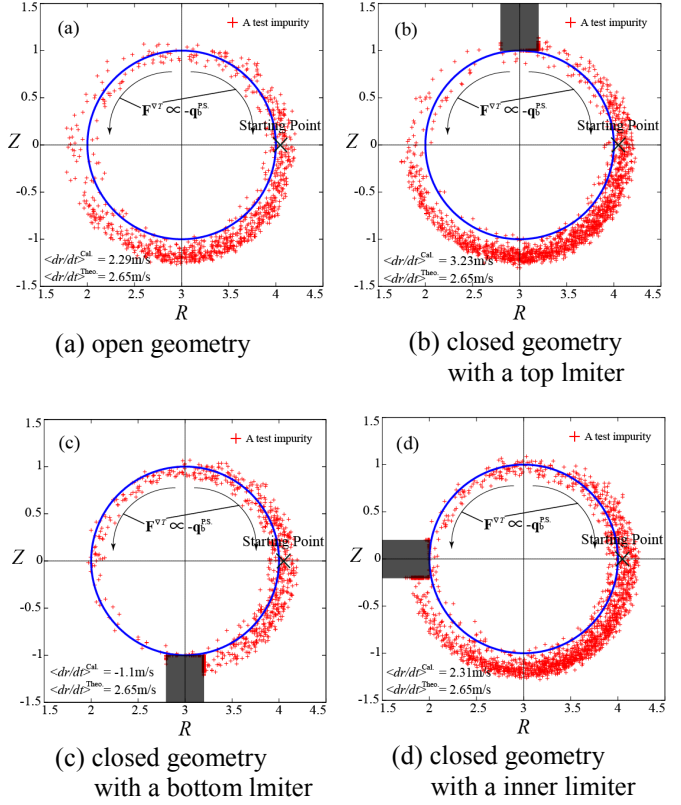


Fig. 2 Spatial distribution of test impurity ions in the torus geometry under a given background density and temperature gradient ($dn_b/dr=0$, $dT_b/dr=300\text{eV/m}$). In order to simulate the open magnetic configurations, the solid wall structure, which corresponds to so-called limiter or divertor plates, is installed for cases (b)-(d). Test ions have been launched at the same location (symbol:x) for all the cases.

6. Conclusion

We have developed a new numerical model for test impurity transport, which can take into account the neoclassical transport processes such as the inward pinch and the temperature screening effect.

As a result of test simulation in the open magnetic field geometries, we have confirmed that impurity transport can be strongly affected by the location of the wall structure.

References

- [1] Y. Sawada, M. Toma, Y. Homma, W. Sato, T. Furuta, S. Yamoto, A. Hatayama: Transactions of Fusion Science and Technology, **63**, 352 - 354 (2013).
- [2] Y. Homma, A. Hatayama: J. Comput. Phys., **231**, 3211-3227 (2012).
- [3] Y. Homma, A. Hatayama: J. Comput. Phys., **250**, 206-223 (2013).
- [4] D. Naujoks, K. Asmussen, M. Bessenrodt-Weberpals, *et al.*: Nucl. Fusion **36** 671 (1996).
- [5] T. Takizuka, H. Abe: J. Comput. Phys. **25** 205 (1977).

Simulation Study of SOL-Divertor Plasmas Using a Virtual Divertor Model

Satoshi Togo, Tomonori Takizuka^{a)}, Makoto Nakamura^{b)}, Kazuo Hoshino^{b)}, Yuichi Ogawa

Graduate School of Frontier Sciences, University of Tokyo, 5-1-5 Kashiwanoha, Kashiwa 277-8568, Japan

^{a)}Graduate school of Engineering, Osaka University, 2-1 Yamadaoka, Suita 565-0871, Japan

^{b)}Japan Atomic Energy Agency, 2-166 Omotedate, Obuchi-aza, O-aza, Rokkasho 039-3212, Japan

A one-dimensional (1D) SOL-divertor plasma simulation code with the virtual divertor (VD) model has been developed. In order to reproduce the effects of the divertor plate and the accompanying sheath in the SOL-divertor plasma fluid model, the VD model sets an artificial region beyond the divertor plates and sets artificial sinks for the particle, momentum and energy there in the image of a “waterfall”. In addition, the VD region makes the periodic boundary condition available and reduces the complexity of the algorithm. The self-consistent neutral model which matches the VD model is also developed.

1 Introduction

Reduction of the divertor heat load is one of the most important issues in order to commercialize the tokamak fusion reactors [1]. The SOL-divertor plasma code packages such as SOLPS [2] and SONIC [3] are widely used for designing the divertors or predicting the heat load on the divertor plates in the future tokamaks. The simulation results from these code packages for the SOL-divertor plasmas in the existing devices, however, include ones which do not agree satisfactorily with the experiments [4, 5].

The SOL-divertor codes solve the fluid equations for the plasma in general in stead of directly solving the Boltzmann equation for the distribution function from the computational cost point of view. There are some physics models in the plasma fluid model such as the boundary conditions and the heat conductions. The validation of such physics models by using the kinetic codes such as PARASOL (for example, [6–9]) is important.

The parallel momentum transport equation solved in many SOL-divertor plasma fluid codes has the second-order derivative parallel viscosity term which was derived under the assumption that the difference between the parallel and perpendicular components of the pressure of ion and electron (to the direction of the magnetic field) was much smaller than the pressure itself so that the pressure was almost isotropic [10]. In the open field system, however, the parallel component of the convective energy is larger than perpendicular one and the parallel temperature becomes lower than the perpendicular one. It is reported from the PARASOL’s results that the ion temperature anisotropy is remarkable even in the medium collisional regime [6, 9]. The generalized plasma fluid equations which distinguish the parallel temperature from the perpendicular one are proposed in such as [11, 12] but are not reported to be adopted in the SOL-divertor codes yet.

In many SOL-divertor plasma fluid codes, the boundary condition $M_t = 1$ (M_t is the Mach number at the divertor plate) is imposed in order to solve the parallel momentum transport equation which is a second-order partial differential equation (PDE). This boundary condition comes from the Bohm condition and requires the iteration which makes the algorithm complex in the codes. Moreover, the rigorous Bohm condition only imposes the lower limit of the Mach number at the divertor plate as $M_t \geq 1$ [13]. In addition, PARASOL reported that the plasma flow becomes supersonic at the divertor plate with the cooling effect [8].

We have been improving our one-dimensional (1D) SOL-divertor plasma code [14, 15] by introducing the anisotropic ion temperature, $T_{i,\parallel}$ and $T_{i,\perp}$, directly to the plasma fluid model [16]. It is assumed that the electron temperature is isotropic [6, 9]. This makes it possible to exclude the parallel ion viscosity term in the parallel momentum transport equation and to describe the equation as a first-order PDE [17]. Because of this, the boundary condition $M_t = 1$ becomes unnecessary to solve it. In order to reproduce the effects of the divertor plate and the accompanying sheath, the virtual divertor (VD) model is developed which sets an artificial region beyond the divertor plates and sets artificial sinks for the particle, momentum and energy there in the image of a “waterfall”. This VD region connects the calculation domain and makes the periodic boundary condition available reducing the complexity of the algorithm. Recently, we have constructed a self-consistent neutral model which matches the VD model. The equations for neutral can also be solved by using the periodic boundary condition.

In this paper, the numerical model is described in Sec. 2 and the results are shown in Sec. 3. In Sec.4, summary and discussion are described.

2 Numerical Model

2.1 Basic equations for plasma

The 1D fluid equations in the system of the homogeneous magnetic field are as follows;

$$\frac{\partial n}{\partial t} + \frac{\partial nV}{\partial s} = S \quad (1)$$

$$\frac{\partial m_i nV}{\partial t} + \frac{\partial}{\partial s} (m_i nV^2 + nT_{i,\parallel} + nT_e) = M_m \quad (2)$$

$$\begin{aligned} & \frac{\partial}{\partial t} \left(\frac{1}{2} m_i nV^2 + \frac{1}{2} nT_{i,\parallel} \right) \\ & + \frac{\partial}{\partial s} \left(\frac{1}{2} m_i nV^3 + \frac{3}{2} nT_{i,\parallel} V + c q_{i,\parallel}^{\text{eff}} \right) \\ & = Q_{i,\parallel} + \frac{n(T_{i,\perp} - T_{i,\parallel})}{\tau_{\text{rlx}}} + \frac{m_e n(T_e - T_{i,\parallel})}{m_i \tau_e} \\ & - V \frac{\partial nT_e}{\partial s} \end{aligned} \quad (3)$$

$$\begin{aligned} & \frac{\partial nT_{i,\perp}}{\partial t} + \frac{\partial}{\partial s} (nT_{i,\perp} V + (1-c) q_{i,\perp}^{\text{eff}}) \\ & = Q_{i,\perp} - \frac{n(T_{i,\perp} - T_{i,\parallel})}{\tau_{\text{rlx}}} + \frac{2m_e n(T_e - T_{i,\perp})}{m_i \tau_e} \end{aligned} \quad (4)$$

$$\begin{aligned} & \frac{\partial}{\partial t} \left(\frac{3}{2} nT_e \right) + \frac{\partial}{\partial s} \left(\frac{5}{2} nT_e V + q_e^{\text{eff}} \right) \\ & = Q_e + \frac{3m_e n(T_i - T_e)}{m_i \tau_e} + V \frac{\partial nT_e}{\partial s} \end{aligned} \quad (5)$$

Here, the symmetric SOL-divertor system is assumed. We omit the explanation of the notations here because they are the same as those in [16]. Here, we fix the heat flux limiter as $\alpha_{i,\parallel} = \alpha_{i,\perp} = 0.5$ and $\alpha_e = 0.2$ and $c = 0.5$, for simplicity. The relaxation time of ion temperature is assumed to be $\tau_{\text{rlx}} = 2.5\tau_i$ [11]. The sound speed is defined as $c_s = ((T_e + T_{i,\parallel})/m_i)^{1/2}$.

2.2 Virtual divertor model

The sheath theory imposes following physical boundary conditions at the divertor plate [13]; (a) the Mach number $M = V/c_s$ is equal to or larger than unity (the Bohm condition) and (b) the heat fluxes of ion and electron are given by $\gamma_i nT_i V$ and $\gamma_e nT_e V$, respectively, where γ_i and γ_e are the heat transmission factors. Because the parallel momentum transport equation, Eq. (2), is the first-order PDE, the Mach number at the divertor plate is determined only by the upstream condition while it is given as $M_t = 1$ in many SOL-divertor plasma codes. Instead of giving the Mach number at the divertor plate, we introduced the virtual divertor (VD) model in order to reproduce the effect of the divertor plate and the accompanying sheath. We set an artificial region beyond the divertor plate and set artificial sinks of particle, momentum and energy there in the image of a ‘‘waterfall’’ as follows;

$$S^{\text{VD}} = -\frac{n}{\tau_{\text{VD}}} \quad (6)$$

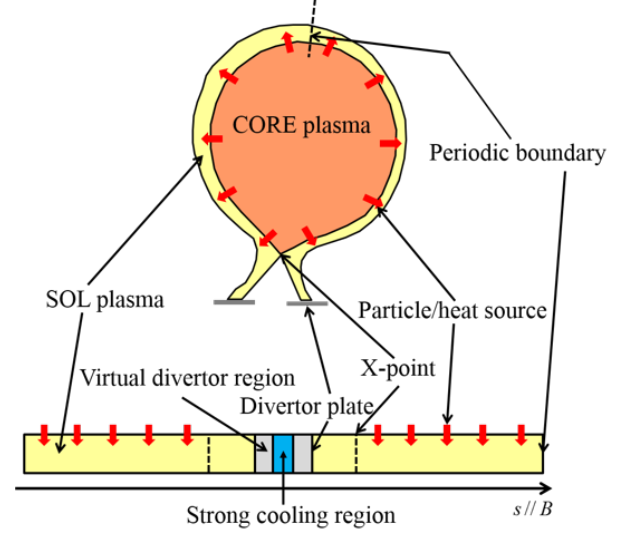


Fig. 1 Schematic of the SOL-divertor 1D system.

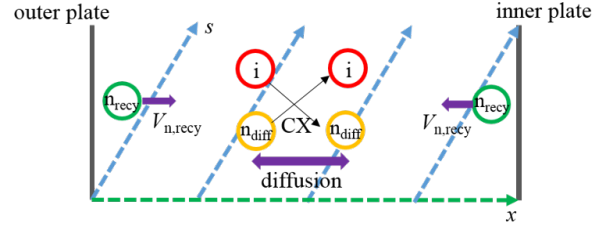


Fig. 2 Schematic of the neutral model.

$$M_m^{\text{VD}} = -\frac{m_i nV}{\tau_{\text{VD}}} + \frac{\partial}{\partial s} \left(\eta^{\text{VD}} \frac{\partial V}{\partial s} \right) \quad (7)$$

$$Q_{i,\parallel}^{\text{VD}} = -\frac{1}{\tau_{\text{VD}}} \left(\frac{1}{2} m_i nV^2 + g_{i,\parallel} \frac{1}{2} nT_{i,\parallel} \right) \quad (8)$$

$$Q_{i,\perp}^{\text{VD}} = -\frac{g_{i,\perp} nT_{i,\perp}}{\tau_{\text{VD}}} \quad (9)$$

$$Q_e^{\text{VD}} = -\frac{1}{\tau_{\text{VD}}} \left(g_e \frac{3}{2} nT_e \right) \quad (10)$$

The notations are the same as [16]. The VD region connects the calculation domain and the periodic boundary condition is available. Figure 1 shows the schematic of the SOL-divertor 1D system. The geometry used are also the same as [16].

2.3 Neutral model

Neutrals are divided into two kinds; the recycling neutrals generated at the divertor plate and transported by the convection at the constant velocity and the diffusion neutrals generated in the plasma and transported by diffusion by charge exchange. The recycling neutrals are further divided by which divertor plate (inner and outer) they are generated at. The schematic of the neutral model is shown in Fig. 2. The equations are as follows;

$$\begin{aligned} & \frac{\partial n_{n,\text{recy}}^{\text{in}}}{\partial t} + \frac{\partial n_{n,\text{recy}}^{\text{in}} V_{n,\text{recy}}^{\text{in}}}{\partial x} \\ &= -\frac{n_{n,\text{recy}}^{\text{in}}}{\tau_{n,\text{recy}}} - S_{\text{iz,recy}}^{\text{in}} - S_{\text{cx,recy}}^{\text{in}} \end{aligned} \quad (11)$$

$$\begin{aligned} & \frac{\partial n_{n,\text{recy}}^{\text{out}}}{\partial t} + \frac{\partial n_{n,\text{recy}}^{\text{out}} V_{n,\text{recy}}^{\text{out}}}{\partial x} \\ &= -\frac{n_{n,\text{recy}}^{\text{in}}}{\tau_{n,\text{recy}}} - S_{\text{iz,recy}}^{\text{out}} - S_{\text{cx,recy}}^{\text{out}} \end{aligned} \quad (12)$$

$$\begin{aligned} & \frac{\partial n_{n,\text{diff}}}{\partial t} + \frac{\partial}{\partial x} \left(-D_n \frac{\partial n_{n,\text{diff}}}{\partial x} \right) \\ &= -\frac{n_{n,\text{diff}}}{\tau_{n,\text{diff}}} - S_{\text{iz,diff}} + S_{\text{rc}} + S_{\text{cx,recy}} \end{aligned} \quad (13)$$

Here, the coordinate x is in the poloidal direction and $x = s \sin \theta$ where $\theta = B_p/B$ is the pitch angle which is assumed to be constant, for simplicity. The velocity of the recycling neutral is given as $V_{n,\text{recy}}^{\text{out}} = -V_{n,\text{recy}}^{\text{in}} = V_{\text{FC}}/2$ where $V_{\text{FC}} = (2\epsilon_{\text{FC}}/m_i)^{1/2}$ and the Franck-Condon energy $\epsilon_{\text{FC}} = 3.5$ eV. The diffusivity is determined as $D_n = T_i/m_i / (\nu_{\text{cx}} + \nu_{\text{iz}} + \nu_{n,\text{diff}})$. The radial loss times $\tau_{n,\text{recy}}$ and $\tau_{n,\text{diff}}$ are the input parameters. The source terms are defined as $S_{\text{iz,recy}}^{\text{in(out)}} = \langle \sigma v \rangle_{\text{iz}} n_{n,\text{recy}}^{\text{in(out)}} n_e$, $S_{\text{cx,recy}}^{\text{in(out)}} = \langle \sigma v \rangle_{\text{cx}} n_{n,\text{recy}}^{\text{in(out)}} n_i$, $S_{\text{iz,diff}} = \langle \sigma v \rangle_{\text{iz}} n_{n,\text{diff}} n_e$, $S_{\text{rc}} = \langle \sigma v \rangle_{\text{rc}} n_i n_e$ and $S_{\text{cx,recy}} = S_{\text{cx,recy}}^{\text{in}} + S_{\text{cx,recy}}^{\text{out}}$ where n_i and n_e are the density of the ion and electron and $n_i = n_e = n$ for the charge neutrality.

In the VD region, we use the following equations;

$$\frac{\partial n_{n,\text{recy}}^{\text{in}}}{\partial t} + \frac{\partial n_{n,\text{recy}}^{\text{in}} V_{n,\text{recy}}^{\text{in}}}{\partial x} = \eta_0 \frac{n}{\tau_{\text{VD}}} + \eta_2 \frac{n_{n,\text{diff}}}{\tau_{n,\text{diff}}} \quad (14)$$

$$\frac{\partial n_{n,\text{recy}}^{\text{out}}}{\partial t} + \frac{\partial n_{n,\text{recy}}^{\text{out}} V_{n,\text{recy}}^{\text{out}}}{\partial x} = \eta_0 \frac{n}{\tau_{\text{VD}}} + \eta_2 \frac{n_{n,\text{diff}}}{\tau_{n,\text{diff}}} \quad (15)$$

$$\frac{\partial n_{n,\text{diff}}}{\partial t} + \frac{\partial}{\partial x} \left(-D_n \frac{\partial n_{n,\text{diff}}}{\partial x} \right) = -\frac{n_{n,\text{diff}}}{\tau_{n,\text{diff}}} \quad (16)$$

The terms in the RHS of Eq. (14) (Eq. (15)) become zero in the region of $V < 0$ ($V > 0$) for the first term and $\partial n_{n,\text{diff}}/\partial x > 0$ ($\partial n_{n,\text{diff}}/\partial x < 0$) for the second term. The decay time for the diffusion neutral in the VD region $\tau_{n,\text{diff}}^{\text{VD}}$ is an input parameter. These equations are also solved by the periodic boundary condition.

2.4 Source terms

The source terms for the plasma are summarized as follows;

$$S = S^{\text{core}} + S_{\text{iz}} - S_{\text{rc}} \quad (17)$$

$$\begin{aligned} M_{\text{m}} &= \frac{1}{2} m_i V_{\text{FC}} \sin \theta \left(S_{\text{iz,recy}}^{\text{out}} - S_{\text{iz,recy}}^{\text{in}} \right) \\ &+ \frac{1}{2} m_i V_{\text{FC}} \sin \theta \left(S_{\text{cx,recy}}^{\text{out}} - S_{\text{cx,recy}}^{\text{in}} \right) \\ &- m_i V \left(S_{\text{cx}} + S_{\text{rc}} \right) \end{aligned} \quad (18)$$

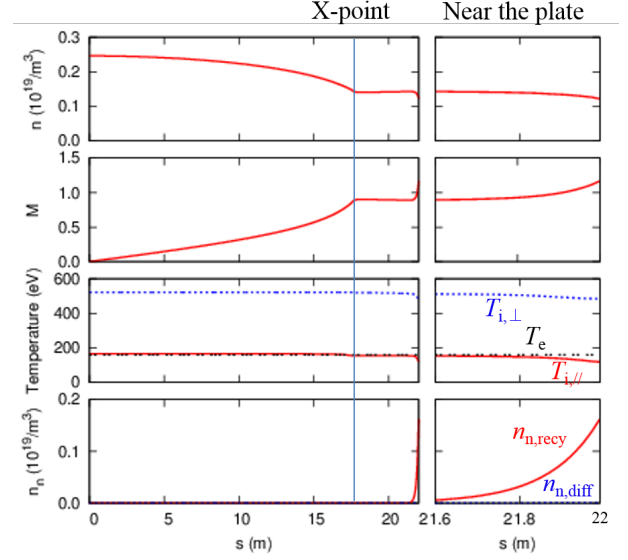


Fig. 3 Profiles of the parameters for the low recycling case.

$$\begin{aligned} Q_{i,\parallel} &= Q_{i,\parallel}^{\text{core}} + \frac{T_i}{2} (S_{\text{iz,diff}} + S_{\text{cx,diff}}) \\ &+ \frac{1}{6} m_i V_{\text{FC}}^2 (S_{\text{iz,recy}} + S_{\text{cx,recy}}) \\ &- \left(\frac{1}{2} m_i V^2 + \frac{1}{2} T_{i,\parallel} \right) (S_{\text{cx}} + S_{\text{rc}}) \end{aligned} \quad (19)$$

$$\begin{aligned} Q_{i,\perp} &= Q_{i,\perp}^{\text{core}} + T_i (S_{\text{iz,diff}} + S_{\text{cx,diff}}) \\ &+ \frac{1}{3} m_i V_{\text{FC}}^2 (S_{\text{iz,recy}} + S_{\text{cx,recy}}) \\ &- T_{i,\perp} (S_{\text{cx}} + S_{\text{rc}}) \end{aligned} \quad (20)$$

$$Q_e = Q_e^{\text{core}} - \epsilon_{\text{iz}} S_{\text{iz}} - \frac{3}{2} T_e S_{\text{rc}} \quad (21)$$

Here, $\epsilon_{\text{iz}} = 30$ eV is used.

3 Results

In the previous paper [16], we showed the simulation results without neutrals. The relation between the anisotropy of ion temperature and the normalized mean free path of ion was investigated and agreed well with the kinetic result [9]. The Bohm condition was satisfied for the collisional and weakly collisional cases. The direct comparison between viscous flux and the stress tensor was also carried out.

In the present paper, we present shortly the simulation results including the neutral model. Figure 3 shows the profiles of the plasma parameters for a low recycling case (recycling ratio of 0.05) and Fig. 4 for a high recycling case (recycling ratio of 0.7). Input parameters are as follows; parallel connection length $L = 44$ m, SOL width $d = 2$ cm, particle flux from the core to SOL region $\Gamma_{\text{sep}} = 1 \times 10^{22}$ /s and heat flux from the core $P_{\text{sep}} = 3$ MW. In the low recycling case, the Mach number at the divertor plate becomes larger than unity. The ion temperature anisotropy $T_{i,\parallel}/T_{i,\perp}$

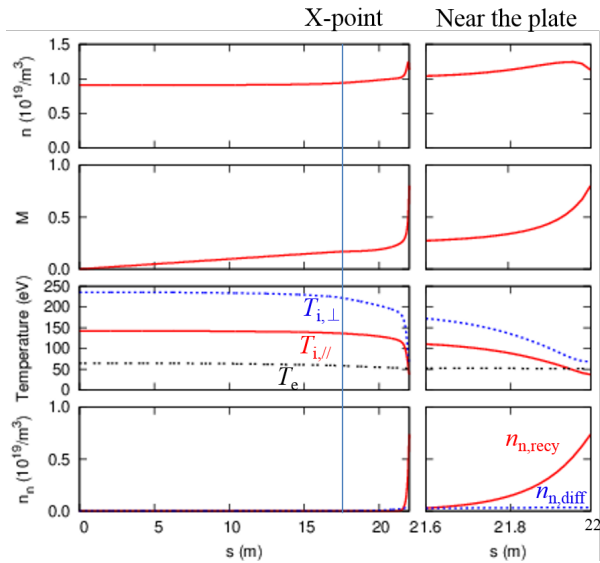


Fig. 4 Profiles of the parameters for the high recycling case.

is about 0.3. In the high recycling case, the Mach number at the divertor plate becomes lower than unity. This may be caused by the strong particle source near the divertor plate. The ion temperature anisotropy $T_{i,\parallel}/T_{i,\perp}$ is about 0.6. For the both cases, the recycling neutral is dominant.

4 Summary and Discussion

A 1D SOL-divertor plasma simulation code with the VD model has been developed. In order to reproduce the effects of the divertor plate and the accompanying sheath in the SOL-divertor plasma fluid model, the VD model sets an artificial region beyond the divertor plates and sets artificial sinks for the particle, momentum and energy there in the image of a “waterfall”. In addition, the VD region makes the periodic boundary condition available and reduces the complexity of the algorithm. The self-consistent neutral model which matches the VD model is also developed. Simulation results and discussions without neutrals are shown in [16]. In this paper, Simulation results including the neutral model are shown for the low and high recycling cases.

For the present study, the homogeneous magnetic field and the symmetric inner/outer SOL-divertor systems are assumed for simplicity. In order to simulate the inhomogeneous magnetic field and the asymmetric SOL-divertor systems, the effects of the mirror force and the plasma current have to be considered. The value of c does not make significant differences in the present study because the convective heat flux is dominant but it might be important in the higher recycling or the detached cases. These are our future works.

Acknowledgement

We would like to thank Dr. Shimizu of Japan Atomic Energy Agency (JAEA) for helpful advice on the numerical calculations and Dr. A. Okamoto of Tohoku University and Dr. K. Ibano of Osaka University for fruitful discussions. This work is partially supported by a Grant-in-Aid for Scientific Research from Japan Society for the Promotion of Science (JSPS).

References

- [1] ITER Physics Expert Group on Divertor, Nucl. Fusion **39** (1999) 2391.
- [2] R. Schneider *et al.*, Contrib. Plasma Phys. **46** (2006) 3.
- [3] H. Kawashima *et al.*, Plasma Fusion Res. **1** (2006) 031.
- [4] A. V. Chankin *et al.*, J. Nucl. Mater. **390-391** (2009) 319.
- [5] M. Wischmeier *et al.*, J. Nucl. Mater. **415** (2011) S523.
- [6] T. Takizuka *et al.*, J. Nucl. Mater. **128-129** (1984) 104.
- [7] T. Takizuka and M. Hosokawa., Contrib. Plasma Phys. **40** (2000) 3-4, 471.
- [8] T. Takizuka *et al.*, J. Nucl. Mater. **290-293** (2001) 753.
- [9] A. Froese *et al.*, Plasma Fusion Res. **5** (2010) 026.
- [10] S. I. Braginskii, *Review of Plasma Physics*, Consultants Bureau (New York, 1965) **1** 205.
- [11] E. Zawaideh *et al.*, Phys. Fluids **29** (1986) 463.
- [12] W. Fundamenski, Plasma Phys. Control. Fusion **47** (2005) R163.
- [13] P. C. Stangeby, *The Plasma Boundary of Magnetic Fusion Devices*, Institute of Physics Publishing (Bristol and Philadelphia 1999).
- [14] M. Nakamura *et al.*, J. Nucl. Mater. **415** (2011) S553.
- [15] S. Togo *et al.*, Plasma Fusion Res. **8** (2013) 2403096.
- [16] S. Togo *et al.*, J. Nucl. Mater. (2015) *in Press*.
- [17] R. V. Bravenec *et al.*, Phys. Fluids **25** (1982) 608.

How to apply a turbulent transport model based on a gyrokinetic simulation for helical plasmas

S. Toda¹, M. Nunami¹, A. Ishizawa¹, T. -H. Watanabe² and H. Sugama¹

¹*National Institute for Fusion Science, Oroshi-cho 322-6, Toki, Gifu, 509-5292, Japan*

²*Department of Physics, Nagoya University, Furo-cho, Nagoya, Aichi, 464-8602, Japan*

Turbulent transport is one of the most critical issues for plasma confinement in magnetic fusion devices. Recently, a large number of the gyrokinetic simulations have been done in toroidal plasmas [1]. The GKV-X code solving the gyro-kinetic equation has been used to examine the ITG mode and zonal flows in the LHD for studying the turbulent transport in helical plasmas [2]. The reduced model of $\chi_i \sim \rho_{ti}^2 v_{ti} f(\mathcal{L}, \tilde{\tau}_{ZF})/R$ is taken [3] using the GKV-X code for the high- T_i LHD discharge of the shot number 88343. Here, \mathcal{L} is the mixing length estimate $\tilde{\gamma}_{\tilde{k}_y}/\tilde{k}_y^2$ integrated over the \tilde{k}_y space, where $\tilde{\gamma}_{\tilde{k}_y}$ is the normalized linear growth rate of the ITG mode and $\tilde{\tau}_{ZF}$ is the normalized decay time of zonal flows [4, 5]. However, it is costly to carry out linear calculations of the growth rate by the gyrokinetic simulation at each time step of the dynamical transport code such as TASK3D [6], because the transport analysis of helical plasmas demands a high radial resolution so as to accurately evaluate the radial electric field and the field configuration. In this study, how to apply the reduced model of the turbulent heat diffusivity for the ITG mode derived from the gyrokinetic simulation to the transport code is shown with a low computational cost. Modeling of the term \mathcal{L} in the reduced model for the ITG mode is necessary to be involved with a parameter dependence of the plasma instability in the dynamical transport code. The ion temperature gradient scale length $L_{T_i} (= -T_i/(\partial T_i/\partial r))$ is chosen for the parameter to apply \mathcal{L} to avoid the linear gyrokinetic analysis at each time step of the transport simulation. The field configuration is fixed at the initial state in the transport simulation. We have developed the formula for \mathcal{L} in terms of L_{T_i} . The decay time of zonal flows depends on the magnetic field configuration and is independent of the plasma profile. The formula of the zonal flow decay time is needed to be calculated only at the initial state. The calculation by substituting these formulae for \mathcal{L} and $\tilde{\tau}_{ZF}$ to the reduced model [3] reproduces the results of the reduced model itself within allowable errors. The computational cost to obtain the value of the turbulent ion heat diffusivity by this modeling at each time step of the transport simulation is much smaller than that of the linear gyrokinetic simulation. This additional modeling is applied to the transport code and enables us to study the simulation results with the experimental results in LHD.

Firstly, the linear analysis is done using the GKV-X code for the additional modeling of the turbulent ion heat diffusivity. The ITG instability is examined in the high- T_i LHD discharge #88343 [7]. The value of the turbulent ion heat diffusivity $\chi_i^{(1)}/\chi_i^{GB}$ was fitted [3] only by the function $\mathcal{L} (\equiv \int (\tilde{\gamma}_{\tilde{k}_y}/\tilde{k}_y^2) d\tilde{k}_y)$ as $\chi_i^{(1)}/\chi_i^{GB} = C_0 (C_T \mathcal{L})^\delta$, where χ_i^{GB} is the gyroBohm diffusivity, $\tilde{\gamma} = \gamma/(v_{ti}/R)$ and $\tilde{k}_y = k_y \rho_{ti}$. A reduced model for the ITG turbulent heat diffusivity in terms of the functions \mathcal{L} and $\tilde{\tau}_{ZF} (= \tau_{ZF}/(R/v_{ti}))$ was obtained as $\chi_i^{(2)}/\chi_i^{GB} = A_1 \mathcal{L}^\alpha / (A_2 + \tilde{\tau}_{ZF}/\mathcal{L}^{1/2})$. The numerical coefficients are given in [3]. The characteristic length of the ion temperature gradient is considered to be the important parameter for the ITG instability. As the function of L_{T_i} , the parameter \mathcal{L} is

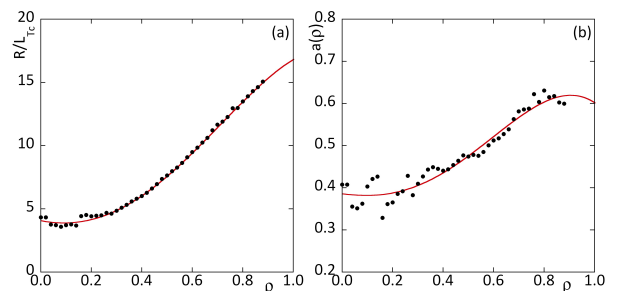


Figure 1: The radial dependence of (a) R/L_{T_e} and (b) $a(\rho)$ is shown with filled circles.

modeled by

$$\mathcal{L} = a(\rho) \left(\frac{R}{L_{T_i}} - \frac{R}{L_{T_c}} \right), \quad (1)$$

where L_{T_c} is the normalized critical ion temperature gradient for the ITG instability. To examine the critical ion temperature gradient for the ITG mode, the dependence of \mathcal{L} on R/L_{T_i} is examined [8] with all plasma parameters fixed except the ion temperature gradient. The density and ion temperature profiles are obtained from the experimental results at $t = 2.233$ s in the high- T_i LHD discharge #88343. The T_e profile is set as $T_e = T_i$ in a gyrokinetic simulation. We calculate the linear fitting function (1) at each radial point and obtain the values of R/L_{T_c} . The critical ion temperature gradient for the ITG mode, (a) R/L_{T_c} and the slope (b) $a(\rho)$ in terms of R/L_{T_i} are obtained in figure 1. When we calculate the value of the ion heat diffusivity in the integrated transport code, the fitting polynomials of R/L_{T_c} and $a(\rho)$ are used as $R/L_{T_c} = 4.0929 - 3.7681\rho + 19.712\rho^2 + 11.087\rho^3 - 14.272\rho^4$ and $a(\rho) = 0.38661 - 0.070919\rho + 0.2571\rho^2 + 0.95949\rho^3 - 0.92978\rho^4$. The comparison between the right hand side ($a(\rho)(R/L_{T_i} - R/L_{T_c})$) and the left hand side (\mathcal{L}) in equation (1) is examined with the root mean square of $((a(\rho)(R/L_{T_i} - R/L_{T_c}))/\mathcal{L} - 1)$ given by $\sigma = 0.13$. The zonal flow decay time $\tilde{\tau}_{ZF}$ [5] is examined. The radial profile of the zonal flow decay time $\tilde{\tau}_{ZF}$ is examined. The fitting function for the zonal flow decay time: $\tilde{\tau}_{ZF}(fit) = 0.98565 - 0.65943\rho + 2.4471\rho^2 + 3.2337\rho^3 - 2.8382\rho^4$ is used throughout the transport simulation. The first modeled turbulent ion heat diffusivity, where the term $a(\rho)(R/L_{T_i} - R/L_{T_c})$ is substituted for \mathcal{L} in $\chi_i^{(1)}/\chi_i^{GB}$, is shown as

$$\frac{\chi_i^{FTS(1)}}{\chi_i^{GB}} = C_0 \left(C_T a(\rho) \left(\frac{R}{L_{T_i}} - \frac{R}{L_{T_c}} \right) \right)^\delta. \quad (2)$$

The second modeled turbulent ion heat diffusivity, where the term $a(\rho)(R/L_{T_i} - R/L_{T_c})$ is substituted for \mathcal{L} and the fitting function $\tilde{\tau}_{ZF}(fit)$ is used for $\tilde{\tau}_{ZF}$ in $\chi_i^{(2)}/\chi_i^{GB}$, is also shown as

$$\frac{\chi_i^{FTS(2)}}{\chi_i^{GB}} = \frac{A_1 \left(a(\rho) \left(\frac{R}{L_{T_i}} - \frac{R}{L_{T_c}} \right) \right)^\alpha}{A_2 + \tilde{\tau}_{ZF}(fit) / \left(a(\rho) \left(\frac{R}{L_{T_i}} - \frac{R}{L_{T_c}} \right) \right)^{1/2}}. \quad (3)$$

To obtain the value of the turbulent ion heat diffusivity at each time step transport code, the values of equations (2) and (3) are calculated.

Now, the transport dynamics is examined using the modeled turbulent ion heat diffusivity, when the TASK3D [6] is performed. The radial profiles of the density and the electron temperature are fixed. The T_i profile of the experimental results at $t = 2.233$ s in the high- T_i LHD discharge #88343 is used as an initial state. The dynamics of the radial T_i profile is simulated by solving the diffusion equation. The profile of the radial electric field E_r is derived from the ambipolar condition at the initial plasma state. Three solutions of the ambipolar radial electric field are found in the radial region $0.265 \leq \rho \leq 0.785$. The profile of the radial electric field is dynamically fixed. The turbulent heat diffusivity is calculated using equations (2) and (3). At first, the positive E_r is chosen. We show the simulation results for the stationary ion temperature profile at $t = 0.1$ s with the solid line in figure 2. In figure 2(a), the simulation result for the ion temperature profile is obtained when we use $\chi_i^{FTS(1)}$. We show the simulation result of the T_i profile in figure 2(b) when $\chi_i^{FTS(2)}$ is used. The dashed line indicates the radial profile of T_i at $t = 2.233$ s in the LHD discharge #88343. In figure 2 (a) and (b), the simulation results for the radial T_i profile show a good agreement with the experimental results.

Specially, in figure 2(b) when the turbulent ion heat diffusivity is given by the function of $\tilde{\tau}_{ZF}$ in addition to L_{T_i} , the better agreement between the experimental and the simulation results is obtained. For modeling \mathcal{L} in terms of L_{T_i} , three runs at the different values of L_{T_i} are needed at a radial point before the dynamical transport simulation. It takes about one hour per one time of the program run. If the value of \mathcal{L} is calculated at each time step in the TASK3D, about one hundred thousand times of the program run are necessary. Therefore, the transport simulation of an extremely low computational cost can be achieved due to the additional modeling of the turbulent ion heat diffusivity based on the gyrokinetic simulation. Next, the negative radial electric field is chosen. The stationary profile of the ion temperature does not agree with the experimental results. The ion temperature is found to become low from the initial T_i profile and the lower ion temperature ($T_i \simeq 3.2\text{keV}$ at $\rho = 0$) is obtained.

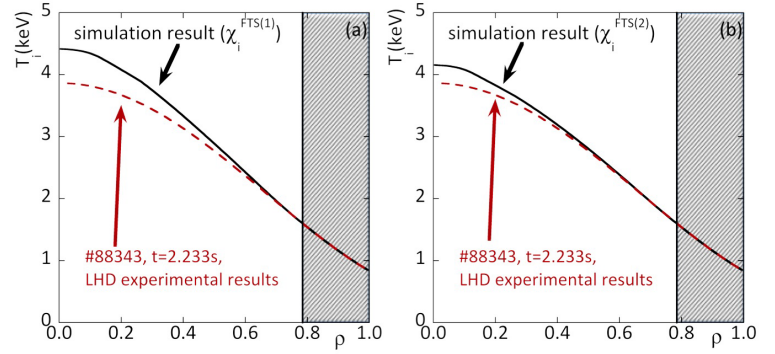


Figure 2: Simulation results for the T_i profile are shown using (a) $\chi_i^{FTS(1)}$ and (b) $\chi_i^{FTS(2)}$.

To reduce the simulation cost, how to apply the transport model based on a gyrokinetic simulation to a dynamical transport code is shown within the accuracy of the gyrokinetic simulation. The GKV-X code is performed for the additional modeling in terms of the ion temperature gradient scale length instead of the linear growth rate term for the ITG mode. The formula of the zonal flow decay time in the reduced model is derived at the given magnetic field structure. The value of the reduced model is reproduced by those of the modeled turbulent ion heat diffusivity with an extremely low computational cost. The simulation results by applying the additional modeled turbulent ion heat diffusivity to the dynamical transport code are shown. In this study, the promising technique of a low computational cost for adapting the gyrokinetic turbulent transport model to a transport code is proposed within allowable errors. Note that the form for the turbulent ion heat diffusivity by this additional modeling is valid for the high- T_i LHD discharge #88343. The dependence of the turbulent heat diffusivity on the field configuration and the plasma profiles for the LHD and different devices will be investigated. This report is based on the article [9].

The authors are grateful to the LHD Experimental Group for making the experimental data available. This work was partly supported by JSPS KAKENHI Grant Number 23561002, the NIFS Collaboration Research program (Plasma Simulator), NIFS14KNST062 and the Collaborative Research Program of Research Institute for Applied Mechanics, Kyushu University, 26FP-11.

- [1] Garbet X, Idomura Y, Villard L and Watanabe T -H 2010 *Nucl. Fusion* **50** 0433002
- [2] Nunami M, Watanabe T -H, Sugama H and Tanaka K 2012 *Phys. Plasmas* **19** 042504
- [3] Nunami M, Watanabe T -H and Sugama H 2013 *Phys. Plasmas* **20** 092307
- [4] Sugama H and Watanabe T -H 2006 *Phys. Plasmas* **13** 012501
- [5] Ferrando-Margalet S, Sugama H and Watanabe T -H 2007 *Phys. Plasmas* **14** 122505
- [6] Yokoyama M, Wakasa A, Seki R, Sato M, Murakami S, Suzuki C, Nakamura Y, Fukuyama A and LHD Experimental Group 2012 *Plasma Fusion Res.* **7** 2403011
- [7] Tanaka K, et al. 2010 *Plasma Fusion Res.* **5** S2053
- [8] Nunami M, Watanabe T -H, Sugama H and Tanaka K 2011 *Plasma Fusion Res.* **6** 001
- [9] Toda S, Nunami M, Ishizawa A, Watanabe T -H and Sugama H 2014 *Journal of Physics: Conference Series* **561** 012020

Integrated Transport Simulation of High Ti Plasma of LHD

Murakami, H. Yamaguchi, A. Sakai, A. Wakasa, A. Fukuyama, K. Nagaoka*, H. Takahashi*, H. Nakano*, M. Osakabe*, K. Ida*, M. Yoshinuma*, M. Yokoyama* and LHD Experiment group

Department of Nuclear Engineering, Kyoto Univ., Nishikyo, Kyoto 615-8540, Japan

**National Institute for Fusion Science, 322-6 Oroshi, Toki 509-5292, Japan*

e-mail: murakami@nucleng.kyoto-u.ac.jp

An integrated transport simulation code, TASK3D, is developed and applied to the high ion temperature plasma of LHD. The particle and heat transport equations are solved and compared with LHD experimental results. Relatively good agreements are obtained between the simulated and experimental profiles of the density and temperature in the steady state plasma of LHD. Next the high ion temperature plasma with the carbon pellet injection is simulated. It is found that the reduction of turbulence transport is most significant contribution to achieve the high ion temperature and that the reduction of the turbulent transport from the L-mode plasma (normal hydrogen plasma) is evaluated to be a factor about five. We introduce a Z_{eff} dependent turbulent transport improvement model and obtain a relatively good agreement in the time behavior of the ion temperature.

1. Integrated transport simulation of NBI heating plasma

We perform the integrated transport simulation of the NBI heating plasma of LHD. We assume that the heat transport consists of the neoclassical transport and the turbulent transport. The neoclassical transport coefficients are evaluated by the DGN/LHD[1, 2] module. We have investigated about twenty of pure hydrogen plasma shots and have found that the turbulence transport model the gyro-Bohm model for electron and the gyro-Bohm+gradTi model for ion have shown relatively good agreements with the experimental results with fixed constant factors, C_s , as

$$\chi_e^{TB} = C_e \left(\frac{T_e}{eB} \right) \left(\frac{\rho_e}{a} \right), \quad \chi_i^{TB} = C_i \left(\frac{T_i}{eB} \right) \left(\frac{\rho_i}{a} \right) \left(\frac{aT'_{ave}}{T_{ave}} \right) \quad (1)$$

where, $T_{ave} = (T_e + T_{i(bulk)})/2$, ρ_e , ρ_i , B , and a are the averaged temperature of electron and bulk ion, the Larmor radius of electron, the Larmor radius of ion, the magnetic field strength, and the minor radius. C_e and C_i are the constant factors estimated by best fitting of the hydrogen L-mode shot profile data. Based on the previous study, we used the constant factors; $C_e = 1.52$ and $C_i = 1.41$ [3].

We, also, assume that the particle transport consists of the neoclassical transport and the turbulent transport. The neoclassical transport coefficients are evaluated by the DGN/LHD[1, 2] module. We have applied several turbulent transport models for the particle transport; the constant model, the Alcator scaling model, the gyro-Bohm model and gyro-Bohm multiplied by gradient T term model (gyro-Bohm+gradT). We have found that the constant turbulent transport model for the particle transport is well agree with the experimental results. The turbulent part of the particle transport coefficient, D^{TB} , is assumed to be a constant as $D = 0.25$ [m²/s].

We perform the integrated transport simulation of the NBI heating plasma of LHD, the discharges (#109081, #109125 and #109125), where the density scan was done with fixing the NBI heating power [$P_{NBI} = 26.2$ MW]. We assume the magnetic field configuration of LHD as $R_{ax} = 3.6$ [m] and set the central magnetic field strength as $B_0 = 2.75$ [T].

The radial profile of the NBI heat deposition is evaluated by the FIT3D module[4]. In the FIT3D module the beam ion birth profiles are calculated by Monte Carlo method and the heat deposition profiles are evaluated by solving the Fokker-Plank equation in the $(v_{\parallel}, v_{\perp})$ space.

The particle source term, S_s , are consists of two parts; one is the ionization of neutral particle in the plasma and the other is the NBI injected beam ions. In the simulation we calculate the neutral particle profile by AURORA code[5] and evaluate the ionization profile of the neutral particle. The particle source by NBI heating beams is evaluated in the FIT3D module.

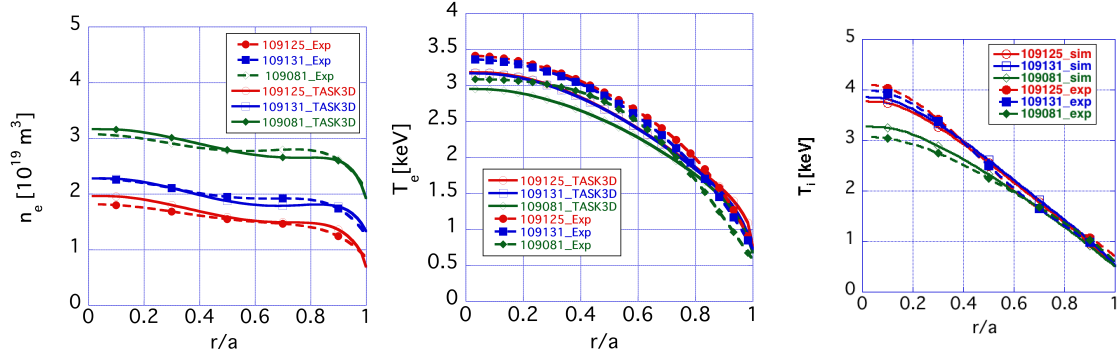


Figure 1: Comparisons TASK3D simulation results of the density (left) and temperature profiles of electron (center) and ions (right) with the experimental results of the density scan LHD discharges.

Figure 1 shows comparisons of the density (left) and, electron (center) and ion (right) temperature profiles by the TASK3D simulation with LHD experimental ones in the three different density cases. We control the plasma density varying the neutral particle density at the plasma edge to increase the neutral particle density and the ionization particle source term. Almost flat density profiles are obtained in three density cases and the small peaking of density would be due to the particle source from the NBI beam ions. We see good agreements of the plasma density profiles for these three density cases. The electron temperature reaches about 3keV and not strongly depend on the plasma density. The ion temperatures reach about 4keV in the two lower density cases and about 1keV lower in the higher density case. As a result we obtain relatively good agreements of the electron and ion temperature profiles.

2. Integrated heat transport simulation of C-pellet injection plasma

We study the high T_i plasma with C pellet injection of LHD[6, 7] applying the integrated simulation code GNET-TD+TASK3D.

We perform time-dependent NBI heating simulation of high T_i plasma of LHD using GNET-TD[8] code, which is a modified version of the 5D drift kinetic equation solver GNET[9]. We take into account the time development of the plasma density and temperature during the slowing-down of beam ions. Experimental data of the plasma density, temperature, and NBI heating is used as the input to TASK3D.

In order to analyze the NBI heat deposition profile of time evolving plasma. We performed NBI heating simulation of high- T_i discharge (# 110599) plasma, in which the plasma density changes in time due to the C pellet injection. There are five NBI injectors and one of them #4 is modulated in order to measure the ion temperature. In the simulation time change of densities and temperature profiles are from the experimental measurements. The plasma density rapidly increases due to the pellet injection and decays gradually. The Z_{eff} also increases due to the increase of the carbon impurity by the pellet injection. In this simulation we have assume the pure hydrogen plasma as a first step in order to evaluate the plasma heat depositions. Also, for simplicity we assumed $T_e = T_i$ because $V_{beam} \gg V_i$. We evaluate the beam distributions including time evolutions of density and temperature and beam modulations.

Before the C pellet injection beam ion distribution reaches a steady state slowing down distribution, and just after the pellet injection strong slowing down of energetic beam can be seen at the edge region. But we can not see clear change in the central region. After the density decay phase the beam ion distribution is recovered.

Figure 2 shows the time history of the NBI heat deposition in the core region $r/a < 0.5$ (left) and the outer region $r/a > 0.5$ (right). The heat deposition jumps up by the pellet injection and by the start of the perpendicular #4 injector at $t = 4.575s$. In the edge region we can see a large

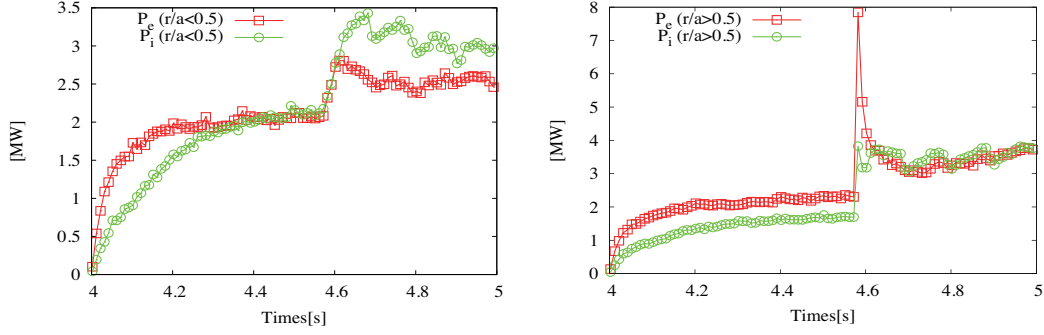


Figure 2: Time history of NBI heat deposition of electron and ion in the inner region $r/a < 0.5$ (left) and the outer region $r/a > 0.5$ (right).

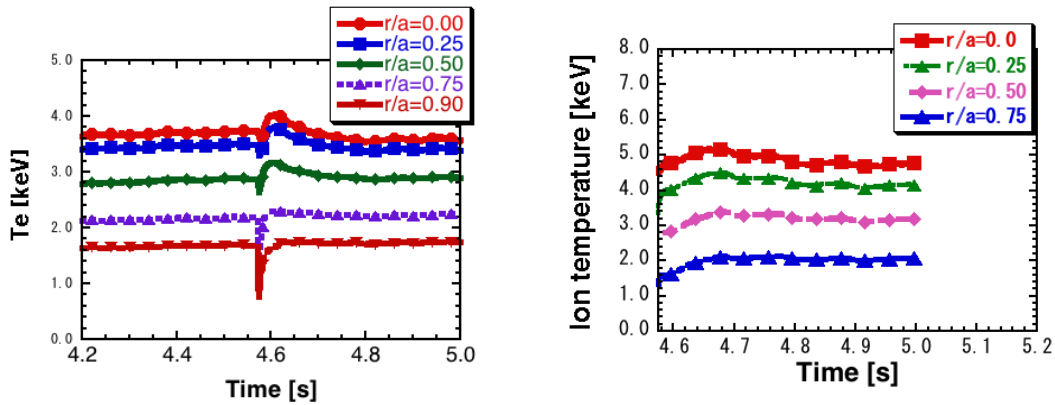


Figure 3: Time history of electron (left) and ion (right) temperatures before and after the C-pellet injection ($t = 4.575$ s).

jump in the electron heating power due to the rapid slow down of the energetic beam ions by the C-pellet injection.

Next we investigate the heat transport of high T_i plasma (# 110599) assuming multi-ion species plasma (e, H, He, C) by the integrated transport code, TASK3D[10, 11]. In the previous paper we, also, have shown that the ion and electron temperature agrees well with that of experimental results with the assumed turbulent transport model in the time evolving pure hydrogen NBI heating plasma with out pellet injection [12].

Figure 3 shows the TASK3D simulation results of the high- T_i discharge (# 110599) plasma. The electron temperature drops rapidly by the pellet injection at $t = 4.575$ s and backed to the previous temperature (Fig. 3, left). This shows similar behavior with the experimental one. The ion temperature increases to more than 5 keV just after the pellet injection until $t = 4.7$ s and gradually decreases (Fig. 3, right). This is due to the reduction of effective neoclassical transport and the decrease of the ion number density by the C-pellet injection. However the obtained T_i value is lower than that of experimental one. This indicates that the reduction of the turbulent transport is necessary to explain the observed high- T_i .

Next we introduce the confinement improvement factor, γ_{TB} , in the ion turbulent heat transport model as

$$\chi_i^{TB} = \frac{1}{\gamma_{TB}} \chi_{(L-mode)}^{TB}. \quad (1)$$

where $\chi_{(L-mode)}^{TB}$ is the turbulent transport model assumed in the pure hydrogen plasma. It is found that about factor five of the improvement of the turbulent heat conduction is necessary to obtain the high T_i observed experimentally. Interestingly we see a large enhancement of negative radial electric field by changing the improving factor γ and this enhanced radial electric field reduce the

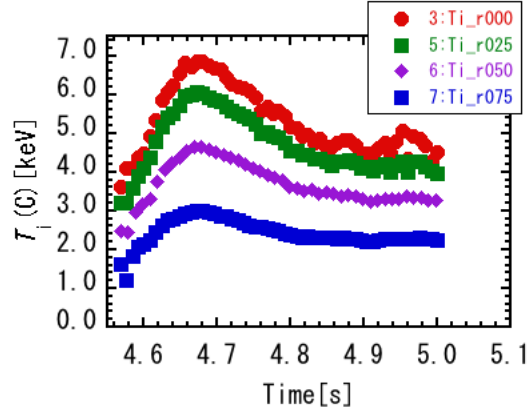


Figure 4: *Time history of T_C with the Z_{eff} depending improvement model.*

neoclassical transport of ions. Increasing the γ we obtain higher T_i but the neoclassical transport value does not increase or even decreased for hydrogen ion.

It has been suggested experimentally that the C impurity is one of key factors in the ion heat transport improvement in the LHD[13]. So we consider the turbulent transport improvement model depending on Z_{eff} . The IFS-PPPL transport model has included the model depending on Z_{eff} . We, first, consider the turbulent transport improving model assuming the similar Z_{eff} dependence. However the reduction is much smaller and we found that this model can not explain the LHD experimental results.

Then, we assume the following stronger Z_{eff} depending model as

$$\chi_i^{TB} = \gamma_Z \chi_i^{TB(L-mode)}, \quad \gamma_Z = \min(1, (C_Z/Z_{eff})^{k_Z}). \quad (2)$$

Figure 4 shows the simulation results with the stronger Z_{eff} depending model ($C_Z = 1.5$ and $k_Z = 1.8$). We obtain a relatively good agreement of the ion temperature time behavior after the pellet injection with the experimental results.

- [1] Wakasa, A. et al., Jpn. J. App. Phys. **46** (2007) 1157.
- [2] Wakasa, A. et al., Plasma Fusion Res., **3** (2008) S1030.
- [3] Wakasa, A. et al., Proc. 39th EPS Conf. and 16th Int. Cong. Plasma Phys., 2012, **P2.028**.
- [4] Murakami, S., et al., Trans. Fusion Technol. **27** (1995)
- [5] Hughes M.H. and Post D.E., J. Comput. Phys., 28, (1978) 43.
- [6] Takahashi, H. et al., Nucl. Fusion **53** (2013) 073034.
- [7] Nagaoka, K. et al 2011 Nucl. Fusion 51 083022
- [8] Yamaguchi, H. et al., Plasma Fusion Res., **8** (2013) 2403099.
- [9] Murakami, S. et al., Nucl. Fusion, **46** (2006) S425.
- [10] Sato M. et al., Plasma Fusion Res., **3** (2014) S1063.
- [11] Sakai, A. et al., Plasma Fusion Res., **9** (2014) 3403124.
- [12] Yamaguchi, H. et al., JPS Conf. Proc., **1** (2014) 015045.
- [13] Osakabe, M., et al., Plasma Phys. Control. Fusion 56 (2014) 095011.

Fokker-Planck Simulation of the Runaway Electron Generation in Tokamak Disruption

H. NUGA¹, A. MATSUYAMA¹, M. YAGI¹, A. FUKUYAMA²

¹Japan Atomic Energy Agency

²Department of Nuclear Engineering, Kyoto University

Disruptive plasma termination is one of the crucial problems for large scale tokamaks, such as ITER. The disruption of tokamak plasmas causes rapid thermal and current quenches. The toroidal electric field induced by the rapid current quench accelerates electrons to the relativistic high energy and some of them become runaway electrons (REs). The impact of REs to the first wall leads crucial localized heat load. Since the RE generation rate is expected to be higher for a large-scale tokamak, the estimation of the amount of the REs during tokamak disruption is an important issue for the development of operation scenarios, such as the mitigation method.

The simulation of the RE generation simulation during tokamak disruption should include the non-thermal effect. This is because, if the thermal quench is enough fast, the plasma cools down so quickly that high velocity electrons, of which collision time is longer than the quench time, do not have enough time to thermalize. These non-thermal electrons forms the high velocity tail of the electron velocity distribution. The existence of this high energy tail enhances the primary RE generation rate and this effect is called as “hot-tail effect”.

There are several previous works[1, 2] that simulate the RE generation process during tokamak disruption including self-consistent induced electric field. Especially, Smith[3] and Fehér[4] are one of the works that include hot-tail effect to self-consistent RE generation simulation. In their model, however, the primary REs are divided into two components, hot-tail REs and Dreicer REs. The tail formation due to thermal quench is evaluated by one dimensional Fokker-Planck equation neglecting electric field and the hot-tail REs are defined as the number of electrons whose velocity is faster than $v_c = v_{th}(E_D/E)^{1/2}$, where v_{th} , E_D and E are the thermal velocity, the Dreicer electric field and parallel electric field. On the other hand, the Dreicer component is described by the conventional steady state model[5]. Since these components are intrinsically indivisible, it might be a problem when the hot-tail effect becomes important. Therefore the self-consistent description of the momentum distribution and the induced electric field is desirable for accurate evaluation of RE current. To our knowledge, this has not been done so far.

In our present research, we have developed a Fokker-Planck simulation code TASK/FP in order to calculate the time evolution of the relativistic momentum distribution function and that of induced toroidal electric field self-consistently. It solves the Fokker-Planck equation:

$$\frac{\partial f}{\partial t} = -\nabla \cdot \mathbf{S}_{C,E} \quad (1)$$

$$\mathbf{S}_{C,E} = -\overleftrightarrow{\mathbf{D}}_C \cdot \nabla f + \mathbf{F}_{C,E} f, \quad (2)$$

where ∇ is a derivative operator in momentum space and f is a relativistic momentum distribution function. In this paper, the weak relativistic isotropic background collision term[6] with relativistic

Maxwellian is adopted for \vec{D}_C and F_C . The induced electric field E obeys following equations:

$$\frac{1}{r} \frac{\partial}{\partial r} \left(r \frac{\partial E}{\partial r} \right) = \mu_0 \frac{\partial j}{\partial t} \quad (3)$$

$$j = \sigma_{sp} + ecn_r \quad (4)$$

$$\frac{dn_{rp}}{dt} = \int \nabla \cdot S_{C,E} d\mathbf{p} \quad (5)$$

$$\frac{dn_{rs}}{dt} = n_r \frac{\bar{E} - 1}{\tau_r \ln \Lambda} \sqrt{\frac{\pi\varphi}{3(Z_{eff} + 5)}} \left(1 - \bar{E} + \frac{4\pi(Z_{eff} + 1)^2}{3\varphi(Z_{eff} + 5)(\bar{E}^2 + 4/\varphi^2 - 1)} \right)^{-1/2} \equiv S_s(n_r, \bar{E}), \quad (6)$$

where σ_{sp} is a Spitzer conductivity. RE density n_r is a sum of two kind of RE density, ‘‘primary REs’’ and ‘‘secondary REs’’: $n_r = n_{rp} + n_{rs}$. The density of primary REs is defined in eq. (5) as electrons go out from the momentum calculation domain: $0 < p < p_{max}$ and $p_{max}^2/m \sim 1\text{MeV}$. On the other hand, the secondary RE generation rate[7] is expressed as the function of n_r and $\bar{E} = E/E_C$ in eq. (6), where $E_C = E_D(v_{th}/c)^2$, $\varphi = 1 - 1.46\varepsilon^{1/2} + 1.72\varepsilon$, $\varepsilon = r/R$ and $\tau_r = 4\pi\epsilon_0^2 m^2 c^3 / n_e q^4 \ln \Lambda$. Ohm’s law is adopted as the closure in the diffusion equation of E . Here, it is assumed that the velocity of all REs equals to the velocity of light and REs are collisionless.

In order to reveal the influence of the hot-tail effect, we implement the other primary RE generation rate derived by Conner and Hastie[5] which do not consider the hot-tail effect. That primary RE generation rate is expressed as a function of the temperature and $\hat{E} = E/E_D$:

$$\frac{dn_{rp}}{dt} = S_{dreicer}(\hat{E}, T). \quad (7)$$

Under the condition of the steady electric field and constant plasma temperature, the values of the primary RE generation rate calculated by eq. (5) and (7) have good agreement.

In the following calculation, the background plasma temperature obeys:

$$T(t, \rho) = (T(0, \rho) - T_f(\rho)) \exp(-t/\tau_q) + T_f(\rho) \quad (8)$$

$$T_f(\rho) = T_f(0)(1 - 0.9\rho^2), \quad (9)$$

where ρ denotes normalized minor radius, τ_q is a parameter of the thermal quench time, and T_f denotes the post-quench plasma temperature, respectively. We employ the JT-60U like plasma parameters, such as major radius $R = 3.4\text{m}$, minor radius $a = 1.0\text{m}$, initial plasma current $I_p = 1.052\text{MA}$, initial temperature $T(0, 0) = 2\text{keV}$, post-quench temperature $T_f(0) = 10\text{eV}$, electron density $n_e(0) = 4 \times 10^{19}\text{m}^{-3}$ and $Z_{eff} = 3$. We compare the simulation results of RE generation during thermal quench between two cases, A: includes the hot-tail effect and B: excludes hot-tail effect. In case A, RE generation is simulated by eqs. (1)-(6). In case B, on the other hand, eq. (7) is used instead of eq (5).

Figure 1 and 2 show the time evolution of net plasma current and RE current for case A and B with different values of τ_q . From fig. 1, it is found that the hot-tail effect enhances the RE current for $\tau_q = 0.15\text{msec}$. By contrast, fig. 2 shows that the hot-tail effect is not effective for $\tau_q = 0.50\text{msec}$. These results indicate that the steady state RE generation model eq. (7) is valid for the slow thermal quench case. Figure 3 show the relation between the thermal quench time and primary RE current ratio for case A and B. For faster thermal quench, the primary RE current ratio in case A becomes higher than that of in case B and it seems that the criterion value becomes

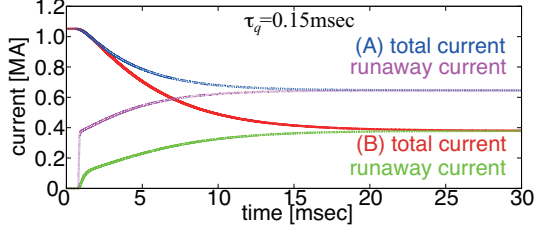


Figure 1: The time evolution of net plasma current and RE current for $\tau_q = 0.15\text{msec}$.

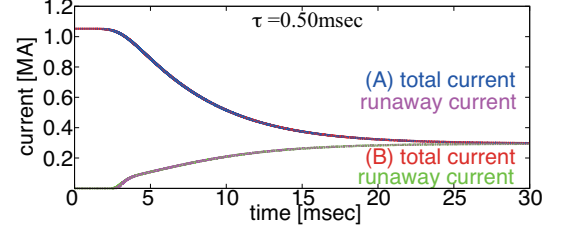


Figure 2: The time evolution of net plasma current and RE current for $\tau_q = 0.50\text{msec}$.

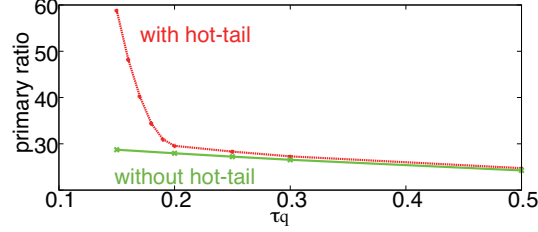


Figure 3: The relation between τ_q and the primary RE current ratio at $t = 30\text{msec}$. Red line denotes the case A and green line denotes the case B.

around $0.2 - 0.3\text{msec}$. This threshold can be roughly estimated from the electron-electron slowing down time τ_{ee}^s . The e-e slowing down time for the velocity $v \gg v_{th}$ is expressed as:

$$\tau_{ee}^s(v) = \frac{2\pi\epsilon_0^2 m^2 v^3}{n_e q^4 \ln \Lambda}. \quad (10)$$

If the thermal quench time is longer than the slowing down time for almost all electrons, it is presumable that the tail of the momentum distribution is not formed and the hot-tail effect is suppressed. Since the most electrons have the velocity less than a few times of v_{th} , the slowing down time for such a velocity can be seen as a criterion value. In this simulation case, $\tau_{ee}^s(3v_{th}) \sim 0.26\text{msec}$ and this value seems to be valid criterion.

This study was supported in part by the Grant-in-Aid for scientific research, No. 23246163, from Japan Society for the Promotion of Science, and by the use of the Helios system at the International Fusion Energy Research Center (project code: KIMHCD).

- [1] L.-G. Eriksson and P. Helander, *Comput. Phys. Commun.* **154**, 175, (2003).
- [2] H. Smith, *et. al.*, *Phys. Plasmas*, **13**, 102502, (2006).
- [3] H. M. Smith and E. Verwichte, *Phys. Plasmas*, **15**, 072502, (2008).
- [4] T. Fehér, *et. al.*, *Plasma Phys. Control. Fusion*, **53**, 035014, (2011).
- [5] J. W. Conner and R. J. Hastie, *Nuclear Fusion*, **15**, 415, (1975).
- [6] C. F. F. Karney, *Computer Physics Report*, **4**, 183, (1986).
- [7] M. N. Rosenbluth and S. V. Putvinski, *Nuclear Fusion*, **37**, 1355, (1997).
- [8] S. C. Chiu, *et. al.*, *Nuclear Fusion*, **38**, 1711, (1998)

Hybrid, reduced modeling of coupled energetic particle-driven modes

M. Lesur

Research Institute for Applied Mechanics, Kyushu University

In collisionless plasmas, it is known that energetic particle-driven modes can be destabilized even when they are linearly stable (subcritical excitation), by the nonlinear growth of vortex-like structures in phase-space [1,2,3,4]. Indeed, the growth of such structures is a nonlinear kinetic mechanism, which provides a channel for free-energy extraction, different from conventional inverse Landau damping. However, nonlinear growth requires the presence of a seed structure, with a threshold in amplitude [3]. In parameter regimes relevant for current days magnetic fusion experiments, the amplitude threshold is much larger than the thermal noise, except when the linear growth rate γ is very close to marginal stability ($-1\% < \gamma / \gamma_L < 0$, where γ_L is the linear drive by energetic particles).

This paper assesses whether wave-wave coupling can provide a seed structure in the presence of a second, linearly unstable (supercritical) mode. By modeling a subcritical mode kinetically in a one-dimensional plasma, and the impact of the supercritical mode by parametric coupling equations, I show that a subcritical instability can be easily triggered. The conclusions stand true even when the frequency of the supercritical mode is rapidly sweeping (chirping).

The new model is hybrid in the sense that it combines kinetic nonlinearities with fluid nonlinearities. The evolution of the energetic particle distribution is given by

$$\frac{\partial f}{\partial t} + v \frac{\partial f}{\partial x} + \frac{qE_1}{m} \frac{\partial f}{\partial v} = \frac{v_f^2}{k_1} \frac{\partial(f - f_0)}{\partial v} + \frac{v_d^3}{k_1^2} \frac{\partial^2(f - f_0)}{\partial v^2}, \quad (1)$$

where E_1 is the electric field of the subcritical mode, and k_1 is its wave number.

The bulk (or thermal) particles, which support the waves, are assumed to interact adiabatically with the wave, so that their contribution can be expressed as a part of the electric field [5].

I have split the electric field between the two waves, $E = E_1 + E_2$ and assumed that the kinetic impact of wave 2 at the resonant location of wave 1 is negligible. In other words, I assume that there is enough overlap between the two mode structures to enable energy transfer, but not enough for wave 2 to significantly redistribute energetic particles which resonate with wave 1. Assuming that wave 2 is roughly a second harmonic of wave 1, the electric field components $E_n = Z_n \exp[i(k_n x - \omega_n t)] + c. c.$ follow the equations

$$\frac{dZ_1}{dt} = -\frac{m \omega_p^3}{4\pi q n_0} \int f(x, v, t) \exp[-i(k_1 x - \omega_1 t)] dx dv - \gamma_d Z_1 - i \frac{V}{\omega_1} Z_2 Z_1^* e^{-i\theta t} \quad (2)$$

$$\frac{dZ_2}{dt} = -i \frac{V}{\omega_2} Z_1^2 e^{i\theta t}. \quad (3)$$

Here, the term proportional to γ_d in Eq. (2) is an external wave damping, which is a model

for all linear dissipative mechanisms of the wave energy to the background plasma. For simplicity, I have assumed that the damping and the drive of mode 2 are balanced. The last term in Eqs. (2) and (3) describe the interaction between the two waves, which depends on a coupling constant V and the frequency mismatch $\theta = \omega_2 - 2\omega_1$.

This model can be viewed as an extension of the Berk-Breizman model [6] to multiple modes at different radial locations. It is implemented as an expansion of the COBBLES code [7].

Linearly, the growth rate of mode 1 is $\gamma \approx \gamma_L - \gamma_d$, where γ_L is the linear drive, proportional to the slope of energetic particle velocity distribution at the resonant velocity. Here, I consider only the region of subcritical instability, that is, $\gamma < 0$.

I first performed a series of simulations without frequency mismatch ($\theta = 0$). Figure 1 (on next page) shows the peak of the amplitude of the linearly stable mode ($C_1 = |Z_1|$), normalized by the initial amplitude of mode 2 ($C_{2,0}$). For comparison, Fig.1 (a) is the well-known case of pure fluid nonlinearity, that is assuming that the integral in Eq. (2) vanishes. As can be seen by comparing Fig.1 (a) and Fig.1 (b), the kinetic nonlinearity has a strong impact on the nonlinear stability of mode 1, namely, it expands the stability threshold by more than one order of magnitude (except far from the linear stability of mode 1), from $V > 0.2$ to $V > 0.01$ (in units of $C_{2,0}$). As observed in my simulations (not shown here), the physical mechanism is as follows: fluid coupling between the assumed unstable wave 2, and the simulated linearly stable wave 1, drives the amplitude of wave 1 to a value, relatively small, but much larger than thermal noise. This amplitude is sufficient to trap a significant number of particles, creating a vortex in phase-space, which acts as a seed to trigger a subcritical instability, according to the mechanism described in Ref. [3].

In Fig.1 (c) and Fig.1 (d), the collision frequencies are varied, as shown in the legend. (c) corresponds to low collision frequencies, and (d) corresponds to high collision frequencies. As expected, lower collision frequencies exacerbate the impact of kinetic nonlinearities, and the nonlinear stability becomes even more sensitive to the distance to linear marginality of mode 1, than to the coupling constant.

The conclusions stay valid in the presence of a small frequency mismatch (not shown here), or when the frequency of mode 2 is dynamically changing (chirping, $\theta(t)$). Fig.1 (e) is the nonlinear instability diagram, for the same collision frequencies as Fig.1 (b), but when mode 2 is chirping with $d\theta/dt = 7 \cdot 10^{-4} \omega_p^2$.

For all figures, I have arbitrarily chosen $C_{2,0} = 10^{-2} m\omega_p^2/(qk)$. However, I have confirmed that the figures are not sensitive to this choice (not shown here), whether $C_{2,0}$ be one order higher, or one order smaller.

In conclusion, I have developed a new hybrid, reduced model for coupled energetic particle modes, and shown for the first time that the combination of fluid nonlinearities and kinetic nonlinearities expands the unstable region significantly into the linearly stable region, even when fluid coupling alone is one order of magnitude too weak (in terms of the coupling coefficient) to do so, and even relatively far from linear marginal stability ($-0.2 < \gamma/\gamma_L < 0$).

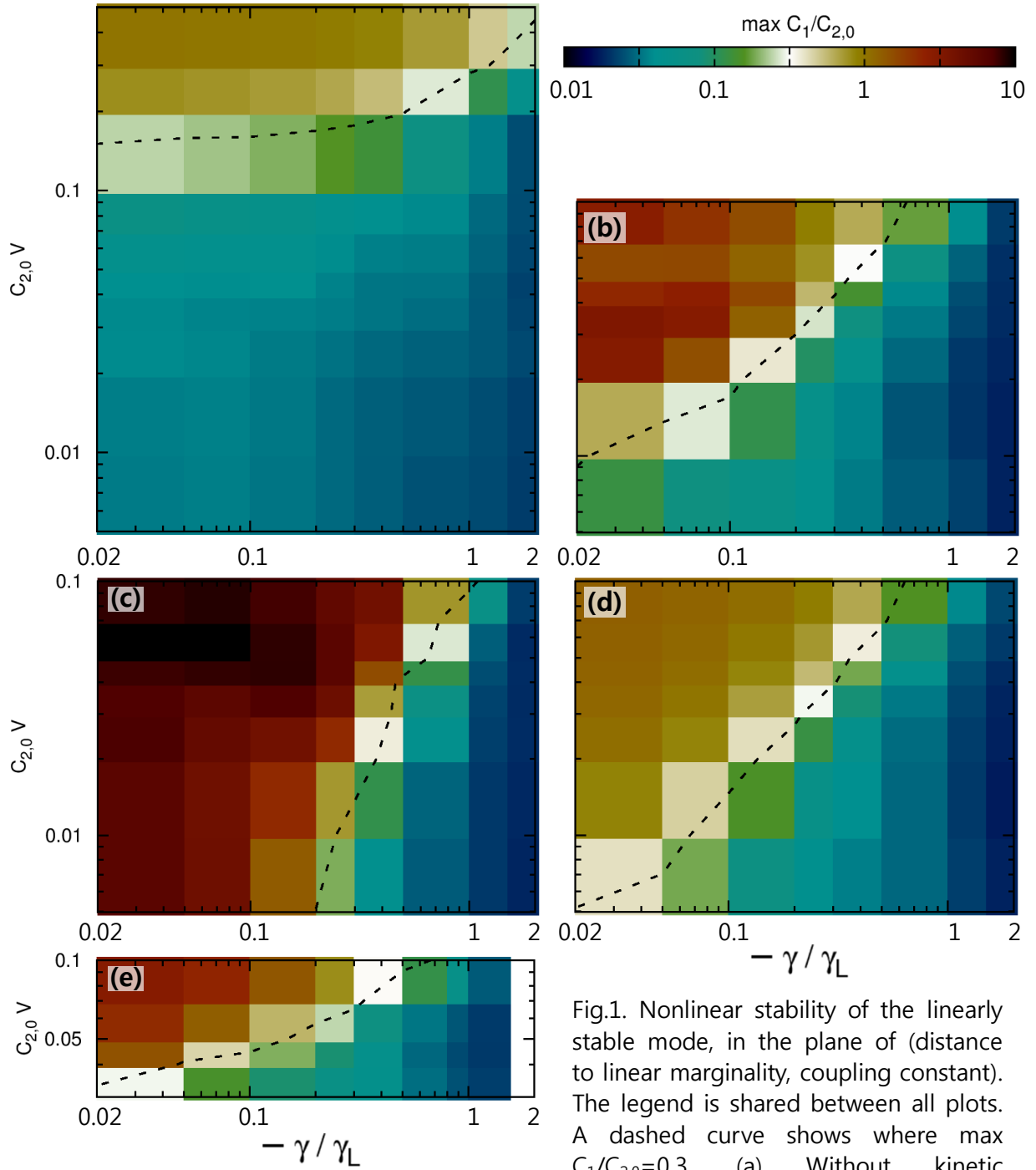


Fig.1. Nonlinear stability of the linearly stable mode, in the plane of (distance to linear marginality, coupling constant). The legend is shared between all plots. A dashed curve shows where $\max C_1/C_{2,0}=0.3$. (a) Without kinetic nonlinearity. (b) $\nu_i/\gamma_L=0.02$, $\nu_d/\gamma_L=0.1$. (c) $\nu_i/\gamma_L=0.005$, $\nu_d/\gamma_L=0.01$. (d) $\nu_i/\gamma_L=0.07$, $\nu_d/\gamma_L=0.7$. (e) Same as (b) but mode 2 is chirping.

- [1] H. Schamel, Phys. Scr. **20**, 336 (1979)
- [2] T.H. Dupree, Phys. Fluids **15**, 334 (1982)
- [3] M. Lesur, and P.H. Diamond, Phys. Rev. E **87**, 031101 (2013)
- [4] M. Lesur, P.H. Diamond, and Y. Kosuga., Plasma Phys. Contr. Fusion **56**, 075005 (2014)
- [5] M. Lesur and Y. Idomura, Nucl. Fusion **52**, 094004 (2012)
- [6] H.L. Berk, B.N. Breizman, and M. Pekker, Phys. Plasmas **2**, 3007 (1995)
- [7] M. Lesur, Y. Idomura, and X. Garbet, Phys. Plasmas **16**, 092305 (2009)

Steep wave front of drift waves in linear magnetized plasmas

M. Sasaki^{1, 2}, N. Kasuya^{1, 2}, K. Itoh^{2, 3}, T. Yamada^{2, 4}, M. Yagi^{2, 5}, and S.-I. Itoh^{1, 2}

¹Research Institute for Applied Mechanics, Kyushu University, Kasuga 816-8580, Japan

²Research Center for Plasma Turbulence, Kyushu University, Kasuga 816-8580, Japan

³National Institute for Fusion Science, Toki 509-5292, Japan

⁴Faculty of Arts and Science, Kyushu University, Fukuoka 819-0395, Japan

⁵Japan Atomic Energy Agency, Rokkasho 039-3212, Japan

1 Introduction

Importance of turbulent structures driven by nonlinear processes of turbulence has been recognized in the study on transport in magnetically confined plasmas [1, 2]. Basic experimental plasmas, such as in linear devices, play important roles for study on nonlinear processes of the turbulence, since detailed measurements of fluctuations are possible. The streamer and the zonal flows have been observed, and the detail nonlinear processes have been studied [3]-[6]. The energy transfer of the drift waves to higher wavenumber modes has also been observed as the formation of a solitary drift wave structure, which has a steep wave front in the azimuthal direction [7]. The formation of the steep wave front is one of important aspects of the nonlinear waves, so that the understanding of the formation mechanism is required. In this study, we focus on the formation mechanism of the steep wave front of the solitary drift wave in cylindrical plasmas by using a three dimensional simulation of resistive drift waves.

2 Solitary drift waves

A three-dimensional simulation of resistive drift waves in a cylindrical plasma is performed using the Numerical Linear Device (NLD) code [8]. According to the experiments in PANTA

device [9], we focus on high density $n_e \sim 1 \times 10^{19}[\text{m}^{-3}]$ with low temperature $T_e \sim 5[\text{eV}]$ plasmas in an argon discharge. The set of the model equations of the simulation is based on an extension of Hasegawa-Wakatani equations to include the effects of the neutral particle and the nonlinearity of the electron parallel velocity. The following parameters are used; $B = 0.3[\text{T}]$, $T_e = 3[\text{eV}]$, $a = 10[\text{cm}]$, $\lambda = 4[\text{m}]$, $\nu_{in} = 0.04$, $\mu_W = \mu_V = 10^{-4}$, and $\nu_e = 510$, where the notations are same as those in [8]. Simulations are performed with 256 grids in the radial direction. Fourier modes $-16 \leq m \leq 16$, $-8 \leq n \leq 8$ are kept in the simulations, including $(m, 0)$, $(0, n)$ modes, where m and n are the azimuthal and axial mode numbers, respectively.

The spatio-temporal structure of the solitary drift wave is described, and the steep wave front in the azimuthal direction is shown, which can be understood by the phase dynamics. The density fluctuation propagates without changing its shape as a solitary wave in the positive azimuthal direction, which is the electron diamagnetic direction. Figure 1 shows a snapshot of the azimuthal structure of the density fluctuation at $t = 6500$ with the fundamental, second and third harmonics modes. The steep wave front can be seen in the azimuthal direction around $-0.5\pi < \theta < 0$, and it faces in the propagation direction. In the region of the

steep wave front, all the modes of the fundamental and its harmonics have negative slope so that the steep wave front is formed and is sustained by locking the phase relations among these modes. The evolution of the phase difference between the fundamental and second harmonic modes is shown in Fig. 2, where the phase difference is evaluated by

$$\Delta\Psi = 2\Psi_{1,1} - \Psi_{2,2} = \arctan \left[\frac{\text{Im}N_{1,1}^2 N_{2,2}^*}{\text{Re}N_{1,1}^2 N_{2,2}^*} \right]. \quad (1)$$

Here, the phase $\Psi_{m,n}$ is calculated from

$$N_{m,n} = |N_{m,n}| e^{i\Psi_{m,n}}. \quad (2)$$

The value of the phase difference is sustained for a long time compared to the drift wave oscillation, and is almost constant around $\Psi \approx \pi/2$.

We show that this phase difference is the stationary solution of the phase evolution equation, and discuss the stability of the stationary solutions. The evolution equation of the phase difference $\Delta\Psi$ can be written as

$$\frac{\partial\Delta\Psi}{\partial t} \approx \Delta\omega + \Xi_c \cos(\Delta\Psi + \delta) + \Xi_s \sin(\Delta\Psi + \delta), \quad (3)$$

$$\Xi_c = \frac{|\phi_{1,1}| |N_{1,1}|}{r |N_{2,2}|} \partial_r \ln \left(\frac{|\phi_{1,1}|}{|N_{1,1}|} \right), \quad (4)$$

$$\Xi_s = \frac{|\phi_{1,1}| |N_{1,1}|}{r |N_{2,2}|} \partial_r \delta, \quad (5)$$

where $\Delta\omega$ is the linear frequency difference defined as $\Delta\omega = 2\omega_{1,1} - \omega_{2,2}$, and δ is the phase difference between the density and the potential. Here, we focus on the convective derivative term $[N, \phi]$ among the nonlinear terms. The coefficient Ξ_c is related to the radial derivative of the amplitude ratio between the density and potential fluctuations, and Ξ_s is determined by the radial derivative of the phase difference δ , so that they become finite when the density and potential deviate from the Boltzmann relation. Here, it should be noted that Ξ_c is determined by the local gradients of the fluctuation amplitudes. Thus, the difference of the radial eigenmodes of $\phi_{1,1}$ and $N_{1,1}$ has significant impact

for Ξ_c . While, when $|\phi_{1,1}(r)| = |N_{1,1}(r)|$, the Ξ_c term becomes zero, and the phase difference term Ξ_s becomes important.

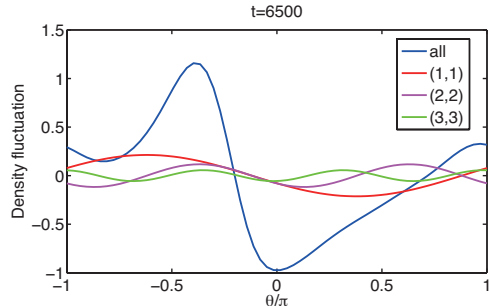


Fig. 1: Snapshot of the azimuthal structure of the density fluctuation at $t = 6500$.

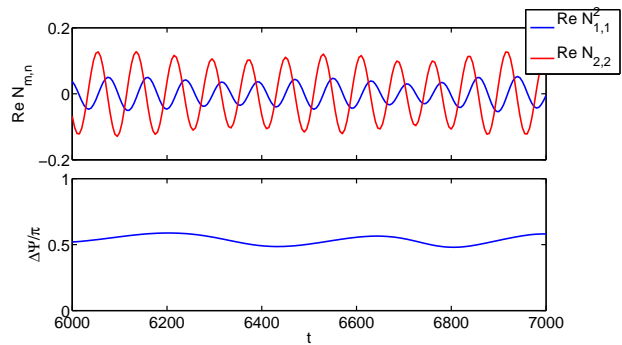


Fig. 2: Temporal evolution of phase difference between modes with (1,1) and (2,2).

Equation (3) has a stationary solution as

$$\Delta\Psi = \pm\pi/2 - \delta \approx \pm\pi/2, \quad (6)$$

in the case of $|\Xi_c| \gg |\Xi_s|$ and of $\Delta\omega = 0$. The solution, $\Delta\Psi = \pi/2$, is that the fundamental mode precedes the second harmonics and the steep wave front faces forward in the propagation direction, and the solution, $\Delta\Psi = -\pi/2$, is related to the steep wave front facing backward in the propagation direction.

The stabilities of the stationary solutions can be analyzed by giving perturbation $\tilde{\Psi}$ to the stationary solution. The linearized equation for $\tilde{\Psi}$ is obtained as

$$\frac{\partial\tilde{\Psi}}{\partial t} = \left[-\Xi_c \sin(\Delta\Psi_s) + \Xi_s \cos(\Delta\Psi_s) \right] \tilde{\Psi}, \quad (7)$$

The sign of the coefficient of $\tilde{\Psi}$ in the RHS of Eq. (7) determines the stability of the stationary solutions. The stability of the solutions, $\Delta\Psi_s = \pm\pi/2$, is governed by the sign of Ξ_c . When $\Xi_c > 0$, the solution with $\Delta\Psi_s = \pi/2$ is stable so that the steep wave front faces forward in the wave propagation direction. When $\Xi_c < 0$, the solution with $\Delta\Psi_s = -\pi/2$, which corresponds to the steep wave front facing backward in the propagation direction, is realized.

The time averaged radial profiles of Ξ_c and Ξ_s are shown in Fig. 3. The magnitudes of the Ξ_c is much larger than that of Ξ_s in the region of $r/a < 0.4$, where the fluctuations exist. The positive Ξ_c is obtained so that $\Delta\Psi_s = \pi/2$ is the stable stationary solution. This is because the radial wavelengths of the fluctuations are comparable to the plasma size in this simulation so that the difference of the radial structures of the density and potential is not negligible. Thus, Ξ_c is important in this simulation. It is confirmed that the simulation result, the steep wave front facing forward in the propagation as in Figs. 1, and 2, is consistent with the theoretical prediction.

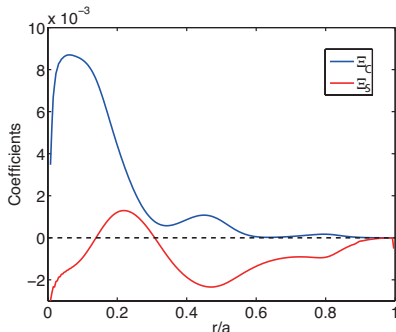


Fig. 3: Radial profile of time averaged Ξ_c and Ξ_s .

3 Summary

The formation mechanism of the solitary drift wave is investigated by using the three-dimensional simulation of the resistive drift waves in cylindrical plasmas. The solitary drift wave is observed in the regime where the collisional transport is important as well as fluctuation induced

transport. The solitary drift wave forms a steep wave front in the azimuthal direction. The phase differences between the fundamental and second harmonic modes are locked so that the steep wave front is sustained for a long time compared to the drift wave oscillation. The simulation results can be explained by the phase entrainment of the drift waves. The details of this study are described in [10].

References

- [1] P. H. Diamond, et. al., Plasma Phys. Control. Fusion, **47**, R35 (2005).
- [2] A. Fujisawa, et. al., Nucl. Fusion, **49**, 013001 (2009).
- [3] T. Yamada, Nature Phys., **4**, 721 (2008).
- [4] Y. Nagashima, et. al., Journal of Phys. Soc. Jap., **77**, 114501 (2008).
- [5] Z. Yan, et. al., Phys. Plasmas, **15**, 092309 (2008).
- [6] M. Xu, et. al., Phys. Plasmas, **17**, 032311 (2010).
- [7] H. Arakawa, et. al., Plasma Fusion Res. **5**, S2044 (2010).
- [8] N. Kasuya, et. al., J. Phys. Soc. Japan, **76**, 044501 (2007).
- [9] S. Oldenburger, et. al., Plasma Phys. Control. Fusion, **54**, 055002 (2012).
- [10] M. Sasaki, et. al., submitted to Phys. Plasmas (2015).

Integrated modeling of JT-60SA plasma operation scenarios with model validation and verification

N. Hayashi¹⁾, J. Garcia²⁾, M. Honda¹⁾, K. Shimizu¹⁾, K. Hoshino³⁾, S. Ide¹⁾, G. Giruzzi²⁾, Y. Sakamoto³⁾, T. Suzuki¹⁾, H. Urano¹⁾

1) Japan Atomic Energy Agency, Naka, Ibaraki 311-0193, Japan

2) CEA, IRFM, 13108 Saint-Paul-lez-Durance, France

3) Japan Atomic Energy Agency, Rokkasho, Aomori 039-3212, Japan

Development of plasma operation scenarios in JT-60SA has been progressing by using integrated modeling codes. Anomalous heat transport model, which are one of major uncertainties in the prediction, have been validated for ITB plasmas with full current drive (CD) condition in JT-60U and JET, and integrated codes TOPICS and CRONOS equipped with the models are used for the model verification. It is found that CDBM model predicts temperatures close to those in experiments or underestimates them, and thus can be used for the conservative prediction. By using TOPICS with CDBM model, JT-60SA ITB plasmas with high β_N and full CD condition have been predicted consistently with Ar seeding to reduce the heat load on divertor plates below 10 MW/m². In the prediction, TOPICS is coupled with impurity transport code IMPACT to examine the Ar core accumulation for the influx to the core and the separatrix density evaluated by integrated divertor code SONIC. The Ar accumulation is found to be so mild that the performance can be recovered by additional heating. Due to the strong dependence of accumulation on the pedestal density gradient, the high separatrix density is important for low accumulation as well as low divertor heat load.

1. Introduction

Validation of main models for plasma simulation is required for extrapolation to future devices (JT-60SA[1], ITER, DEMO). Such validation activities are being carried out through a JA-EU cooperation, especially for development of JT-60SA operation scenarios. JT-60SA scenarios should be based on experimental results of two machines that are the most similar for size & configuration: JT-60U & JET. JA and EU codes are used and thus models are verified between the codes. The best recipe to predict JT-60SA plasmas needs to be obtained. By using the recipe, plasma performance at I_p flattop phase is studied at first, and then operation scenarios with I_p ramp up/down are examined. The validation and verification (V&V) for H-mode and hybrid plasmas, and the prediction of these plasmas at I_p flattop phase have been done [2]. In this paper, we perform V&V and prediction for ITB plasmas with the full current drive (CD) condition at I_p flattop phase.

2. Validation and verification of heat transport models for ITB plasmas with full CD in JT-60U and JET

Anomalous heat transport model is one of major uncertainties in the prediction. Integrated codes TOPICS and CRONOS are used for the model verification and equipped with typical three anomalous transport models, CDBM (Current Diffusive Ballooning Mode, without ExB shear effect), BgB (Bohm / gyro-Bohm, CRONOS version, with ExB shear effect) and GLF23 (with α stabilization and internally calculated E_r). For the model validation, 3 shots in JT-60U and 1 shot in JET are chosen. Electron and ion temperature profiles are solved inside the pedestal ($\rho < 0.85$) starting from experimental profiles and then a stationary state is obtained.

Figure 1 shows an example of result. The CDBM results agree with experiments, but the BgB results are higher and the GLF ones are lower than the experiment. From all results including other shots, it is summarized that the CDBM results are close to or lower than experiments and thus CDBM can be used for the conservative prediction.

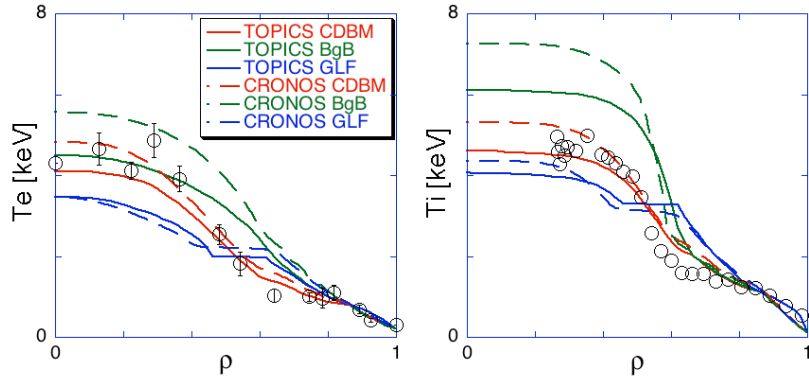


Fig.1. Comparison of electron (left) and ion (right) temperatures of simulations (lines) to experimental ones (symbols) for a JT-60U shot (48246)

3. Prediction of JT-60SA ITB plasmas with high β_N and full CD, consistent with impurity seeding to reduce divertor heat load

TOPICS with the CDBM model is used for the prediction of JT-60SA plasma. Pedestal profiles are determined on the basis of a pedestal width scaling and a stability check by a linear MHD code MARG2D [3]. Various states with high- β_N (>3.5) and nearly full CD condition can be obtained by using various sets of actuators (nearly-on or off-axis negative-ion-based NB (NNB), positive-ion-based NB (PNB), ECH/CD) in JT-60SA. Figure 2 shows an example of profiles with assumed $Z_{\text{eff}}=2$ with full-striped carbon. By using $P_{\text{NNB,off-axis}}=5\text{MW}$, $P_{\text{PNB}}=12\text{MW}$, $P_{\text{EC}}=7\text{MW}$ (110GHz for heating), a plasma with $H_H=1.68$, $\beta_N=3.90$, $f_{\text{BS}}=0.72$, $f_{\text{NB}}=0.22$, $f_{\text{OH}}=0.04$ ($V_{\text{loop}}\sim 3\text{mV}$) is obtained. The full CD scenario requires low separatrix density n_{esep} for high CD efficiency and low peak heat load q_{peak} on divertor plates. Analysis by integrated divertor code SONIC showed, for the total input power $P_{\text{in}}=37\text{MW}$ in initial and integrated research phases, the conditions can be satisfied by Ar seeding of $0.86\text{ Pa m}^3/\text{s}$ resulting in low n_{esep} ($\sim 1.46 \times 10^{19}\text{ m}^{-3}$) and low q_{peak} ($\sim 10\text{ MW/m}^2$) [4]. The Ar accumulation in the core may reduce the performance and should be studied. From the SONIC result, the Ar influx to the core is about $5 \times 10^{20}\text{ s}^{-1}$, which is the maximum because the value is not net flux and $P_{\text{in}} < 37\text{ MW}$ in the TOPICS simulation. To study the Ar core accumulation, TOPICS is coupled with impurity transport code IMPACT for multi impurity species and charge states where n_{esep} is set to the SONIC value (already in Fig.1), and neoclassical impurity diffusivities and convective velocities are calculated by NCLASS. Anomalous impurity diffusivities are set to $0.2\text{ m}^2/\text{s}$, which is neoclassical level (larger value reduces the accumulation), and convective velocities are zero. The intrinsic impurity carbon content is conserved from making initial $Z_{\text{eff}}=2$ and the effect of carbon transport only slightly reduces the performance. Figures 3 and 4 show profiles with the Ar influx to the core, which is assumed to be injected as neutrals in IMPACT. An inward pinch due to bulk density gradient exists in the core and a outward convection due to temperature gradient in the pedestal, resulting in Ar^{16-18+} accumulation in the core and the increase in the radiation power from 2.8 MW to 4.3 MW. The performance decreases, but can be recovered by adding the PNB power to supplement the radiation increase. Half reduction of n_{esep} keeping the pressure results in the inward pinch in all region and further decrease in the performance. The high n_{esep} is important for low accumulation.

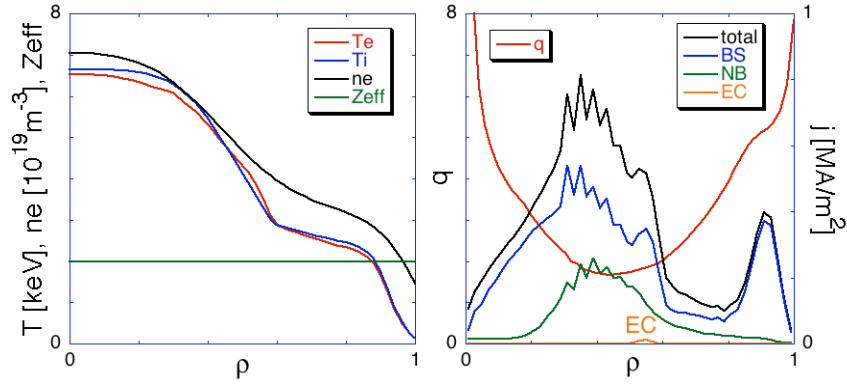


Fig.2. Profiles of temperatures, electron density, Z_{eff} (left) and safety factor, current densities (right) in a JT-60SA plasma with given $Z_{\text{eff}}=2$

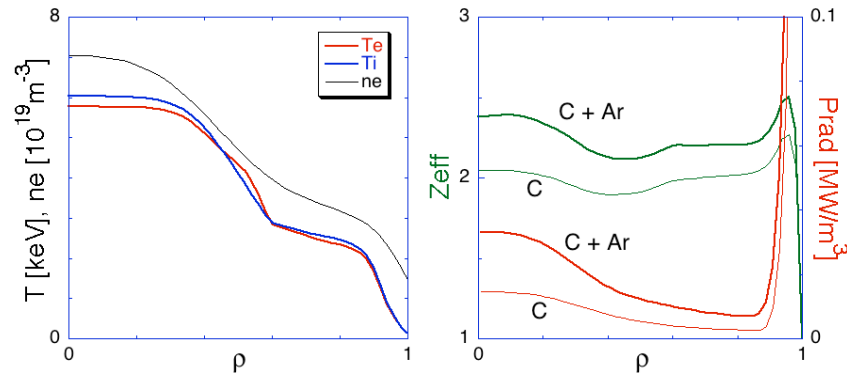


Fig.3. Profiles temperatures (left) and Z_{eff} and radiation powers (left) with C and Ar transport solved

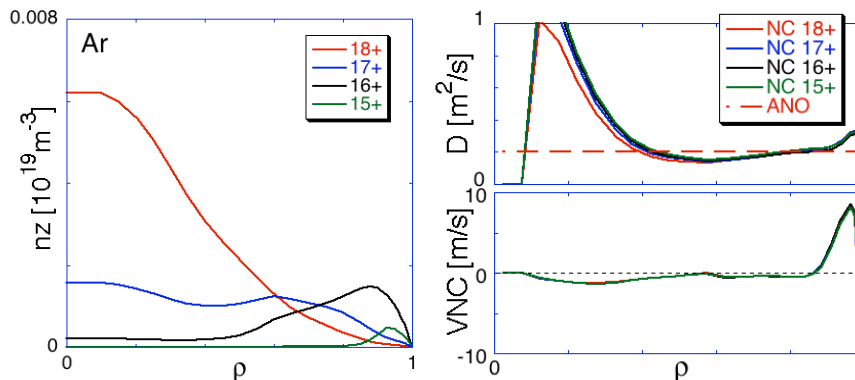


Fig.4. Profiles of Ar density, diffusivity and convective velocity for each charge state

Acknowledgments

This work was supported by a Grant-in-Aid for Scientific Research (C) (No 26420862) from the Japan Society for the Promotion of Science and was carried out using the HELIOS supercomputer at International Fusion Energy Research Centre, Aomori, Japan, under the Broader Approach collaboration between Euratom and Japan.

References

- [1] JT-60SA Research Plan v3.1, http://www.jt60sa.org/pdfs/JT-60SA_Res_Plan.pdf
- [2] J. Garcia et al.: Nucl. Fusion **54** (2014) 093010.
- [3] S. Ide et al.: Proc. 6th IAEA TM on Steady State Operation of Magnetic Fusion Devices, 2010
- [4] K. Hoshino et al.,: Contrib. Plasma Phys. **54** (2014) 404.

ソース変調に対するヒステリシス応答に関するシミュレーション研究

Simulation Study of Hysteresis in the Flux-Gradient Relation Responding to a Source Modulation

N. Kasuya, M. Sasaki, S. Inagaki, K. Itoh¹, M. Yagi² and S.-I. Itoh

Research Institute for Applied Mechanics, Kyushu University, Kasuga, Fukuoka 816-8580, Japan

¹ National Institute for Fusion Science, Toki, Gifu 509-5292, Japan

² Japan Atomic Energy Agency, Obuchi, Rokkasho-mura, Aomori 039-3212, Japan

E-mail: kasuya@riam.kyushu-u.ac.jp

There are reports indicating that ‘local closure’ of transport relation (in which flux at one-position is expressed uniquely by parameters/gradients at the same position) is violated in turbulent plasmas [1]-[4]. Candidates of the explanation include, e.g., meso-scale and macro-scale fluctuations [5]-[7], turbulence spreading [8]-[9], and dynamics in phase-space [10]. Here we study the mechanism that induces the observed mystery, hysteresis in gradient-flux relation [4], by a global nonlinear simulation of drift-interchange mode turbulence. The hysteresis in the gradient-flux relation is found in a global nonlinear simulation of heat modulation, and its mechanism is investigated [11].

In this study, drift-interchange modes in helical plasmas are analyzed using a reduced MHD model for stream function, toroidal component of the vector potential and total pressure [12]. This model is used as the fundamental one including the global and localized modes, nonlinear couplings with the Reynolds stress, and collisional transport processes. The following parameters are used: magnetic field $B_0 = 2.0$ [T], density $N = 1 \times 10^{19}$ [m⁻³], beta ratio $\beta = 0.03$, minor radius $a = 0.6$ [m], major radius $R_0 = 3.75$ [m], and specific heat ratio $\gamma = 5/3$. The rotational transform ι monotonically increases in radius from $\iota(0) = 0.51$ to $\iota(1) = 1.5$. Diffusion coefficients are set to 1×10^{-4} to model collisional transport processes. In the present simulation, the global energy confinement time τ_E is in the order of $1000 \tau_s$ and $\tau_s = 1.3t_A$, where the ion acoustic transit time is $\tau_s = a / c_s$, t_A is the Alfvén time, and c_s is the ion sound velocity. The confinement time τ_E has the time scale more than 10 times larger than that of the turbulence, such as the auto-correlation times ($\sim 10 \tau_s$) or the transit-time at diamagnetic velocity, $a / v_{\text{dia}} \sim 90 \tau_s$, which is related to the turbulent front propagation.

To clarify the dynamical response, source modulation is investigated. Simulations are performed with a grid of 1024 points in the radial direction. Fourier modes $-32 \leq m \leq 32$, $-8 \leq n \leq 8$ are taken, where m and n are the poloidal and toroidal mode numbers, respectively. Figure 1 (a) shows the time evolutions of the fluctuating internal energy $E_{p\,mm}$. Low (m, n) modes are excited in the linear growing phase, and saturation is obtained with energy exchanges between various modes by nonlinear couplings. The modulation of the source is made as shown in Fig. 1 (b) after $t \sim 2000$, where t is normalized with τ_s . The additional source is switched on and off cyclically as in Fig. 1 (c). The modulation cycle is set to be $800 \tau_s (= 1000 t_A)$, which is close to the energy confinement time.

There exist large pressure fluctuations, so superposition of source modulation cycles is necessary to obtain sufficient statistical convergence. The random fluctuation can be eliminated by this conditional averaging. The calculation up to $t = 93000$ (~ 100 times of τ_E)

has been carried out that includes over 100 cycles of the modulation to confirm statistical convergence. At $r = 0.2$, there is the direct change of the source, which gives the immediate response of all the physical quantities. In the middle region, the direct source change is negligibly small, so it is possible to observe how the modulation propagates from the center. At $r > 0.4$ the response of the flux has time delay from $t = 0$. The front propagation velocity is given to be $v_p = (0.008 \pm 0.002) a / \tau_s$. This velocity gives the typical time scale $a / v_p \sim 100 \tau_s$, which is close to the transit time by the diamagnetic velocity $90 \tau_s$. The heat flux begins to increase as the pressure gradient increases, and vice versa. At $r = 0.6$ the increase of the heat flux is accelerated from $t \sim 30$, continuing to increase after the settlement of the pressure gradient. This response gives a hysteresis in the counter-clockwise in the gradient-flux relation (Fig. 2). The changes of the pressure gradient and the heat flux are settled in $t_{up} \sim 200 \tau_s$. We conclude this observed hysteresis as the break-down of the diffusive model, owing to the competition of the two time scales. Note that the existence of the hysteresis is confirmed by examining the convergence of its width against the number of modulation repetition. The width is converged over 40 cycles in this case. In the region $r > 0.8$, the turbulent transport is small, and the diffusive transport process is dominant by the selection of the boundary condition.

The response of transport to the modulation can be explained by two processes. One is that mediated by a global mode. Figure 3 shows the radial structures of mode amplitudes and of driven-fluxes by the modes. The mode amplitudes of low m, n modes, such as $(m, n) = (1, 1)$ and $(2, 1)$, spread broadly in the radial direction and have the auto-correlation time of $30 \tau_s$ (global mode), and those of medium m, n modes, such as $(5, 5)$ and $(8, 6)$, are localized near their rational surfaces and have the auto-correlation time of $10 \tau_s$ (micro mode) [13]. Even though the global mode $(2, 1)$ spreads broadly, its flux is dominant only in the central part $r < 0.4$. In the outer region, at $0.5 < r < 0.7$, the pressure and potential fluctuations have the phase close to each other, so this mode does not drive the mean flux. On the other hand, this global mode mediates the energy exchange to higher m modes. At $r = 0.6$ the change of the amplitude reaches in $t \sim 30$, which leads nonlinear energy transfer to the other modes. This redistribution of the energy is taken place in a finite duration related to the turbulence correlation time, which makes the flux keep increasing even after the settlement of the pressure gradient change. In addition, the dominant contribution at $r \sim 0.6$ is $(2, 1) \leftarrow (8, 6) + (-6, -5)$, and the direction of the energy transfer shows that it extracts the energy from micro modes. The global mode can play a role as the mediator of seesaw mechanism [14] in the turbulent transport, i.e., the increase of the mode amplitude owing to the stronger drive at the core region can suppress the fluctuations at different radii. The amplitude of the $(2, 1)$ mode starts to increase at the onset of heating, which induces the increment of transport flux at the core ($r < 0.4$), while the change of amplitude propagates to outer region $0.5 < r < 0.7$ at the speed of group velocity so as to reduce the energy of micro modes. These features can give the delay of the flux response from the pressure gradient response, and induce the non-diffusive response in the heat modulation. Micro modes also cause the non-diffusive response. Owing to the array configuration of transport by such modes, the successive change of the flux propagates to the outer region. The heat source modulation directly affects the global mode $(2, 1)$, and the simultaneous response takes place in its width $r < 0.4$, though there is little change outside of the width. The pressure gradient increases in accordance with the change of the flux, and propagates to the outer region. Then, the unstable micro modes begin to increase. The typical time scale for the response of the micro modes is also given by that of the front propagation. Combining the response induced via the global mode and the successive change of micro modes, the change of the mean pressure gradient precedes that of

the turbulent intensity and turbulence-drive flux in the outer region $0.5 < r < 0.7$, as in the case of the turbulence spreading [9].

In the present global nonlinear simulation, the hysteresis in the gradient-flux relation is found to appear owing to the global mode and the front propagation mechanism. The obtained hysteresis is in the counter-clockwise, which is opposite to the experimental observation [4]. In the simulation, the global mode (2, 1) absorbs the energy from microscopic fluctuations without inducing the radial flux by itself in the region of $0.5 < r < 0.7$. Thus increasing the amplitude of the (2, 1) mode over the whole plasma column after the onset of heating works to suppress the microscopic turbulence in the region of $0.5 < r < 0.7$. In contrast, the fluctuations in that region increase immediately after the onset of the additional heating in the experiment. This implies the possibility that variety of hysteresis responses will be observed

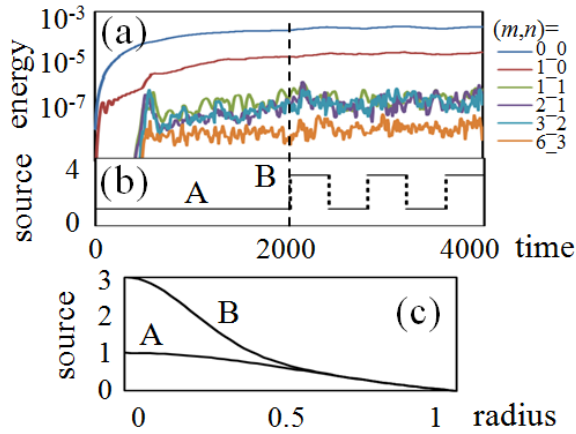


FIG 1. Nonlinear saturation and heat modulation. Time evolutions of the energy of Fourier modes are shown, when the source modulation is applied after $t = 2000$. (a) The mean and fluctuating internal energies, and (b) the magnitude of the source at $r = 0$, normalized with the value at $t = 0$, are plotted. (c) The radial profiles of the source during the modulation are also shown.

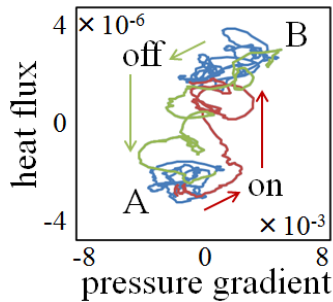


FIG 2. Hysteresis in local parameters. Relationship between the pressure gradient and heat flux at $r = 0.6$ is shown.

Acknowledgements

This work is supported by the Grant-in-Aid for Young Scientists (24760703), for Scientific Research (23244113) of JSPS, by the collaboration program of NIFS (NIFS13KNST050, NIFS13KOCT001) and of RIAM of Kyushu University.

in fusion plasmas. In future experiments, one can identify the radial profiles of the flux by the global mode itself and of the energy transfer from microscopic modes to the global mode. It is also necessary to extend the simulation models to include the phase-space coupling of turbulence with heating as was pointed out in, e.g., [10].

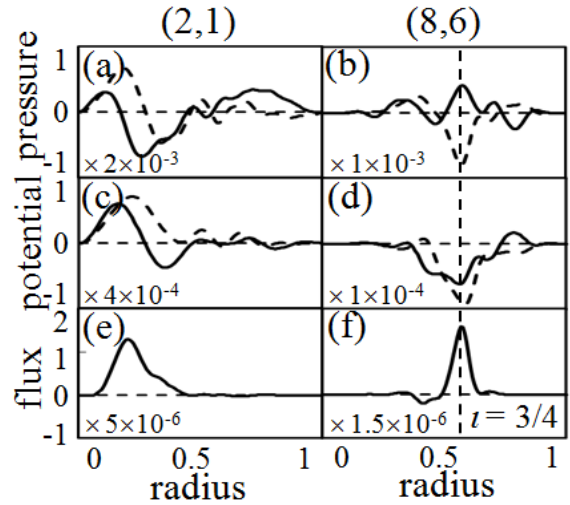


FIG 3. Mode structures. (a - d) Snapshots of the eigenfunction of the (2, 1) and (8, 6) mode of the pressure and potential at $t = 2400$ are shown, where solid and dashed lines represent the real and imaginary part, respectively. (e, f) Snapshots of the heat flux given by the (2, 1) and (8, 6) mode are also shown. The vertical dashed line in (b, d, f) represents the position where the resonance rational surface $3/4$ exists.

References

- [1] K. Gentle, *et al.*, Phys. Rev. Lett. **74**, 3620 (1995)
- [2] U. Stroth, *et al.*, Plasma Phys. Control. Fusion **38**, 611 (1996)
- [3] N. Tamura, *et al.*, Nucl. Fusion **47**, 449 (2007)
- [4] S. Inagaki, *et al.*, Nucl. Fusion **53**, 113006 (2013)
- [5] See theoretical reviews, e.g. P. H. Diamond, *et al.*, Plasma Phys. Control. Fusion **47**, R35 (2005). See experimental reviews, e.g. A. Fujisawa, *et al.*, Nucl. Fusion **47**, S718 (2007)
- [6] S. Inagaki, *et al.*, Phys. Rev. Lett. **107**, 115001 (2011)
- [7] K. Itoh, *et al.*, Plasma Phys. Control. Fusion **54**, 095016 (2012)
- [8] T. S. Hahm, *et al.*, Plasma Phys. Control. Fusion **46**, A323 (2004)
- [9] X. Garbet, *et al.*, Phys. Plasmas **14**, 122305 (2007)
- [10] S.-I. Itoh and K. Itoh, Sci. Rep. **2**, 860 (2012)
- [11] N. Kasuya, *et al.*, Phys. Plasmas **21**, 110701 (2014)
- [12] N. Kasuya, *et al.*, Plasma Fusion Res. **8**, 2403070 (2013)
- [13] N. Kasuya, *et al.*, Plasma Fusion Res. **6**, 1403002 (2011)
- [14] K. Itoh, *et al.*, J. Plasma Fusion Res. SERIES **8**, 119 (2009)

Radio-frequency sheath-plasma interactions in a semi-realistic tokamak model

Haruhiko Kohno^{1,*}, James R. Myra² and Daniel A. D'Ippolito²

¹Department of Mechanical Information Science and Technology, Kyushu Institute of Technology
680-4 Kawazu, Iizuka, Fukuoka 820-8502, Japan

²Lodestar Research Corporation, 2400 Central Avenue P-5, Boulder, Colorado 80301, USA

*Author to whom correspondence should be addressed E-mail: kohno@mse.kyutech.ac.jp

ABSTRACT

A numerical code that solves self-consistent radio-frequency (RF) sheath-plasma interactions in the ion cyclotron range of frequencies (ICRF) has been developed based on a finite element method. In this study, we investigate fast-wave propagation and RF sheath interaction with a tokamak wall using a two-dimensional quasi-circular domain with a limiter-shaped bump. It is found that strong sheath interaction occurs where the contact angle between the magnetic field line and the wall rapidly changes at the poloidal edges of the bump. This physical phenomenon is consistent with the experimental observation in Alcator C-Mod. The important mechanism for the strong sheath interaction is the conversion from a fast wave to a slow wave on the curved wall, which generates a large electric field component parallel to the background magnetic field and thereby high local sheath voltage that can potentially induce ion sputtering at the conducting surface.

Keywords: Radio-frequency sheaths, Plasma waves, Magnetic confinement fusion, Finite element method

1. INTRODUCTION

Radio-frequency (RF) waves in the ion cyclotron range of frequencies (ICRF) have been successfully applied to various heating experiments in fusion plasmas. However, it has been revealed by experimental and theoretical studies that deleterious edge plasma interactions can occur due to various nonlinear mechanisms [1]. One of the most important nonlinear effects is RF sheath formation, in which the sheath potential on the walls and limiters of the tokamak device is enhanced by the ICRF waves. RF sheath formation causes various problems including impurity generation by enhanced sputtering and power dissipation in the scrape-off layer (SOL), leading to local hot spots and reduced power. Because sheaths occur on the scale of the Debye length, which is much smaller than domain sizes or RF wavelengths of interest for fusion applications, approximate RF sheath boundary condition (sheath BC) approaches have been developed [2,3]. These approaches effectively treat the sheath as a thin vacuum layer, and thus capture the important effect of sheath capacitance on the boundary. In addition, a finite element code employing this sheath BC has been developed by the authors for the purpose of solving self-consistent RF sheath-plasma interactions in the ICRF [4,5]. In this short paper, we will briefly summarize our recent numerical analysis of propagating fast waves (FWs) and sheath interactions in the poloidal domain of a semi-realistic tokamak.

2. MATHEMATICAL MODELING

The governing equation for plasma waves is a combined form of Maxwell's equations described as

$$\nabla \times \nabla \times \mathbf{E} - \frac{\omega^2}{c^2} \boldsymbol{\varepsilon} \cdot \mathbf{E} - i\omega\mu_0 \mathbf{J}_{\text{ext}} = \mathbf{0}, \quad (1)$$

where the electric field \mathbf{E} and the external current \mathbf{J}_{ext} vary on the RF time scale. Here, ω is the applied ICRF wave frequency, c is the speed of light, and μ_0 is the permeability in vacuum. The dielectric tensor $\boldsymbol{\varepsilon}$ is given based on the cold plasma model. At the metal wall, the sheath effect is taken into account by means of a sheath BC [2,3], which is written as follows:

$$\mathbf{E}_t = \nabla_t \left(\frac{\Delta_{\text{sh}}}{\varepsilon_{\text{sh}}} D_n \right). \quad (2)$$

Here, Δ_{sh} is the time-averaged sheath width, ε_{sh} is the dielectric constant in the sheath, D_n is the component of the electric displacement normal to the sheath, and the subscript t denotes the two components tangential to the boundary. The sheath width is expressed as follows:

$$\Delta_{\text{sh}} = \left(\frac{eC_{\text{sh}}}{\varepsilon_{\text{sh}}T_e} |D_n| \right)^3 \lambda_{\text{De}}^4 + C_{\text{th}} \lambda_{\text{De}}, \quad (3)$$

where C_{sh} is an order-unity constant giving the rectification factor, T_e is the electron temperature, and λ_{De} is the electron Debye length. See Ref. [4] for details.

3. RESULTS OF NUMERICAL SIMULATION

In recent Alcator C-Mod experimental work, large plasma potentials (~ 100 V) were measured on magnetic field lines connecting the emissive probe to a nearby plasma limiter [6]. This plasma potential rose rapidly in the vicinity of the limiter tip and then decayed exponentially along the major radius direction behind the limiter tip. To investigate the cause of this local high potential, we consider (so far linear) solutions of the interactions between propagating FWs and sheaths using typical Alcator C-Mod parameters in the two-dimensional finite element numerical analysis. Figure 1 shows the filled contour plot of the real part of $E_{\perp y}$, which is the electric field y -component perpendicular to the magnetic field lines, in the quasi-circular domain corresponding to the poloidal cross-section of the Alcator C-Mod tokamak. Here, the antenna and magnetic field lines are also superimposed on the plot. It is observed that the FW propagates across the magnetic field lines and reaches the limiter-shaped protrusion on the left-hand side of the domain. Figure 2 shows the enlarged contour plot of the real part of E_{\parallel} , which is the electric field component parallel to the magnetic field lines, near the poloidal edge of the limiter-shaped protrusion. Since this is a plot of E_{\parallel} and thus the FW contribution is considered to be negligible, one can confirm that the FW is converted into the slow wave (SW) where the contact angle between the magnetic field line and the wall rapidly changes. This conversion makes the local sheath voltage sufficiently high as confirmed in Fig. 3 (see the result for $\delta a = 0.03$ m). Figure 3 also shows that the maximum local sheath voltage increases with the increase of the bump height δa .

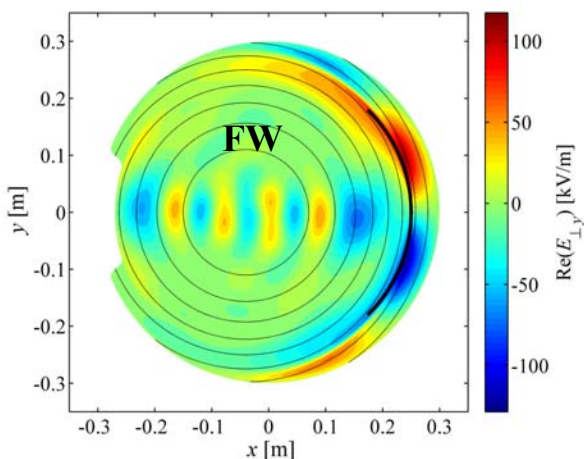


FIG. 1. Filled contour plot showing the distribution of an electric field component perpendicular to the background magnetic field.

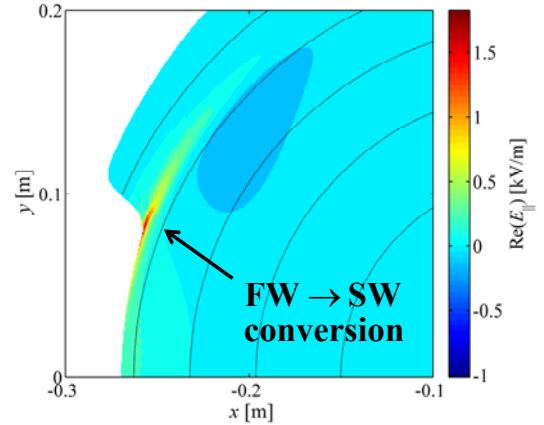


FIG. 2. Enlarged plot of the parallel electric field component near the poloidal edge of the limiter-shaped protrusion. This plot shows the conversion of the FW to the SW where the contact angle between the magnetic field line and the wall rapidly changes.

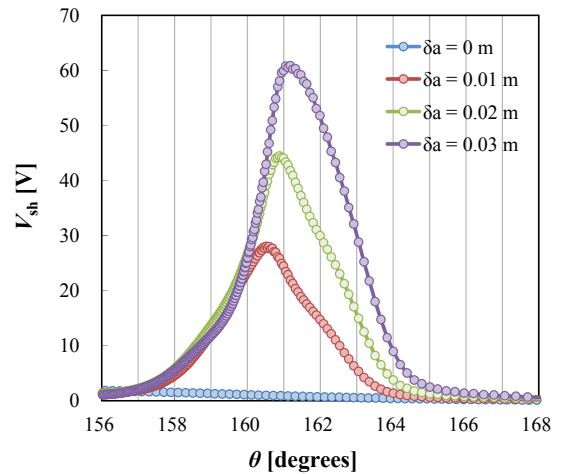


FIG. 3. Comparison of the RF sheath voltage near the limiter tip as a function of the poloidal angle.

REFERENCES

- [1] J. R. Myra, D. A. D'Ippolito, D. A. Russell, L. A. Berry, E. F. Jaeger, and M. D. Carter, Nucl. Fusion **46**, S455 (2006).
- [2] J. R. Myra, D. A. D'Ippolito, and M. Bures, Phys. Plasmas **1**, 2890 (1994).
- [3] D. A. D'Ippolito and J. R. Myra, Phys. Plasmas **13**, 102508 (2006).
- [4] H. Kohno, J. R. Myra, and D. A. D'Ippolito, Comput. Phys. Commun. **183**, 2116 (2012).
- [5] H. Kohno, J. R. Myra, and D. A. D'Ippolito, Phys. Plasmas **20**, 082514 (2013).
- [6] R. Ochoukov, et al., Plasma Phys. Control. Fusion **56**, 015004 (2014).

NBI Heating Analysis in Multi-Ion-Species Plasma in LHD

Hiroyuki YAMAGUCHI, Sadayoshi MURAKAMI

Department of Nuclear Engineering, Kyoto University, Nishikyo, Kyoto 615-8530, Japan

1 Introduction

In the Large Helical Device (LHD) experiment, high ion temperature (high- T_i) up to 8 keV has been achieved applying helium gas puffing and carbon pellet injection to the NBI-heated plasma. [1, 2]. The wall conditioning by RF waves enhance the ion temperature. To accurately evaluate the heat deposition profile of each particle species in this high- T_i plasma, we have to take into account the impurity effect on the beam ion birth and the collisional slowing down.

In this study we perform numerical simulations of the NBI heating in multi-ion-species plasmas of LHD. We consider two typical impurity ions in the high- T_i experiment: He^{2+} and C^{6+} ions. Ionization of the fast neutrals by impurity impact and charge exchange with the impurity is taken into account in the neutral beam attenuation calculation. We also evaluate the beam ion distribution function in five-dimensional phase space using the GNET code[3] taking into account the guiding-center motion in the three-dimensional magnetic configuration of LHD and the Coulomb collisions with the impurity ions.

2 Simulation Models

We evaluate the fast-ion birth profile in LHD plasmas using the HFREYA code, which is a part of the FIT3D code[4]. The geometry of the LHD plasma is introduced using the MHD equilibrium by the VMEC code. We use the approximate form of the beam stopping cross-section in plasma with several of the impurity ion species proposed in ref [5], where they considered the ionization of neutrals owing to electron impact, proton impact, impurity impact, and charge exchange with proton and impurity ions, including various excitation processes of neutrals.

The slowing down is calculated using the GNET code which is based on the orbit-following Monte Carlo algorithm and solves the drift kinetic equation in five-dimensional phase space (3-D in real and 2-D in velocity space),

$$\frac{\partial f_{\text{fast}}}{\partial t} + (\mathbf{v}_{\parallel} + \mathbf{v}_{\text{D}}) \cdot \nabla f_{\text{fast}} + \dot{\mathbf{v}} \cdot \nabla_{\mathbf{v}} f_{\text{fast}} = C(f_{\text{fast}}) + L + S. \quad (1)$$

In the above equation, f_{fast} is the fast-ion distribution function, \mathbf{v}_{\parallel} is the velocity parallel to the field line, \mathbf{v}_{D} is the perpendicular drift velocity, $C(f_{\text{fast}})$ is the linear Coulomb collision operator, L is the particle loss term consisting of the orbit loss, charge exchange loss, and the thermalization. The particle source term, S , is calculated with the HFREYA code. To consider the effect of impurity ions on the slowing down of the fast ions, we introduce the linear Coulomb collision operator for multi-species plasma as the sum of the operators for electrons, protons, and impurity ions:

$$C(f) = C_e(f) + C_p(f) + \sum_{\text{imp}} C_{\text{imp}}(f), \quad (2)$$

where $\text{imp} = \text{He}^{2+}, \text{C}^{6+}$ and the operators for each particle species are given by ref[6] as

$$C_s(f) = \frac{v_d^s}{2} \frac{\partial}{\partial \lambda} (1 - \lambda^2) \frac{\partial f}{\partial \lambda} + \frac{1}{v^2} \frac{\partial}{\partial v} \left[v^2 \nu_E^s \left(v f + \frac{T_s}{m_b} \frac{\partial f}{\partial v} \right) \right],$$

where s is the particle species, $\lambda = v_{\parallel}/v$ is the cosine of the pitch angle, ν_d^s is the pitch angle scattering frequencies, ν_E^s is the energy scattering frequencies, T_s is the temperature, and m_b is the fast-ion mass, respectively.

3 Simulation Results

We assume the typical parameters of the magnetic configuration in the high- T_i experiment in LHD: The magnetic axis is $R_{\text{ax}} = 3.6$ m and the magnetic field strength at the center is $B_0 = -2.85$ T. The radial profiles of the electron density and electron temperature are $n_e(\rho) = n_{e0}(1 - 0.9 \times \rho^8) \times 10^{19} \text{m}^{-3}$ and $T_e(\rho) = 3 - 2.7\rho^2$ keV, respectively, where $\rho = r/a$ is the normalized minor radius. We assumed that the ion temperature is the same value as the electron temperature. We also assumed that the impurity composition is uniform and the ratio of the proton density to He^{2+} density was 2:1.

First, we fixed the birth profile of the beam ions and studied the impurity effect on the beam confinement. Figure 1 shows the beam ion distribution functions of NB#1 in the velocity space at $r/a = 0.2$. The electron density is $n_{e0} = 1 \times 10^{19} \text{m}^{-3}$ and the value of Z_{eff} is 1.5 in the left and 3.6 in the right figure. The ‘holes’ near the origin come from the thermalization. In the case of the higher carbon fraction, $Z_{\text{eff}} = 3.6$, the pitch angle scattering take place at higher energy and there are less beam ions in the velocity region $\sim 2 \times 10^6 \text{ms}^{-1}$ than in the case of $Z_{\text{eff}} = 1.5$. This can be seen more clearly in the left of Figure 2, where the distribution function is plotted for v_{\parallel}/v . The enhancement of the pitch-angle scattering results in the increase in the orbital energy-loss rate, from 2% at $Z_{\text{eff}} = 1.5$ to 8% at $Z_{\text{eff}} = 3.6$ in the case of the co-NBI, as seen in the middle and right of Figure 2.

Next we took into account the change in the birth profile by the impurity ions. The radial profiles of the heat deposition to each particle species are shown in Figure 3. The electron density and temperature are $n_{e0} = 1 \times 10^{19} \text{m}^{-3}$ and $T_{e0} = 3$ keV, respectively. We have obtained center-peaked profiles for each particle species in the case of NB#1 and broad profiles in the case of NB#5.

4 Summary

We have performed NBI heating simulations in multi-ion-species plasmas in LHD. In this study, we have considered two typical impurity ions in the high- T_i experiment: He^{2+} and C^{6+} . The 5-D phase space simulation of the beam ion slowing down using the GNET code have shown that these impurity ions deteriorate the NBI beam ion confinement by increasing the effective deflection frequency. When $n_e = 1 \times 10^{19} \text{m}^{-3}$, the orbital energy-loss rate increased linealy from 2% at $Z_{\text{eff}} = 1.5$ to 8% at $Z_{\text{eff}} = 3.6$ in the case of the co-NBI. The orbital energy-loss rate of the perp-NBI, which generates fast ions predominantly in the trapped region, reached 14% at $Z_{\text{eff}} = 3.6$ for the same electron density. We also have obtained the center-peaked heat deposition profiles for each species in the case of NB#1 and the broad profiles in the case of NB#5. In future, we will perform an NBI heating simulation of the high- T_i experiment, taking into account the effect of the plasma time evolution and the impurity effect.

References

- [1] H. Takahashi *et al.*, Nucl. Fusion **53**, 073034 (2013).

- [2] K.Nagaoka *et al.*, Nucl. Fusion **51**, 083022 (2011).
- [3] S. Murakami, et al., Nucl. Fusion **46**, S425 (2006).
- [4] S. Murakami *et al.*, Fusion Technology **27** Suppl. S 256 (1995).
- [5] R. K. Janev *et al.*, Nuclear Fusion **29** 2125 (1989).
- [6] A. H. Boozer and G. Kou-Petavic, Phys. Fluids **24** 851 (1981)

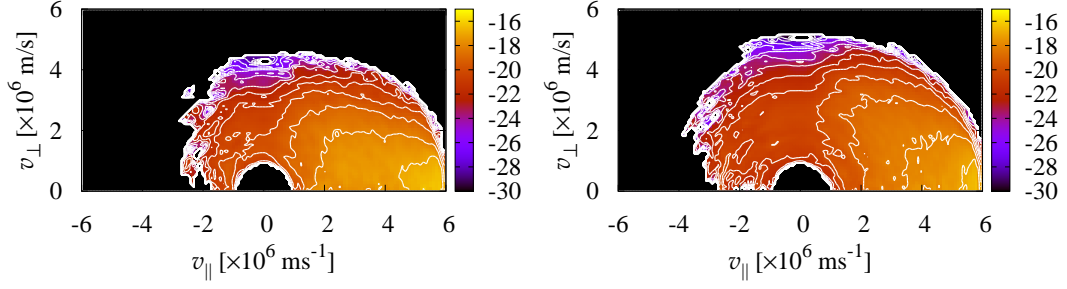


Figure 1: The beam ion distribution function of NB#1, at $r/a = 0.2$, in the velocity space. The value of Z_{eff} is 1.5 in the left and 3.6 in the right figure case.

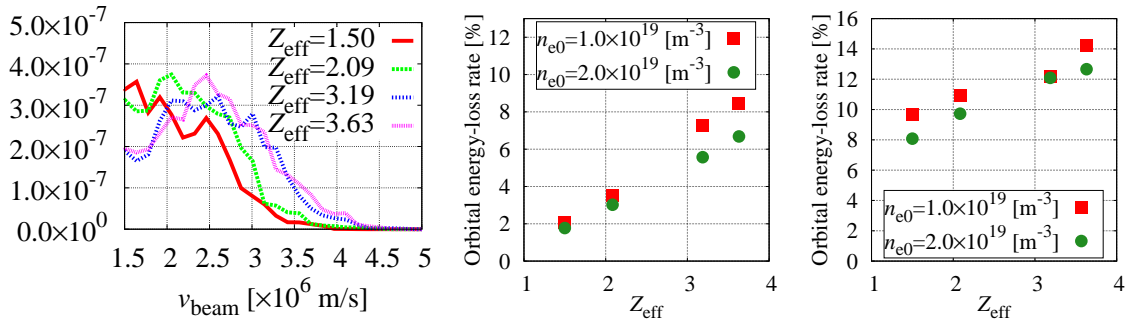


Figure 2: The beam ion distribution function of NB#1, at $r/a = 0.2$, for $v_{\parallel}/v = 0$ (left) and the orbital energy-loss rate for NB#1 (middle) and NB#5 (right).

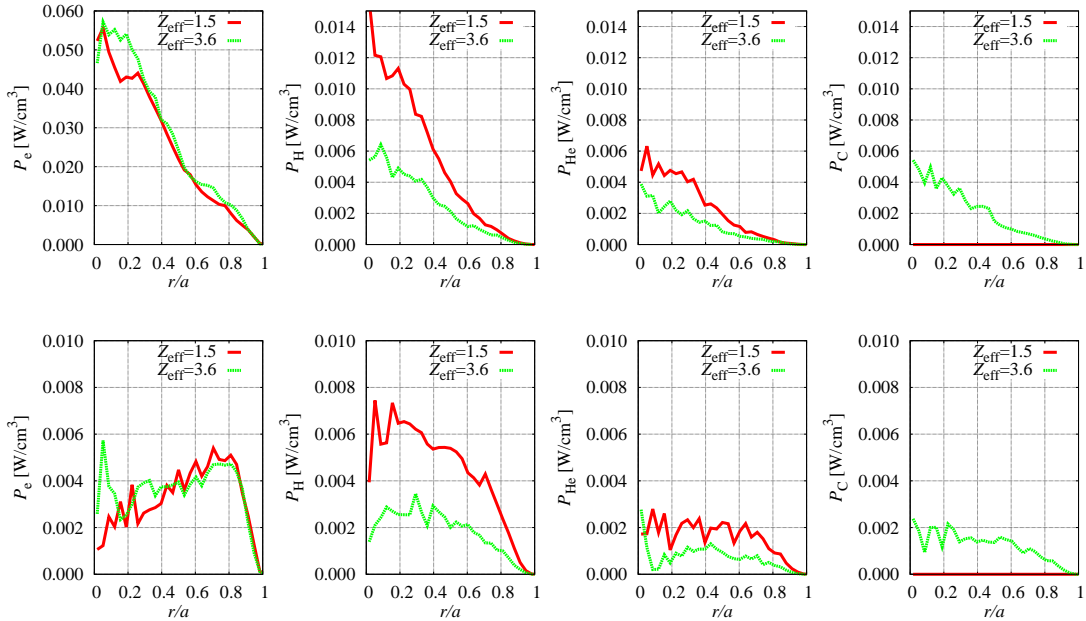


Figure 3: The radial profile of the heat deposition for NB#1 (top) and NB#5 (bottom).

Development of L-H Transition Simulation Framework with BOUT++ Code

Haruki SETO, Masatoshi YAGI and George BREYIANNIS*

Rokkasho Fusion Research Institute, Japan Atomic Energy Agency, Aomori 039-3212, Japan

BOUT++ is a nonlinear 3-dimensional turbulence/MHD code that can be applicable to any axisymmetric geometry and can employ any physics model. It can provide a simulation framework for the investigation of the L-H transition by implementing a reduced MHD model including a mechanism determining the radial electric field by the radial force balance. In this study we have developed a BOUT++ physics module for the first principal simulation of the L-H transition BOUT++_LH based on a 2-field reduced MHD model. We report the derivation of the 2-field L-H transition model and its preliminary simulation results.

1 Introduction

Understanding the L-H transition mechanism¹ is one of the key issues for the prediction of the confinement performance of magnetic confinement fusion devices. The integrated transport simulation (ITS) framework with the current diffusive ballooning mode (CDBM) turbulence transport model² for the L-H transition was therefore developed and accomplished the qualitative evaluations of the L-H transition such as the spontaneous quench of the thermal diffusivity and the self-consistent formation of the pedestal pressure at the edge region.³ The quantitative evaluation of the L-H transitions such as the prediction of the pressure at the pedestal top and the power threshold for the L-H transition, however, has been still unsolved and requires further improvement of turbulent transport models within the ITS framework or development of a new simulation framework from first principals.

Recently 3-dimensional flux-driven simulations of the L-H transition by the 2-field (vorticity and pressure) reduced MHD (RMHD) model have been reported by several research groups independently.^{4,5} Their work is based on the following key features, 1) the electrostatic resistive ballooning turbulence (RBM) described by the 2-field RMHD model, 2) the radial force balance of the ion species generating the strongly sheared radial electric field implemented by the poloidal damping term, and 3) the self-consistent evolution of the pressure determined by the dynamic balance between the energy source and sink term.

A nonlinear 3D edge turbulence/MHD code BOUT++^{6,7} has been developed for analyzing the edge localized modes (ELMs)^{8,9} in arbitrary curvilinear geometries but it also provides a first principal simulation (FPS) framework for investigating the L-H transition.⁵ We have been developing a

BOUT++ physics module BOUT++_LH for the L-H transition simulation incorporating the CDBM turbulence¹⁰ based on the 3-field RMHD model including the poloidal damping, electron inertia and current diffusive effects. The FPS of the L-H transition with CDBM turbulence may also improve the CDBM turbulent transport model through the comparison with the ITS of the L-H transition.

In this paper, we report preliminary simulation results of a 2-field L-H transition model by BOUT++_LH as a first step for the FPS of the L-H transition with the CDBM turbulence. This paper is organized as follows. In section 2, the brief derivation of the 2-field L-H transition model is described with the emphasis on the derivation of the poloidal damping term. Preliminary simulation results by the 2-field L-H transition model by BOUT++_LH are shown in section 3. Finally the conclusion is summarized in section 4.

2 2-field L-H transition model

In this paper, we employ a 2-field RMHD¹¹ consisting of Eq.(1) and Eq.(2) as a L-H transition model,

$$m_i n_i \frac{\partial U_E}{\partial t} = -m_i n_i \left[\frac{\phi}{B_0}, U_E \right] + B_0^2 \nabla_{\parallel} \left(\frac{J_{\parallel}}{B_0} \right) + 2\mathbf{b}_0 \times \boldsymbol{\kappa} \cdot \nabla_{\perp} P + m_i n_i \mu_{\perp} \nabla_{\perp}^2 U_E - \mathbf{b} \cdot \nabla \times \nabla \cdot \vec{\Pi}_{i\parallel} \quad (1)$$

$$\frac{\partial P}{\partial t} = - \left[\frac{\phi}{B_0}, P \right] + \chi_{\perp} \nabla_{\perp}^2 P + \chi_{\parallel} \nabla_{\parallel}^2 P + S_p - PL_p, \quad (2)$$

m_i is the ion mass, $n_i = \text{const.}$ is the ion number density, $U_E = \nabla_{\perp}^2 (\phi/B_0)$ is the vorticity, t is the time, ϕ is the electrostatic potential, B_0 is the equilibrium magnetic field intensity, $J_{\parallel} = \eta^{-1} \nabla_{\parallel} \phi$ is the parallel current density, η is the resistivity, $\mathbf{b}_0 = \mathbf{B}_0/B_0$ is the unit

*current address: European Commission - JRC, Ispra(VA), Italy
author's e-mail: seto.haruki@jaea.go.jp

vector in \mathbf{B}_0 direction, $\boldsymbol{\kappa} = \mathbf{b}_0 \cdot \nabla \mathbf{b}_0$ is the curvature vector, P is the plasma pressure, μ_{\perp} is the perpendicular viscosity, $\overleftrightarrow{\Pi}_{\parallel}$ is the ion parallel viscous tensor, χ_{\perp} is the perpendicular diffusivity, χ_{\parallel} is the parallel diffusivity, S_p is the energy source, PL_p is the energy sink, $[f, g] = \mathbf{b}_0 \cdot \nabla_{\perp} f \times \nabla_{\perp} g$ is the Poisson bracket, and ∇_{\perp} is the perpendicular gradient operator, ∇_{\parallel} is the parallel gradient operator respectively.

In the 2-field L-H transition model, the novel term is the contribution from the parallel viscous tensor to the vorticity equation $\mathbf{b} \cdot \nabla \times \nabla \cdot \overleftrightarrow{\Pi}_{\parallel}$ and this term results in the poloidal damping term describing the relaxation of the ion poloidal flow to the ion neoclassical poloidal flow.^{4,5} Since the detailed derivation of the poloidal damping term has not been reported yet, we derive the poloidal damping term from the heuristic closure for the parallel viscous force,¹² the radial force balance of ion and the parallel force balances in the neoclassical transport theory^{13,14} in this section.

The heuristic closure for the parallel viscous force¹² is employed as

$$\nabla \cdot \overleftrightarrow{\Pi}_{\parallel} = m_i n_i \frac{\langle B^2 \rangle}{B_{\theta}^2} (\mu_{i1} V_{i\theta} + \mu_{i2} W_{i\theta}) \mathbf{e}_{\theta} \quad (3)$$

$$\mathbf{W}_i = 2\mathbf{q}_i / 5P_i, \quad (4)$$

where μ_{i1} and μ_{i2} are the ion parallel neoclassical viscosity coefficients,¹⁴ V_i is the particle flow, \mathbf{W}_i is the heat flow, \mathbf{q}_i is the heat flux, and $\langle \rangle$ indicates the flux surface averaged (FSA) quantity. The second term in Eq.(3) is the additional term describing the contribution from the heat flow to the parallel viscosity and results in the offset neoclassical poloidal flow.¹⁵ In Eq.(3), the local orthogonal torus coordinate (ψ, θ, ζ) is employed, where ψ is the poloidal flux function, θ is the poloidal angle, ζ is the geometrical toroidal angle. The magnetic field \mathbf{B} can be expressed in (ψ, θ, ζ) coordinates as

$$\mathbf{B} = \nabla \zeta \times \nabla \psi + B_{\zeta} \nabla \zeta, \quad (5)$$

$$\mathbf{B}_0 = B_{\zeta} \nabla \zeta = B_0 \mathbf{b}_0, \quad (6)$$

$$B_i^2 \sim B^2 \sim \langle B^2 \rangle \sim B_0^2, \quad B_i^2 \gg B_p^2. \quad (7)$$

In the 2-field L-H transition model, the ion covariant poloidal flow $V_{i\theta}$ is determined by the mean radial force balance,

$$\nabla \psi \cdot \nabla \bar{P}_i = e_i n_i (\bar{\mathbf{E}} + \mathbf{V}_i \times \mathbf{B}) \cdot \nabla \psi \quad (8)$$

which results in

$$V_{i\theta} = \frac{\sqrt{g} B_0 g^{\psi\psi}}{B_{\zeta}} \frac{d}{d\psi} \left(\frac{\bar{\phi}}{B_0} + \frac{\bar{P}_i}{e_i n_i B_0} \right), \quad (9)$$

where $\bar{}$ indicates the mean quantity. In the derivation of Eq.(9), we have assumed the negligibly small

toroidal rotation, which is valid in the case where there are no auxiliary momentum sources such as neutral beam injection (NBI).

On the other hand, the ion covariant poloidal heat flow $W_{i\theta}$ is determined by the mean parallel force balances of the pure ion plasma. According to the Hirshman's moment approach,¹⁴ the parallel force balances of the ion can be expressed by

$$\hat{\mu}_{i1} \hat{V}_{i\theta} + \hat{\mu}_{i2} \hat{W}_{i\theta} = 0 \quad (10)$$

$$\hat{\mu}_{i2} \hat{V}_{i\theta} + \hat{\mu}_{i3} \hat{W}_{i\theta} = \hat{l}_{22}^{ii} \left[\hat{W}_{i\theta} + \frac{B}{\langle B^2 \rangle} \left(-\frac{B_{\zeta}}{e_i B} \frac{d\bar{T}_i}{d\psi} \right) \right], \quad (11)$$

where $\hat{\mu}_{ii} = (3\langle (\nabla_{\parallel} B)^2 \rangle / \langle B^2 \rangle) \mu_{ii}$ is the normalized neoclassical parallel viscosity coefficient, \hat{l}_{22}^{ii} is the neoclassical friction coefficient, and $\hat{V}_{i\theta} = V_i^{\theta} / B^{\theta}$ and $\hat{W}_{i\theta} = W_i^{\theta} / B^{\theta}$ are constant quantities on the flux surfaces respectively. In the large aspect ratio limit, Eq.(10) and Eq.(11) result in

$$W_{i\theta} = -\frac{\mu_{i1}}{\mu_{i2}} V_{i\theta}^{\text{nc}}, \quad (12)$$

$$V_{i\theta}^{\text{nc}} = k_i \frac{B_{\theta} B_{\zeta}}{e_i \langle B^2 \rangle} \frac{d\bar{T}_i}{d\psi}, \quad k_i = -\frac{\mu_{i2}}{\mu_{i1}}, \quad (13)$$

where $V_{i\theta}^{\text{nc}}$ is the ion neoclassical covariant poloidal flow.¹⁶

Substituting Eqs.(9) and (12) into Eq.(3), we obtain the poloidal damping force,

$$\nabla \cdot \overleftrightarrow{\Pi}_{\parallel} = m_i n_i \mu_{i1} \frac{\langle B^2 \rangle}{B_{\theta}^2} (V_{i\theta} - V_{i\theta}^{\text{nc}}) \mathbf{e}_{\theta}$$

$$= m_i n_i \mu_{\text{nc}} \mathbf{b}_0 \times \nabla \left[\frac{\bar{\phi}}{B_0} - \frac{k_{\text{nc}} \bar{P}_i}{e_i n_i B_0} \right] \quad (14)$$

$$\mu_{\text{nc}} = \mu_{i1} B_0^2 / B_p^2, \quad k_{\text{nc}} = k_i - 1, \quad (15)$$

where Eqs.(14) and (15) correspond exactly to Chôné's expressions⁴ in the large aspect ratio limit for $B_0^2 / B_p^2 \rightarrow q^2 / \epsilon^2$, where ϵ is the inverse aspect ratio and q is the safety factor respectively. Finally the contribution from the parallel viscous force to the vorticity equation becomes

$$\mathbf{b} \cdot \nabla \times \nabla \cdot \overleftrightarrow{\Pi}_{\parallel} = m_i n_i \mu_{\text{nc}} (\bar{U}_E - k_{\text{nc}} \bar{U}_D), \quad (16)$$

where $U_D = \nabla_{\perp}^2 (P_i / e_i n_i B_0)$ is the diamagnetic vorticity and the spatial structure of the damping coefficients μ_{nc} and k_{nc} have been neglected for simplicity.

3 Preliminary simulation results

In this section, we show preliminary simulation results of the 2-field L-H transition model by BOUT++_LH. In BOUT++_LH, Eq.(1) and Eq.(2) are normalized with respect to the characteristic

Table 1 Normalization parameters in BOUT++ LH

length	$L_N = L_{\text{mag}}$	3.76×10^0 [m]
magnetic field	$B_N = B_{\text{mag}}$	5.30×10^0 [T]
time	$t_N = t_A$	1.45×10^{-7} [s]
pressure	$P_N = B_N^2/2\mu_0$	1.12×10^7 [Pa]

Alfvén time $t_A = L_N/V_A$, major radius R_{mag} , magnetic field intensity B_{mag} , magnetic energy $B_{\text{mag}}^2/2\mu_0$. The normalized factors are summarized in Table 1, where $n_i = 1.0 \times 10^{19}[\text{m}^{-3}]$ has been employed in the calculation of the system Alfvén velocity $V_A = B_{\text{mag}}/\sqrt{\mu_0 n_i m_i}$.

The radial profiles of the energy source and sink are shown in Figure 1-(a) and the radial profiles of the poloidal damping coefficients are also shown in Figure 1-(b). In terms of the poloidal damping coefficients, we have employed the simplified profiles by reference to the typical profiles in the L-H transition. The viscosity, resistivity and diffusivity used are $\mu_{\perp} = \chi_{\perp} = \eta = 1.0 \times 10^{-6}$ and $\chi_{\parallel} = 1.0 \times 10^{-2}$.

Figure 2 shows the preliminary simulation results by BOUT++ LH. The RBM ($n = 12, m = 36$) grows linearly and is saturated at about $t = 800t_A$. In the nonlinear phase, the pedestal like pressure profile and the strongly sheared radial electric field are observed at the vicinity of the separatrix.

4 Summary

The derivation of the 2-field L-H transition model has been described with emphasis on the derivation of the poloidal damping term in section 2. The poloidal damping term has been derived from the Gianakon's closure of the parallel viscous force and both the mean radial and parallel ion force balance. We have also confirmed that our poloidal damping term reproduces the Chôné's expression in the large aspect ratio limit.

The preliminary simulation has been shown in section 3. Some typical characteristics of the L-H transition have been observed but we cannot argue that the L-H transition was observed due to the lack of turbulence analyses. The development of the turbulence analysis tools is under development.

Acknowledgement

The authors would like to thank Drs. X.Q. Xu and B.D. Dudson for useful discussions. This work has been partly supported by JSPS KAKENHI Grant Numbers 23246163 and 26889068. The simulations were carried out on the supercomputer system HELIOS at IFERC, Aomori, Japan, under the Broader

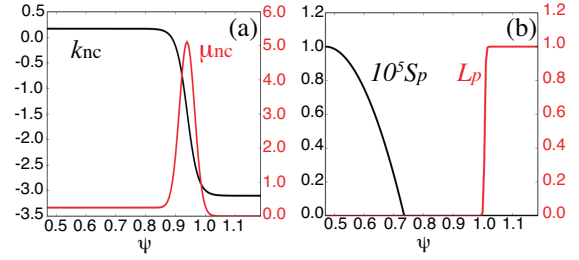


Fig. 1 (a): radial profiles of k_{nc} and μ_{nc} . (b): radial profiles of S_p and L_p .

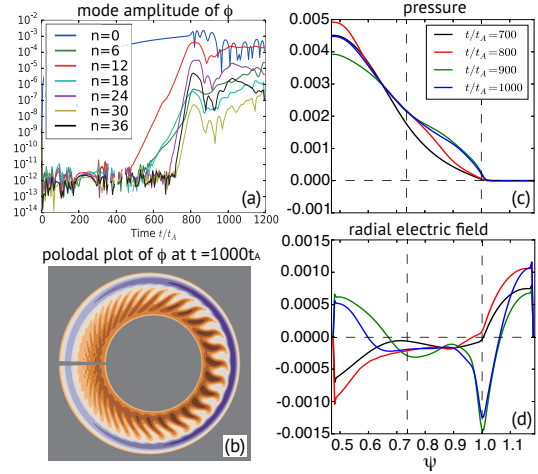


Fig. 2 (a): temporal evolution of the toroidal mode amplitude $|\phi_n|$ on the outer mid-plane, (b): poloidal plot of ϕ at $t = 1000t_A$, (c): temporal evolution of the FSA pressure, (d): temporal evolution of the FSA radial electric field

Approach collaboration between Euratom and Japan, implemented by Fusion for Energy and JAEA.

References

- [1] Wanger F. *et al.*, Phys Rev Lett **49**, 1408 (1982)
- [2] Itoh K. *et al.*, Plasma Phys Control Fusion **36**, 297 (1994)
- [3] Yagi M. *et al.*, Contrib Plasma Phys **52**, 372 (2012)
- [4] Chôné L. *et al.*, Phys Plasmas **21**, 070702 (2014)
- [5] Park G.Y. *et al.*, IAEA-FEC 2014, 2014, TH/8-1.
- [6] Dudson B.D. *et al.*, Comput Phys Comm **180**, 1467 (2009)
- [7] Dudson B.D. *et al.*, J Plasma Phys, FirstView, (2014)
- [8] Xu X.Q. *et al.*, Phys Rev Lett **105**, 175005 (2010)
- [9] Xia T.Y. *et al.*, Nucl Fusion **53**, 073009 (2013)
- [10] Yagi M. *et al.*, Phys Fluids B, **5**, 3702 (1993)
- [11] Hazeltine R.D. *et al.*, Phys Fluids **28**, 2466 (1985)
- [12] Gianakon T.A. *et al.*, Phys Plasmas, **9**, 536 (2002)
- [13] Hinton F.L. and Hazeltine R.D., Rev Mod Phys **48**, 239 (1976)
- [14] Hirshman S.P. and Sigmar D.J., Nucl Fusion **21**, 1079 (1981)
- [15] Callen J.D. *et al.*, Phys Plasmas **16**, 082504 (2009)
- [16] Helander P. and Sigmar D.J., Collisional Transport in Magnetized Plasmas, Cambridge University Press, (2002), see section 12.7

Isotope effect of hydrogen in tungsten

Kazuhito Ohsawa¹, Yuji Hatano², Masatake Yamaguchi³

¹Research Institute for Applied Mechanics, Kyushu University

²Hydrogen Isotope Research Center, University of Toyama

³Center for Computational Science and e-system, Japan Atomic Agency

1. Introduction

Tungsten (W) and its alloys are promising as plasma facing materials (PFMs) in fusion reactors due to the excellent properties, e.g. low hydrogen (H) solubility, high H diffusivity, and high melting point. Divertor armor tiles installed in fusion reactors are exposed to the most intense plasma particle irradiation. So, a large amount of H isotopes, deuterium (D) and tritium (T), are expected to be retained in the divertor armor tiles. In particular, tritium retention of the PFMs is very serious safety concerns because T is a radioisotope whose physical half-life is 12 years.

H isotopes are not soluble in the W bulk because of the very low natural solubility. Therefore, H isotopes are expected to be retained in the vacancy type lattice defects nucleated in the W species. In the present works, we investigate interaction of H isotopes with a W vacancy in terms of first-principle calculations. Stable structures of multiple H atoms in the W vacancy are very anomalous compared with those in usual bcc transition metals. A maximum of six H atoms are trapped in a vacancy in the transition metals, while twelve H atoms can be accommodated in a W vacancy.

We investigate super abundant vacancy (SAV) formation induced by hydrogen in an equilibrium thermodynamic model. Vacancy formation energy is remarkably reduced by the presence of hydrogen at finite temperature. We examine vacancy-hydrogen (V-H) cluster formation energy trapping k H atoms (VH_k) and dependence of the V-H cluster concentration on the temperature and bulk H concentration.

2. Methodology

First-principle calculations are performed using Vienna ab initio simulation package (VASP) based on density functional theory. Binding energy e_k of H or H isotopes to a W vacancy is defined, as follows.

$$e_k = E[\mathbf{W}_{n-1}\mathbf{V}] - E[\mathbf{W}_{n-1}\mathbf{VH}_k] - k(E[\mathbf{W}_n\mathbf{H}^T] - E[\mathbf{W}_n]) \quad (1)$$

where the function E is the cohesive energy of the supercell. $\mathbf{W}_{n-1}\mathbf{VH}_k$ indicates a supercell composed of $n-1$ W, a vacancy V, and k H atoms. \mathbf{H}^T means solute hydrogen in bulk W at T site. We use a large simulation cell, $6 \times 6 \times 6$ bcc lattice i.e. $n=432$ to calculate vibrational entropy, as mentioned later. V-H cluster concentrations are calculated in an equilibrium thermodynamic model.

Helmholtz free energy is

$$F = U - TS \quad (2)$$

The internal energy is expressed as

$$U = Ne_v - \sum_k n_k e_k, \quad (3)$$

where e_v is empty vacancy formation energy, n_k is the number of VH_k , and N is the total number of the V-H clusters. Entropy is composed of two terms, configurational and vibrational entropy.

$$S = S^{con} + S^{vib} \quad (4)$$

The configurational entropy is derived from Boltzmann equation.

$$S^{con} = k_B \ln \Omega, \quad (5)$$

where Ω is the number of possible arrangement of V-H clusters and solute H atoms distributed over the T site in bcc W lattice. The vibrational entropy is described in the lattice vibration ratio in high temperature approximation.

$$S^{vib} = k_B \sum_k n_k \ln P_k \quad P_k = \prod_i v_i / v'_{ki} \quad (6)$$

where v_i and v'_{ki} are vibration mode of perfect lattice and i -th atom in the vicinity of V-H cluster VH_k . We calculate zero point vibration energy of H atoms in order to examine isotope effects, as well. The number of V-H clusters n_k is determined by minimization of the free energy in Eq. (2).

3. Results

Figure 1 indicates binding energies of H isotopes e_k to a W vacancy in Eq. (1). The formation energy for an empty vacancy e_v is estimated to be 3.028 eV. We confirm that binding energy of lighter H isotopes is larger than that of heavier one.

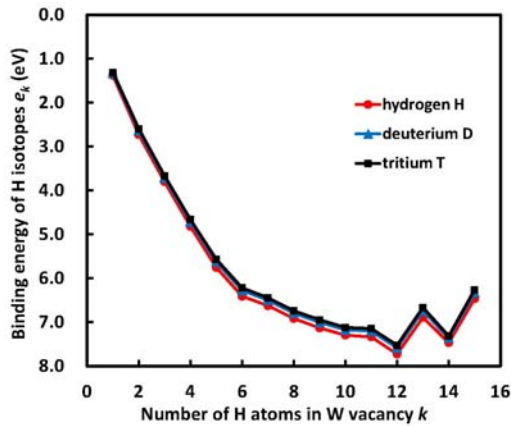


Fig. 1: Binding energy of H isotopes (H, D, T) to W vacancy.

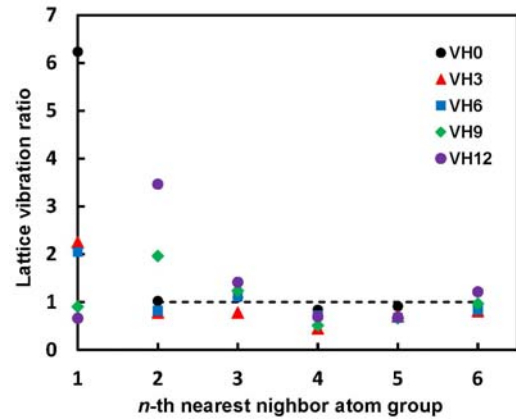


Fig. 2: Lattice vibration ratio of n -th nearest neighbor atom groups of V-H cluster VH_k .

Figure 2 indicates lattice vibration ratio of perfect and defected lattice defined in Eq. (6). In the case of bcc lattice, the numbers of atoms of first, second, and third nearest neighbor from a point defect are 8, 6, and 12, and so on. Figure 2 expresses the total product of lattice vibration ratio of each nearest neighbor atom group. The frequencies of W atoms far from a V-H cluster VH_k are assumed to converge to those of a perfect lattice. So, we take up to the fifth nearest neighbor atom group in the vibrational entropy calculation.

Concentrations of V-H cluster are calculated as a function of bulk H concentration and temperature, as shown in Fig. 3. In the limit of low H concentration, the vacancy concentration at a given temperature is usual thermal vacancy concentration. However, the V-H cluster concentrations rapidly increase when the bulk H concentration exceeds a threshold value. It is possible to be accommodated more than six H atoms in a W vacancy. However, the majority of V-H cluster is VH_6 in a wide range of temperature and bulk H concentration, as shown in Fig. 4.

4. Discussion

More than six H atoms can be accommodated in a W vacancy. However, the major V-H clusters are VH_6 in a wide range of given condition in the present thermodynamic model. We will explain why so many VH_6 clusters are nucleated. According to Fig. 1, the total binding energy is monotonically increases as the number of H atoms in the W vacancy. The binding energy increment is about 1.0 eV for an additional H until six H atoms are trapped. While, the increment is lowered to about 0.2 eV when more than six H atoms are trapped. Therefore, the VH_6 contributes to reduce the free energy.

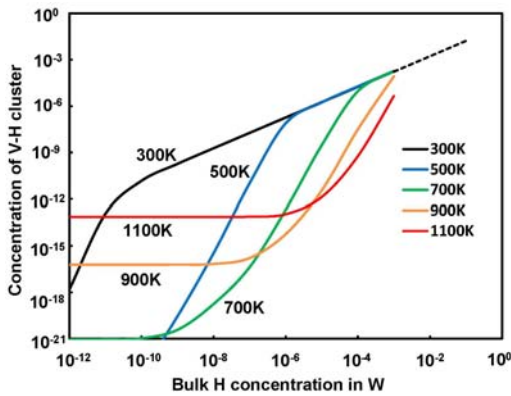


Fig. 3: Dependence of concentration of V-H cluster on bulk H concentration in finite temperatures.

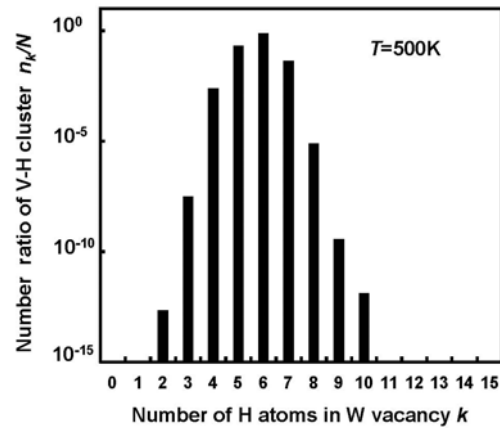


Fig. 4: Number ratio of V-H cluster VH_k at $T=500K$ and H concentration 10^{-3} .

References

K. Ohsawa, F. Nakamori, Y. Hatano, M. Yamaguchi, J. Nucl. Mat. **458** (2015) 187.

Analysis of Ion-Temperature-Gradient Instabilities by Using a Gyro - Fluid Model in Cylindrical Plasmas

G. Hattori, N. Kasuya^a, M. Yagi^b

Interdisciplinary Graduate School of Engineering Sciences, Kyushu University, 6-1 Kasuga-Koen, Kasuga, Fukuoka 816-8580, Japan

^a Research Institute for Applied Mechanics, Kyushu University, 6-1 Kasuga-Koen, Kasuga, Fukuoka 816-8580, Japan

^b Japan Atomic Energy Agency, 2-166 Omotedate, Obuchi, Rokkasho-mura, Aomori 039-3212, Japan

1. Introduction

Anomalous transport is the important issue in magnetic confined plasmas. Nonlinear couplings form turbulent structures, and competition of several kinds of instabilities determines the formed structure and the level of the turbulent transport [1]. One of the causes is an ion-temperature-gradient (ITG) driven microscopic instability (η_i mode) [2]. It is predicted to be unstable, when $\eta_i (= L_T^{-1}/L_n^{-1})$ is more than its threshold, where the inverse of the density gradient length and the ion temperature gradient length are $L_n^{-1} (= -d(\ln n_0)/dr)$ and $L_T^{-1} (= -d(\ln T_0)/dr)$, respectively.

In high-temperature plasma experiments, it is difficult to identify the ITG instability, because of the limitation of the diagnostics. In laboratory experiments using linear machines, detailed measurements of fluctuations are possible to identify the ITG instabilities [3]. In PANTA device, Numerical simulations for the linear growth rate of ITG modes have also been carried out by utilizing the fluid model in PANTA, which shows that the mode with $k_{\perp}\rho_s \sim O(1)$ is destabilization even with a low ion temperature [4]. It is necessary to include the finite-Larmor-radius (FLR) effect so as to perform more quantitative analysis. Our target is ITG instability in linear devices. The ion Larmor radius can be comparable to the plasma radius in linear devices, so we are developing a simulation code using the gyro-fluid model to include the FLR effect. By using the linearized model, the excitation condition of the ITG instability is evaluated.

2. Model Equations

A set of gyro-fluid equations is derived by taking the moments of the following nonlinear electrostatic gyro-kinetic equation in the velocity-spaces [5]. The target plasma has the cylindrical configuration with a homogeneous magnetic field parallel to the axial direction, so the magnetic curvature terms can be eliminated. Applying the gyro-kinetic ordering, the linear forms of the equations are given to be

$$\frac{dn}{dt} + \nabla_{\parallel} u_{\parallel} + \left(1 + \frac{\eta_{i\perp} \hat{V}_{\perp}^2}{2}\right) \frac{\rho_s}{L_n} \frac{\partial \Psi}{r \partial \theta} = 0, \quad (1) \quad \frac{du_{\parallel}}{dt} + \nabla_{\parallel} (n\tau_{\parallel} + T_{\parallel} + \Psi) = 0, \quad (2)$$

$$\frac{1}{\tau_{ii}} \frac{dT_{\parallel}}{dt} + \nabla_{\parallel} (2u_{\parallel} + q_{\parallel}) + \eta_{ii} \frac{\rho_s}{L_n} \frac{\partial \Psi}{r \partial \theta} = -\frac{2v_{ii}}{3\tau_{ii}} (T_{\parallel} - T_{\perp}), \quad (3) \quad \frac{1}{\tau_{\perp}} \frac{dT_{\perp}}{dt} + \nabla_{\parallel} q_{\perp} + \left[\frac{1}{2} \hat{V}_{\perp}^2 + \eta_{i\perp} (1 + \hat{V}_{\perp}^2)\right] \frac{\rho_s}{L_n} \frac{\partial \Psi}{r \partial \theta} = \frac{v_{ii}}{3\tau_{\perp}} (T_{\parallel} - T_{\perp}), \quad (4)$$

where n is the ion density, u is the ion velocity, Ψ is the gyro-averaging potential $\Psi \equiv \Gamma_0^{1/2} \Phi$, Φ is the electrostatic potential, $\tau = T/T_e$, T is the ion temperature, T_e is the electron temperature, q is the heat flux, v_{ii} is the collision frequency between the ions and ρ_s is the effective Larmor radius evaluated by the electron temperature. The subscripts \parallel and \perp represent the quantities in the parallel and perpendicular direction to the magnetic field, respectively. Padé and $\langle J_0 \rangle^2 = \Gamma_0$ approximation are applied, where $\Gamma_0^{1/2} = (1 + b\tau_{\perp}/2)^{-1}$, $b\tau_{\perp} = -\nabla_{\perp}^2 = k_r^2 + k_{\theta}^2$.

Collision is dominant in this system, and higher order moments give simplified forms of the heat flux as follow [6];

$$q_{\parallel} = -\frac{3}{v_{ii}\tau_{\perp}} \nabla_{\parallel} T_{\parallel}, \quad (5) \quad q_{\perp} = -\frac{1}{v_{ii}\tau_{\perp}} \nabla_{\parallel} T_{\perp}, \quad (6)$$

The quasi-neutrality relation is given to be

$$\Gamma_0 \left(n + \frac{1}{\tau_{\perp}} \frac{\nabla_{\perp}^2 T_{\perp}}{2} \right) - (1 - \Gamma_0) \frac{\Psi}{\tau_{\perp}} = \Psi, \quad (7)$$

Our gyro-fluid model consists of Eqs. (1) - (4) and (7). The finite-Larmor-radius effect is included in Ψ , \hat{V}_{\perp}^2 and ∇_{\perp}^2 terms, where

$$\frac{\hat{V}_{\perp}^2}{2} \Psi = -\frac{b\tau_{\perp}/2}{(1 + b\tau_{\perp}/2)} \Psi, \quad (8) \quad \hat{\nabla}_{\perp}^2 \Psi = \frac{b\tau_{\perp}/2(b\tau_{\perp}/2 - 1)}{(1 + b\tau_{\perp}/2)^2} \Psi, \quad (9)$$

The FLR effect breaks the Boltzmann relation between the density and the potential in this model.

3.Linear Growthrate Analysis

The local linear analyses are carried out to evaluate the excitation condition of the ITG instability. For the linearization, the differential operator d/dt , $\nabla_{||}$ and ∇_{\perp} are replaced to λ , ik_z and ik_{\perp} , where the real and imaginary part of λ are the growthrate and frequency, k_z and k_{\perp} are the wavenumber in the parallel and perpendicular direction, respectively. The axial mode number is assumed to be 1, which gives $k_z = 2\pi\rho_s/l$, where l is the device length. The radial and azimuthal wavenumber are assumed to be same, which give $k_{\perp}^2 = 2k_z^2 = 2(m\rho_s/r)^2$, where m is the poloidal mode number. For the linear analysis, experimental parameters in PANTA are used; $l = 4.0$ m, plasma radius $a = 7.0$ cm, density $n = 1.0 \times 10^{19} \text{ m}^{-3}$, $L_n = 7.0$ cm, magnetic field $B = 0.1$ T, $v_{ii} = 350 \text{ s}^{-1}$.

Here, the linear growthrate at $r = a/2$ are calculated. Firstly the excitation condition with different discharge gases is analyzed. Figure 1 shows the ion mass dependences of critical η_c of the modes with $m = 1-5$. The cases of helium, neon, and argon are plotted. The minimum values of η_c are nearly 1 in spite of the change of the ion mass number. This result suggests that there is no preferential gas for the ITG excitation. Mode numbers of most unstable modes are different with different discharge gasses (He: $m = 5$, Ne and Ar: $m = 2$), so the azimuthal mode structure can be different.

Next the dependency on the temperature and its gradient length is evaluated. Figure 2 shows the contour plot of the growthrate in the τ and η space, assuming $\eta_{||} = \eta_{\perp} = \eta$ and $\tau_{||} = \tau_{\perp} = \tau$. The critical value η_c for the ITG instability changes depending on the magnitude of τ . The minimum $\eta_c = 0.8$ is given with $\tau = 0.15$, and η_c increases as τ increases ($\eta_c = 0.98$, when $\tau = 1.0$). In the case with lower τ , the ITG mode is hard to be unstable. The cross in Fig. 2 indicates one of the experimental conditions in PANTA ($\tau = 0.1$, $\eta = 0.2$ with Argon discharge). It suggests that a higher temperature gradient is needed to observe the excitation of the ITG mode in PANTA.

Characteristic dependencies of the threshold value are evaluated next. Our model includes the FLR effect, which is represented by the magnitude of variable b , so the FLR effect is investigated by changing b . Figure 3 shows the contour plot of the growthrate in the b and η space. The critical η_c increases with larger b , so the FLR affects to stabilize the ITG mode. Notes that the PANTA parameter gives $b = 0.8$.

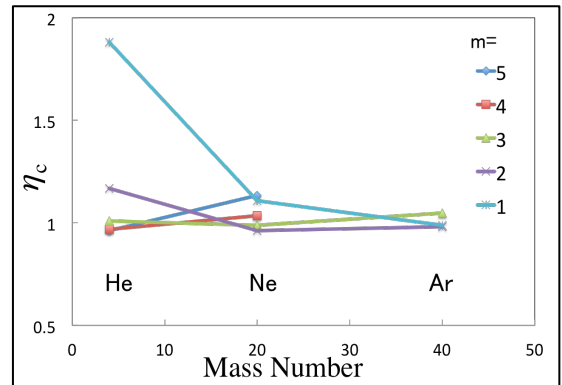


Fig.1 Ion mass dependences of critical η_c , when $\tau = 1$. Those of modes with $m = 1 - 5$ are shown.

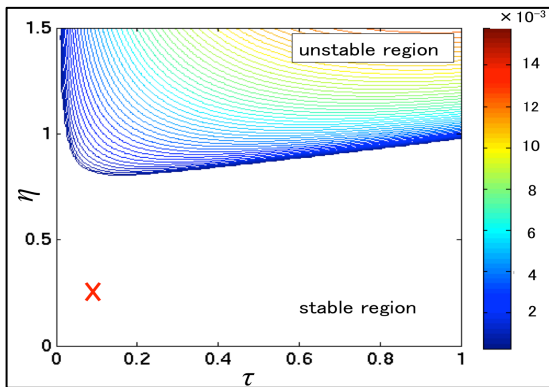


Fig.2 Contour plot of the growthrate in the τ and η space. The boundary for the ITG instability is shown. The cross represents one of the experimental conditions in PANTA.

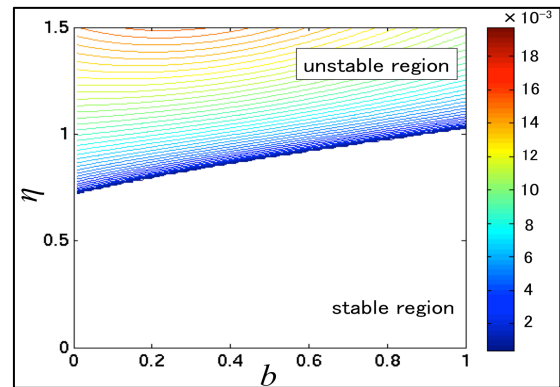


Fig.3 Contour plot of the growthrate in the b and η space. This is the case with $\tau = 1.0$ of Argon plasma.

4.Comparison of the Gyro-Fluid and Fluid Model

Here we use the gyro-fluid model for the ITG excitation condition in PANTA. On the other hand, the ITG analyses have been carried out previously by using the Hamaguchi-Horton (H-H) model, which consists of fluid equations [7]. The results from the H-H model show that the critical temperature gradient is smaller than that with the gyro-fluid model. Comparison between the two models is carried out in this section.

The H-H model solves three fields with ion continuity equation, momentum conservation equation and energy

conservation equation. For the comparison, a reduced set of the gyro-fluid model is obtained with isotropic temperature $T_{||} = T_{\perp} = T$ as

$$\frac{d}{dt} \left[1 - \left(1 + \frac{1}{\tau} \right) \nabla_{\perp}^2 \right] \phi + \nabla_{||} u_{||} + \frac{\rho_s}{L_n} \frac{\partial \phi}{r \partial \theta} + \frac{1}{2} \frac{\rho_s}{L_r} \frac{\partial}{r \partial \theta} (\nabla_{\perp}^2 \phi) = 0, \quad (10) \quad \frac{du_{||}}{dt} + \left[1 + \tau + b\tau \left(1 + \frac{1}{\tau} \right) \right] \nabla_{||} \phi + \left(1 + \frac{b\tau}{2} \right) \nabla_{||} T = 0, \quad (11)$$

$$\frac{dT}{dt} + \frac{2}{3} \tau \nabla_{||} u_{||} + \tau \frac{\rho_s}{L_r} \frac{\partial \phi}{r \partial \theta} = 0, \quad (12)$$

Here the heat-flux terms and the FLR terms in Eqs. (1)-(4) are neglected, and the FLR term with variable b is only retained in the quasi-neutrality relation. Equation (12) is obtained by adding Eqs. (3) and (4). The basic frameworks of the two sets of the models are similar, though some coefficients are different.

Figures 4 and 5 show the contour plots of the growthrate in the τ and η space with the H-H model and the reduced gyro-fluid model, respectively. Critical η_c is much smaller in the case with the H-H model than with the gyro-fluid model. In Fig. 4 the ITG mode is unstable even with $\eta = 0$, when τ is greater than 0.6. Figure 5 shows the same level of critical η_c even with the reduced set as Fig. 1, though the dependency on τ becomes weaker.

The different results come from different origins of the ∇_{\perp} term in each model, i.e., the polarization velocity term in the H-H model, and the gyro-averaging in the gyro-fluid model. In the H-H model the polarization term can couple with the diamagnetic drift term, which is not included in the gyro-fluid model.

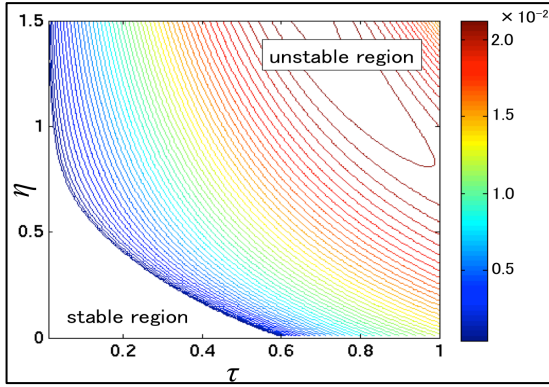


Fig.4 Contour plot of the growthrate in the τ and η space with the H-H model. This is the case of Argon plasma.

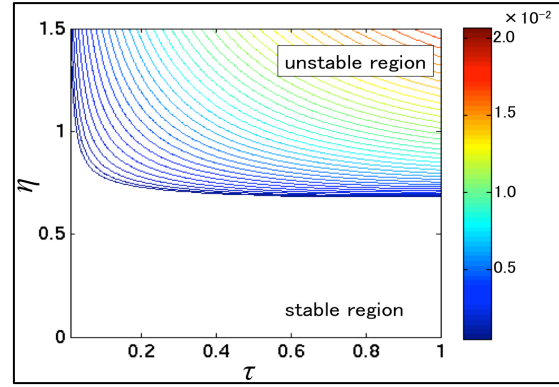


Fig.5 Contour plot of the growthrate in the τ and η space with the reduced gyro-fluid model. This is the case of Argon plasma.

5.Summary

The excitation condition for ITG instability in linear device PANTA is investigated by using the gyro-fluid model. Linear stability analyses show the dependencies of the linear growthrate on the ion mass, the temperature gradient, the magnitude of the FLR effect. Although the modenummer of the most unstable mode is different with different discharge gases, their critical values have almost the same level $\eta \sim 1.0$. There is difference between the results from the gyro-fluid model and the H-H model. The reason for the gap comes from the origin of the ∇_{\perp} terms. From the gyro-fluid model, more than 4 times larger η is needed to observe the ITG instability in PANTA.

Acknowledgements

Authors acknowledge discussions with Prof. S. Inagaki, Dr. M. Sasaki, Dr. Y. Kosuga and Mr. Y. Miwa. This work is supported by the Grant-in-Aid for Young Scientists (24760703), for Scientific Research (23244113) of JSPS, by the collaboration program of NIFS (NIFS13KNST050, NIFS13KOCT001) and of RIAM of Kyushu University.

Reference

- [1] P. H. Diamond, *et al.*, Plasma Phys. Control. Fusion **47**, R35 (2005).
- [2] W. Horton, Rev. Mod. Phys. **71**, 735(1999).
- [3] A. K. Sen, *et al.*, Phys. Rev. Lett. **66**, 429 (1991).
- [4] Y. Miwa, *et al.*, Plasma Fusion Res. **8**, 2403133 (2013).
- [5] W. Dorland and G. W. Hammett. Phys. Fluids B **5**, 812 (1993).
- [6] P. Snyder, Ph. D. thesis, Princeton Univ. (1999).
- [7] S.Hamaguchi and W.Horton, Phys. Fluids B **2**, 1833 (1990)

Simulation on Tungsten Transport and Sawtooth Control in Tokamak Plasmas with TOTAL Code

T. Fujita, Y. Shimizu, H. Natsume

Graduate School of Engineering, Nagoya University
Furo-cho, Chikusa-ku, Nagoya 464-8603, Japan

The PHZ and E_r pinch models have been introduced into TOTAL for high Z impurity transport study. Enhancement of tungsten accumulation by the counter toroidal rotation was found in the analysis of JT-60U H-mode plasma using PHZ. The Porcelli model has been introduced into TOTAL for study on effect of α particle pressure and local current drive on the sawtooth period. The sawtooth period has maximum as a function of α particle pressure, because of competitive stabilizing/destabilizing effects. The sawtooth periods are shortened by lowering magnetic shear at the $q = 1$ radius with local current drive.

1. Introduction

The TOTAL (toroidal transport analysis linkage) is an integrated code solving 1-D transport with 2-D tokamak equilibrium. Models on high-Z impurity transport and on sawtooth have been recently introduced. In this paper, analysis of tungsten transport in JT-60U H-mode plasmas and simulation of sawtooth period control by local current drive in ITER are presented.

2. Tungsten transport

Accumulation of tungsten (W) in the central region of core plasma is concerned because of its large radiation loss due to its high atomic number (high Z). It was observed that accumulation of tungsten is enhanced with increase in the counter toroidal rotation in JT-60U H-mode plasmas [1]. This phenomenon cannot be simply explained by the conventional neoclassical transport.

From theoretical considerations, two pinch models (PHZ pinch and E_r pinch) for high Z impurity due to the toroidal rotation and the radial electric field were proposed [2]. PHZ pinch is caused by change in the ion charge state along its drift orbit. E_r pinch is caused by change in the drift orbit due to the radial electric field. These two pinch models have been introduced into TOTAL and the results of the JT-60 experiments were simulated.

The impurity ion flux is given by following equations in TOTAL;

$$\Gamma_k = \Gamma_k^{NC} - D_k^{AN} \frac{\partial n_k}{\partial \rho} + V_k^{AN} n_k$$

$$\Gamma_k^{NC} = -D_k^{NC} \frac{\partial n_k}{\partial \rho} + V_k^{NC} n_k$$

where Γ_k is flux of impurity ions in charge state k. The NC and AN represent the neoclassical transport

and the anomalous transport, respectively. The neoclassical radial velocity V_k^{NC} and diffusion coefficient D_k^{NC} are calculated by NCLASS module in TOTAL. The anomalous diffusion coefficient D_k^{AN} is assumed to be uniform. The PHZ pinch and the E_r pinch are introduced in the V_k^{AN} term.

In the simulation, transport of tungsten ions were calculated with fixed density, temperature, toroidal rotation velocity and the radial electric field profiles and fixed MHD equilibrium. The radial profiles used for the simulation are shown in Fig. 1. These were obtained from the experimental data of 5 cases. The plasma parameters are the following: $R_p = 3.35$ m, $a = 0.85$ m, $B_t = 3.5$ T, $I_p = 1.6$ MA, $\kappa = 1.46$, $\delta = 0.32$, the neutral beam (NB) heating power is 15 MW. The toroidal rotation velocity V_t

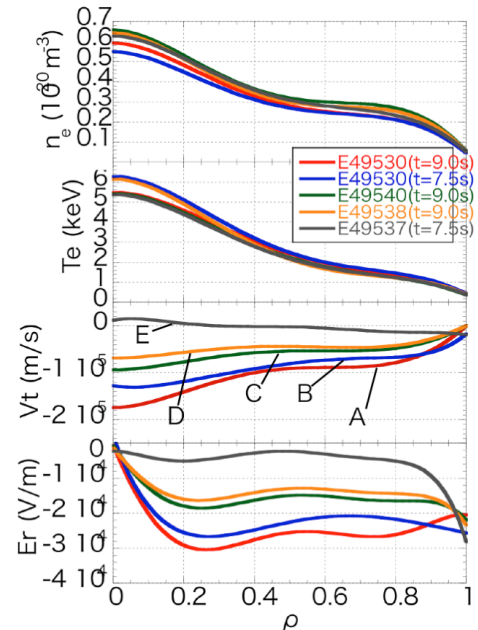


Fig. 1. Radial profiles of plasma parameters of the experimental data used for the simulation.

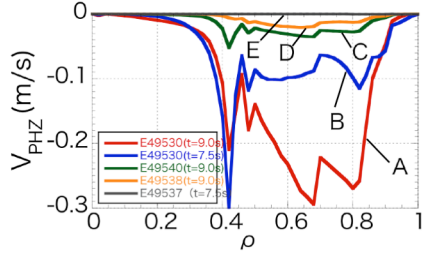


Fig. 2. Radial profiles of PHZ pinch velocity for tungsten ions.

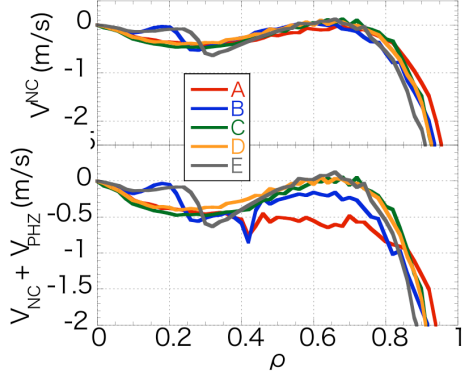


Fig. 3. Radial profiles of (top) neoclassical pinch velocity and (bottom) the total pinch velocity for tungsten ions.

was changed by varying a combination of the tangential NB injection at the constant NB power. The radial electric field E_r was calculated with integrated transport code TOPICS.

Figure 2 shows the radial profiles of PHZ pinch velocity [3]. The V_{PHZ} was larger in the inward direction for larger counter toroidal rotation. For all cases, the E_r pinch model was not applicable over the entire plasma volume. So we study only the effect of PHZ pinch setting $V_{Er} = 0$. Figure 3 shows neoclassical radial velocity and total radial velocity [3]. Magnitude of V_{PHZ} was similar to that of V_{NC} in $\rho < 0.8$. Difference in V_{NC} is recognized at $\rho \sim 0.2$ among 5 cases; nearly zero in case B and E.

The W ion transport was solved assuming the same W influx for 5 cases. Figure 4 shows the radial profile of W ion concentration $c_w = n_w/n_e$ for $D^{AN} = 0.01 \text{ m}^2/\text{s}$ [3]. This value of D^{AN} is similar to $D^{NC} = 0.008\text{-}0.012 \text{ m}^2/\text{s}$. The W ions accumulate at the center. The value of tungsten influx was determined so that the central c_w agrees with the experimental observation for case E (the smallest rotation). Figure 5 shows the dependence of central c_w on the toroidal rotation velocity [3]. In the high rotation case, the W accumulation is about four to five times as large as in the low rotation case. Dependence of W accumulation on the plasma

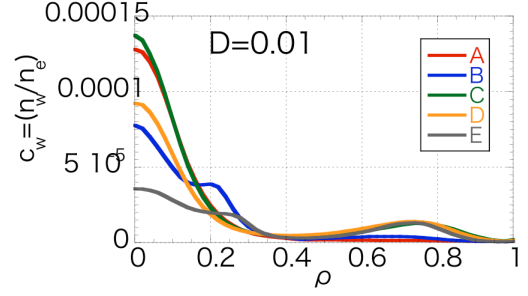


Fig. 4. Radial profiles of tungsten ion concentration (the density normalized by the electron density).

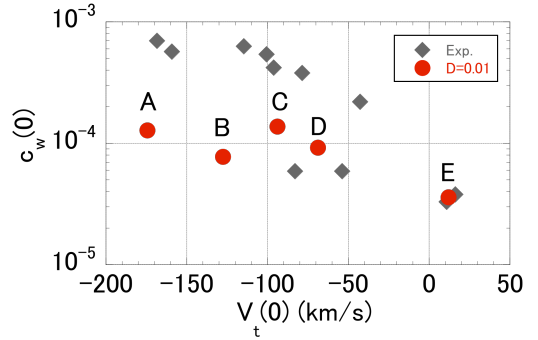


Fig. 5. Dependence of central tungsten accumulation on the central toroidal rotation velocity. Gray diamonds denote the experimental data while red circles denote the simulation results with $D^{AN} = 0.01 \text{ m}^2/\text{s}$.

rotation was seen, but was weaker than the experimental observation. W accumulation depends on D^{AN} ; larger $c_w(0)$ for smaller D^{AN} . The $c_w(0)$ for case A with $D^{AN} = 1 \times 10^{-4} \text{ m}^2/\text{s}$ is about 1.6 times as large as that with $D^{AN} = 1 \times 10^{-2} \text{ m}^2/\text{s}$.

3. Sawtooth control

The sawteeth with long periods eject large energy from the plasma center and also induce other instabilities such as NTMs. The Porcelli model [4] has been newly introduced into TOTAL, to study the effects of fast particles and magnetic shear on the sawtooth crash.

The sawtooth crash is triggered by the onset of the $m = 1$ mode (kink instability). Its stability condition is determined by the potential energy change δW ; the mode is unstable for $\delta W < 0$. In the Porcelli model, δW is represented by the sum of three terms, the ideal MHD term δW_{MHD} , the Kruskal-Oberman term δW_{KO} and the fast ion term δW_{fast} . In the model, the sawtooth crashes are triggered when one of the following conditions is satisfied,

$$-\delta\hat{W}_{\text{core}} = -(\delta\hat{W}_{\text{MHD}} + \delta\hat{W}_{\text{KO}}) > c_h \omega_{\text{Dh}} \tau_A \quad (1)$$

$$-\delta\hat{W} = -(\delta\hat{W}_{\text{core}} + \delta\hat{W}_{\text{fast}}) > 0.5 \omega_{*i} \tau_A \quad (2)$$

$$-c_\rho \hat{\rho} < -\delta\hat{W} < 0.5 \omega_{*i} \tau_A \quad \text{and} \quad \omega_{*i} < c_* \gamma_\rho \quad (3)$$

Here, $\delta\hat{W}$ etc. is the normalized potential energy change such that the growth rate is given by $-\delta\hat{W}/\tau_A$ (τ_A is the Alfvén time). See ref. [4] for finding definition of other variables. The condition (1) means that the fast ion stabilization doesn't work within a time scale of mode growth. The condition (2) means that the driving force overcomes the diamagnetic rotation stabilization of thermal ions. The condition (3) means that the resistive internal kink mode is driven for δW close to zero. The δW_{MHD} , δW_{KO} and δW_{KO} are evaluated by using analytic formula obtained for model equilibria. The q profile after crash is determined based on the Kadomtsev-type complete reconnection model. The density and temperature profiles are made flat inside the mixing radius.

The introduced model has been benchmarked with the Porcelli model module in the NTCC web site. Plasma parameters for the simulation were based on the ITER standard operation; $R_p = 6.2$ m, $a = 2.0$ m, $B_t = 5.3$ T, $I_p = 15$ MA, $\kappa = 1.7$, $\delta = 0.33$ and the line-averaged density was 1.0×10^{20} m⁻³. The density profile was assumed to be nearly flat and no particle transport was solved (the density profile was fixed). The heat transport was solved using the Bohm or the mixed Bohm /gyro-Bohm transport model. The edge temperature was fixed to 2 keV for both ions and electrons and no H-mode pedestal was considered. The heating power profile was assumed to be in proportional to $\exp[-(\rho/0.6)^2]$ where ρ is the normalized minor radius.

Figure 6 shows dependence of the sawtooth period τ_{saw} on the central ion temperature [5]. The

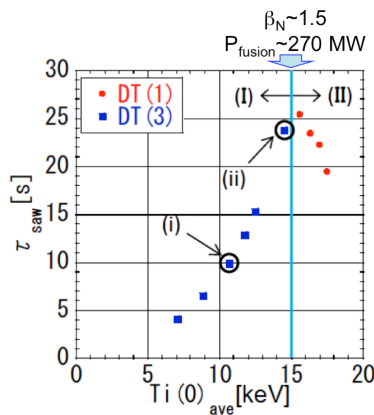


Fig. 6. Dependence of sawtooth period on the central ion temperature.

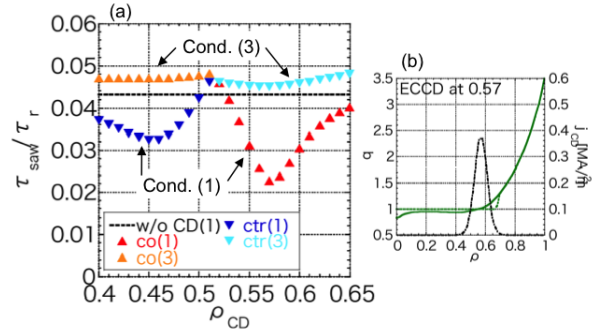


Fig. 7. (a) Dependence of sawtooth period normalized by the current diffusion time on the current drive location. (b) q profiles without CD (solid) and with CD at $\rho = 0.57$ (dotted) and driven current profile.

heating power was scanned to change the α particle pressure. The α particle pressure has a stabilizing effect through $-\delta W_{\text{fast}}$ and a destabilizing effect through $-\delta W_{\text{core}}$. In region (I), where sawteeth are triggered by condition (3), τ_{saw} increases with α particle pressure, due to its stabilizing effect. In region (II), where sawteeth are triggered by condition (1) (no effect of $-\delta W_{\text{fast}}$), τ_{saw} decreases with α particle pressure, due to its destabilizing effect.

Next, effect of magnetic shear control on τ_{saw} was studied by using a simple current drive (CD) model with fixed driven current and fixed location. The heating power required for CD was not taken into account. Figure 7(a) shows CD location dependence of τ_{saw} normalized by the current diffusion time τ_r in the $q = 1$ radius [6]. The plasma parameters were similar to those for Fig. 6 and $\beta_N \sim 1.6$. The driven current was 1 MA. The minimum τ_{saw}/τ_r was obtained by co-CD at $\rho = 0.57$. In this regime, the sawteeth are triggered by condition (1), where the sawteeth are destabilized by lowering magnetic shear at the $q = 1$ radius, s_1 , because δW_{MHD} and δW_{KO} are proportional to $1/s_1$. As shown in Fig. 7(b), s_1 was decreased effectively by local CD applied at $\rho = 0.57$.

References

- [1] T. Nakano, et al., J. Nucl. Mater. **415**, S327-S333 (2011).
- [2] K. Hoshino, et al., Nucl. Fusion **51**, 083027 (2011)
- [3] Y. Shimizu, et al., submitted to Plasma Fusion Res.
- [4] F. Porcelli, et al., Plasma Phys. Control. Fusion **38**, 2163 (1996).
- [5] H. Natsume, et al., Plasma Fusion Res. **9**, 3403048 (2014).
- [6] H. Natsume, et al., submitted to Plasma Fusion Res.

Toroidal rotation modeling with the 3D non-local drift-kinetic code and boundary models for JT-60U analyses and predictive simulations

M. Honda¹, S. Satake², Y. Suzuki², M. Yoshida¹, N. Hayashi¹, K. Kamiya¹, A. Matsuyama¹,
K. Shinohara¹, G. Matsunaga¹, T. Nakata¹, S. Ide¹ and H. Urano¹

¹ Naka Fusion Institute, Japan Atomic Energy Agency

² National Institute for Fusion Science

In present-day tokamaks, there are a variety of torque sources that impart toroidal rotation, like neutral beam injection (NBI) as the primary source. The “intrinsic torque” that is intrinsically generated without external momentum input is expected to be a major momentum source in ITER and a DEMO reactor, and its study is significantly important. As one of the possible intrinsic torque sources, much attention has been recently paid to the NTV (see e.g. [1]), which originates from the 3D non-axisymmetric magnetic field due to the imperfect toroidal symmetry of tokamaks. Enabling us to analyze the NTV in experiments and gain the predictive capability, we develop the cooperative framework among the TOPICS suite, the VMEC code and the FORTEC-3D code [2]. Here, TOPICS is the 1.5D integrated transport code and FORTEC-3D is the δf drift-kinetic solver developed originally for 3D devices, such as heliotrons and stellarators. VMEC computes a 3D equilibrium with plasma response based on the 2D free-boundary equilibrium computed by TOPICS plus the vacuum magnetic field produced by external coils. Coupling of the integrated code and the large-scale kinetic code allows us to accurately calculate the complicated NTV without assumptions on a magnetic equilibrium, guiding-center motion and the collision operator and so forth and to incorporate its effect into interpretive and predictive simulations. For rotation predictions over the entire profile, a boundary condition is as much important as the NTV, whereas a definitive boundary model for toroidal momentum has not been proposed yet. Focusing on the radial force balance equation between V_ϕ and E_r , an empirical boundary model for toroidal momentum is newly proposed with the aid of the SOL/divertor plasma code, D5PM.

JT-60U had the large TF ripple amplitude up to $\sim 2\%$ on the midplane. In the edge region counter-current V_ϕ was observed despite co-tangential NBI, but the radial current torque stemming from a ripple loss of beam ions was not sufficient to fill the rotation gap between simulations and experiments [3]. We thus consider that the NTV may play a role. The NTV calculations for the co, balance and counter NB injection cases are performed to examine how good including the NTV improves the reproducibility of toroidal rotation

profiles. Since the discharges in question are L-mode ones, the residual stress may be neglected. The momentum diffusivity is one of the major unknowns for toroidal momentum transport. We first estimate the ion heat diffusivity by the power balance analysis and then multiply the Prandtl number Pr with the heat diffusivity to obtain the momentum diffusivity. In JT-60U low β L-mode discharges, it has already been found that Pr varies within the range of about 0.5 to 1.1. We choose Pr within this range. Figure 1 illustrates the results, indicating that the NTV tends to decelerate the toroidal rotation velocities for all cases and this makes the prediction accuracy of the toroidal rotation profile better. The NTV is typically localized in the outer-core and edge regions and scales as the ripple amplitude increasing towards the edge. It is therefore important to include the NTV because the modification of rotation profiles in the edge region propagates inwards due to momentum pinch. Simulations show some evidence that the NTV is a major player in explaining the different sensitivity of the rotation profile to the ripple amplitude between co and counter rotation cases via E_r . This extensive research has brought better understanding of the NTV effects in JT-60U.

Despite the importance of the boundary condition (B.C.) for the toroidal momentum density $\langle \mathcal{L} \rangle$, the zero B.C. has been widely used because there are no boundary models yet. In JT-60U, it was observed that the E_r gradient at the plasma surface is independent of V_ϕ and virtually zero or negligibly small for many cases [5]. Using this empirical feature, we model the B.C. via E_r : $\langle \mathcal{L} \rangle$ is estimated by satisfying $d_\rho E_r = 0$ through the radial force balance equation. The pressure and temperature gradients are calculated using D5PM. Note that the applicability of the Matrix Inversion method, which is a neoclassical transport solver implemented in TOPICS, in the edge region adjacent to the separatrix has been verified against JT-60U data.

We are now capable of predicting toroidal rotation over the entire profile for a hydrogen L-mode plasma in ITER. The NTV produced by the static perturbed magnetic field stemming from the TF coils and the FSTs is taken into account. Co tangential NBs of 33MW are injected. Any profiles other than toroidal rotation are fixed, but the temperature profile is computed at initial to be consistent with D5PM predictions at the plasma surface. Predicted rotation at the magnetic axis is up to 2% of Alfvén speed, as shown in Fig. 2. Modeling the B.C. and the NTV enables us to perform rotation simulations over the entire profile, which can contribute to operation scenario development.

Acknowledgments

This work was supported by a Grant-in-Aid for Young Scientists (B) (No 25820442) from the Japan Society for the Promotion of Science (JSPS) and was carried out

using the HELIOS supercomputer system at International Fusion Energy Research Centre, Aomori, Japan, under the Broader Approach collaboration between Euratom and Japan, implemented by Fusion for Energy and JAEA.

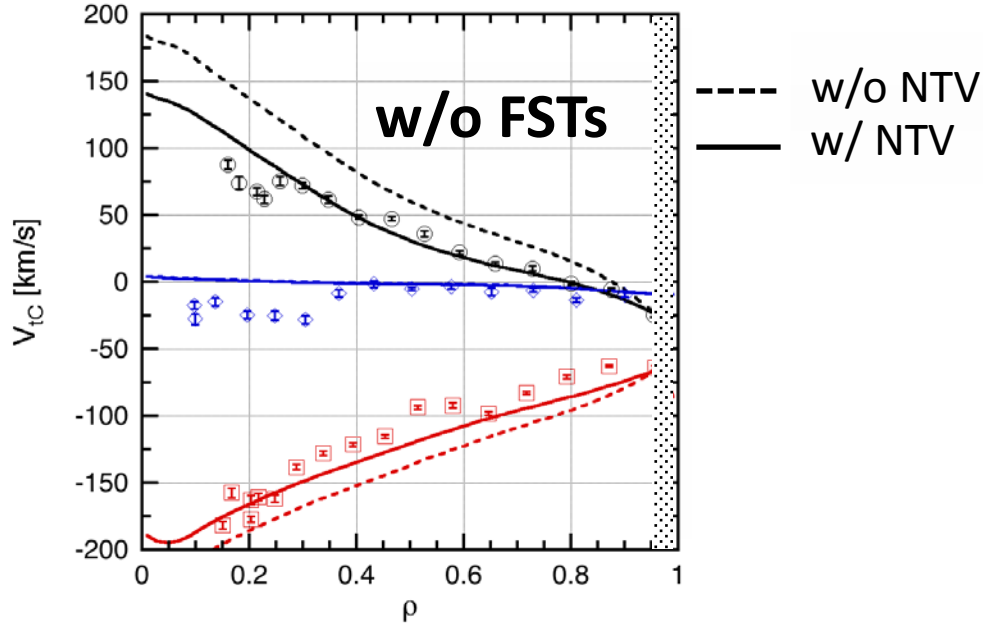


Figure 1. Measured $V_{c\phi}$ profiles and simulated ones with (solid lines) and without (broken) the NTV for the co (black), balance (blue) and counter (red) injection cases, respectively in JT-60U. The boundary is set at $\rho = 0.95$.

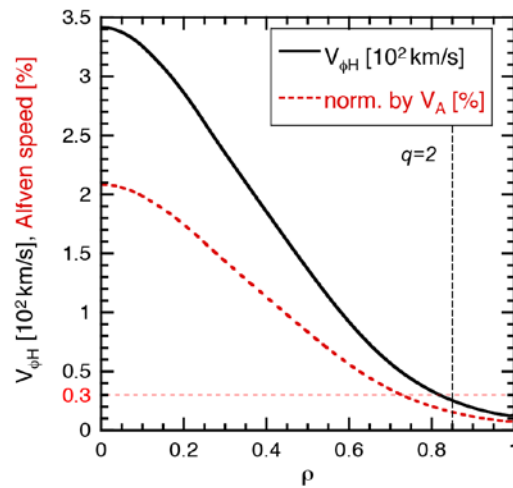


Figure 2. Predicted $V_{H\phi}$ profile in ITER. The red line indicates $V_{H\phi}$ normalized by the Alfvén speed.

References

- [1] K.C. Shaing, *Phys. Plasmas* **10** (2003) 1443.
- [2] M. Honda et al., *Nucl. Fusion* **54** (2014) 114005.
- [3] M. Honda et al., *Nucl. Fusion* **53** (2013) 073050.
- [4] S. Satake et al., *Nucl. Fusion* **53** (2013) 113033.
- [5] K. Kamiya et al. to be published in *Phys. Plasmas*.

Density peaking by parallel flow shear driven instability

Y. Kosuga^[1,2], S.-I. Itoh^[2,3], K. Itoh^[4,3]

[1] Institute for Advanced Study, Kyushu University, Fukuoka, Japan

[2] Research Institute for Applied Mechanics, Kyushu University, Fukuoka, Japan

[3] Research Center for Plasma Turbulence, Kyushu University, Fukuoka, Japan

[4] National Institute for Fusion Science, Gifu, Japan

Predictive modeling of turbulent transport is essential to the success of ITER and DEMO. An important feature of plasma turbulence is that plasma turbulence is characterized by co-existing multiple structures, such as zonal flows, axial flows, peaked density profile, etc. Interestingly, these structures can be driven by primary turbulence. In this sense, they are often called secondary structure. A well-known example of secondary structure is zonal flow, which is generated from Reynolds stress exerted by drift wave turbulence. Once generated, zonal flows feedback the underlying turbulence and reduce turbulent transport. More recently, it is observed that flows along the magnetic field (parallel flows) are also generated by drift wave turbulence, both in toroidal and linear devices. Interestingly, flows themselves can be a free energy source for turbulence, when the shear exceeds the critical value. In this case, flow shear drives primary turbulence, and the secondary structure in density can be established. Thus, turbulent plasmas are characterized by interacting primary turbulence and secondary structures, and their feedback is essential to understand the dynamics of turbulent plasmas. Understanding the coupling among turbulence and secondary structure is important for predictive modeling of turbulent transport.

A more specific example of the interplay of turbulence and secondary structure is reported from the recent experiment on a linear device, PANTA[1]. In that experiment, profile and transport flux are simultaneously measured by using the Mach probe. The measurement reveals that: i.) ∇n driven drift wave turbulence can exert Reynolds stress to drive parallel flows. The turbulence driven flows can invert the direction of externally driven flows by the source. ii.) when parallel flow shear becomes strong enough, turbulence then exerts Reynolds stress to relax the flow shear. In this case, particle flux can be inward, i.e. up the gradient, to drive peaked density profile. The first observation is the analogue of intrinsic toroidal rotation observed in toroidal devices, where drift wave turbulence with the broken symmetry exerts residual stress to drive flows. In this case, turbulence is primarily driven by density gradient, and the primary ∇n driven drift wave turbulence drives secondary structure of the parallel flow v_z . The second observation suggests that in this case the primary turbulence is driven by ∇v_z , and the primary ∇v_z driven turbulence drives the secondary structure in density profile.

From theoretical perspective, ∇v_z driven instability is analyzed by D'Angelo[2]. In that work, D'Angelo formulated the ∇v_z driven instability as a class of reactive instability, that can be thought of due to negative compressibility for ion acoustic waves. D'Angelo modes are stabilized by coupling to drift waves. Critical shear required for the onset of the instability was derived. Since then, the original work has been extended to include kinetic effect, the coupling of ion temperature gradient, etc[2]. However, these works focus on the nature of the instability, and do not address their impact on transport. In particular,

how the parallel flow shear driven turbulence couple to particle transport has not been addressed before.

In this work, we report the impact of D'Angelo modes on driving particle transport. From more broader perspective, the coupled dynamics of drift waves and D'Angelo modes is analyzed by calculating the energetics of turbulent fluctuation:

$$\partial_t I = \int d^3x (\mathcal{P} - \mathcal{D}), \quad (1a)$$

$$\mathcal{P} = c_s \rho_s \partial_y \frac{e\tilde{\phi}}{T_e} \frac{\tilde{n}_e}{n_0} \frac{\partial_x \langle n_e \rangle}{n_0} + c_s \rho_s \partial_y \frac{e\tilde{\phi}}{T_e} \frac{\tilde{v}_{\parallel}}{c_s} \frac{\partial_x \langle v_z \rangle}{c_s}, \quad (1b)$$

$$\mathcal{D} = D_{\parallel} \left\{ \nabla_{\parallel} \left(\frac{\tilde{n}_e}{n_0} - \frac{e\tilde{\phi}}{T_e} \right) \right\}^2. \quad (1c)$$

Here, $I \equiv \int d^3x \{(\rho_s \nabla_{\perp} e\tilde{\phi}/T_e)^2 + (\tilde{n}_e/n_0)^2 + (\tilde{v}_{\parallel}/c_s)^2\}/2$ is the turbulence intensity, \mathcal{D} is the collisional dissipation, \mathcal{P} is the production term for turbulent fluctuation. Other quantities follow the standard notation, i.e. c_s is the ion sound speed, etc. The production term takes the form of flux times gradient. By calculating the production term, we can identify the direction of energy flow (Fig.1). $\mathcal{P} > 0$ indicates that profile acts as a source of free energy to drive turbulence. On the other hand, $\mathcal{P} < 0$ implies that turbulence drives secondary structure. For example, if drift waves are dominant fluctuation, $\mathcal{P}_{DW, \nabla n} > 0$, thus density profile drives turbulent fluctuation. We find that $\mathcal{P}_{DW, \nabla v_z} < 0$ can be satisfied when $\overline{k_y k_{\parallel}} \neq 0$ where $\overline{(\dots)}$ denotes spectrum average. In this case drift wave turbulence can drive secondary parallel flows.

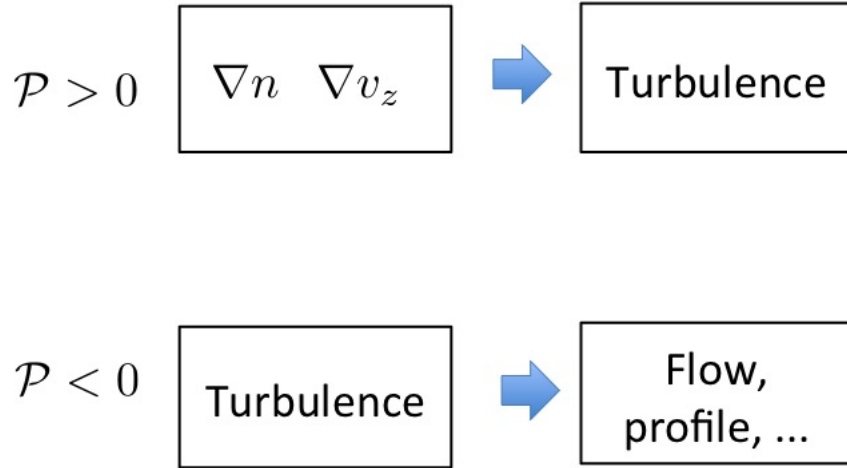


Figure 1: Turbulence production and the direction of energy flow.

When D'Angelo modes are dominant in turbulence, we find that $\mathcal{P}_{D'Angelo, \nabla v_z} > 0$. Thus the parallel flow shear acts as a free energy source to drive primary turbulence. $\mathcal{P}_{D'Angelo, \nabla n} < 0$ holds, when the parallel flow shear is the dominant contribution in $\mathcal{P}_{D'Angelo, \nabla n}$. In this case $\mathcal{P}_{D'Angelo, \nabla n} < 0$ is guaranteed by the necessary condition for D'Angelo modes to be unstable, $k_y k_z \langle v'_z \rangle > 0$. From this analysis, we can see that the secondary structure in density profile can be established. Interestingly, the corresponding particle flux is given as $\Gamma_n \propto -k_y k_z \langle v'_z \rangle$. Thus when D'Angelo modes are strongly unstable, they tend to drive inward particle flux. The inward particle flux can accumulate particles in the central region to establish the secondary peaked profile structure in density.

From the analysis given above, we find that peaked density profile can result when parallel flow shear becomes strong enough. As a caveat, the analysis presented here is oversimplified to focus on the effect of parallel flow shear on particle transport. More realistic analysis would require the coupling of perpendicular flow shear on transport, dynamic effect, atomic physics effect such as recombination and/or ionization. These effect will be studied in future.

We acknowledge useful discussion with S. Inagaki, T. Kobayashi, P.H. Diamond, and T. Takizuka. This work was supported by Grants-in-Aid for Scientific Research of JSPF of Japan (23244113, 25887041), Kyushu University Interdisciplinary Programs in Education and Projects in Research Development.

References: [1] T. Kobayashi, *Parallel flow structure formation by turbulent momentum transport in linear magnetized plasmas*, The 4th Asia Pacific Transport Working Group International Conference, BO2, (2014) [2] Nicola D'Angelo, *Phys. Fluids* **8**, 1748 (1965) [3] Valery V. Garvrishchaka, Supriya B. Ganguli, and Gurudas I. Ganguli, *Phys. Rev. Lett.* **80**, 728 (1998)

Progress on Disruption Research by Integrated Simulation

M. Yagi, A. Matsuyama, H. Nuga, N. Aiba and A. Fukuyama

Japan Atomic Energy Agency, Rokkasho, Aomori

1. Introduction

Up to present, 2D axisymmetric modeling of disruptions has widely been used, which is powerful tools for the parametric study to interpret the experiments and to predict the disruption mitigation scenarios. However, the necessity of improved modeling taking into account 3D nature of disruptions has recently been recognized. If one focuses on the wall load, the toroidal asymmetry of the energy deposition on the plasma facing components is often observed. Asymmetric vertical displacement events (VDEs), which accompanies a kink mode, may also cause a severe constraint on the supporting structures of the vessel wall. Concerning REs, enhanced RE losses have been observed with the excitation of magnetic fluctuations, typically being $n = 1$ mode (n : toroidal mode number), which results in toroidally localized wall loads in the RE discharge termination phase. The physics of these asymmetric loads has not yet been elucidated. Therefore, it is important to address the disruption physics (heat load, VDEs and REs) with a particular emphasis placed on its 3D nature. For this purpose, both hybrid and integrated simulations need to be developed. This report summarizes our recent study on the runaway electron simulations.

2. Redistribution of REs by Internal Modes

Runaway electrons (REs) produced during major disruptions can gain the energies above 10 MeV and their localized wall loads may unacceptably shorten the lifetime of plasma facing components. In ITER, even a small seed current can be amplified by an avalanche mechanism, and the formation of multi-MA RE beams poses a serious problem. Therefore, the development of mitigation schemes has become one of the most important topics in ITER.

The MHD modes that arise in the early phase of a current quench have been considered to mitigate the RE generation [1]. Because REs are produced predominantly in the core region near the magnetic axis, the main contribution is expected to be due to internal modes. For such modes to be effective for the RE de-confinement, the saturated island widths are a key parameter because REs are redistributed at a large parallel velocity along the stochastic magnetic fields once magnetic islands at different radial locations are overlapped. For treating such a phenomenon, we integrate a nonlinear reduced MHD code Extreme [2] (based on the

spectral method in the poloidal and toroidal directions) with a guiding-center runaway electron code ETC-Rel [3,4]. In the simulation, a resistive kink mode is considered as an example of the instability that causes the RE redistribution in the core region. Here, an initial MHD equilibrium with the peaked current profile ($q(0) \sim 0.6$) is chosen for the resistive kink to be unstable. The simulation has shown that REs immediately respond to the change of magnetic field topology associated with the kink growth, and the timescale of RE redistribution is dominated by the mode growth, independently of the RE energy. The physics involved is considered to be similar to the relaxation of fast-ion densities in the presence of sawteeth and fishbone.

Because REs are sensitive to the perturbing fields because of its small gyroradii, it is also expected that short-wavelength magnetic turbulence enhances the radial transport of REs. In future, an application of R4F [5], which can treat higher n modes on the basis of pseudo-spectral method, will be applied for such analyses.

3. RE Loss Flux Driven by External Modes

Another important contribution of MHD modes to REs is the RE current plateau termination driven by external modes. Although the stability properties of the RE current plateau have not yet been elucidated, the experimental correlation of prompt RE losses with the surface safety factor values are rather clear. It suggests the contribution of external-kink type modes. Following this idea, we develop a simulation model combining the linear stability code MARG2D [6] with ETC-Rel. Near the plasma edge, a strong kink perturbation causes a prompt loss of REs even in the absence of stochastic fields. For edge perturbations such as RMPs and external MHD modes, the energy dependence of RE losses are dominated by horizontal shift of the resonant position against the MHD modes due to the curvature drift motion. Because the loss pattern to the wall is governed by the radial magnetic field that is felt by particles [7] when they are lost from the boundary between closed and open field lines, the wall loads exhibit the $n = 1$ toroidal asymmetry.

4. Hot Tail Effect on RE Generation

The non-thermal effect should be taken into account for the RE generation mechanism. This is especially true when the thermal quench time is much shorter than the collision time. In such a situation, a high-energy part of bulk electrons does not have enough time to thermalize, which results in the formation of high-velocity tail of the electron velocity distribution. The existence of the high-energy tail enhances the primary RE generation rate, which is called as “hot-tail effect”. We have developed a Fokker-Planck simulation code TASK/FP in order to

calculate the time evolution of the relativistic momentum distribution function and that of induced toroidal electric field self-consistently [8]. In simulations using JT-60U like parameters, we found that the hot-tail effect becomes remarkable at thermal quench times below 0.25ms. The threshold value can be approximately interpreted as the electron-electron slowing down time. If the thermal quench time exceeds the slowing down time of almost all of electrons, the momentum distribution forms no tail, and the hot-tail effect is suppressed.

5. Summary and Future Work

Progress on the disruption research has been reported, focusing on the RE physics. As the next step, the simulation codes will be extended as an MHD+PIC hybrid model for studying the interaction between REs with MHD. Another important task is to treat slow plasma boundary evolution on the transport timescale, taking into account vertical displacement events (VDEs), which dominates a final loss position of REs. Finally, the mitigation method of disruptions such as Massive Gas Injection (MGI) [9] yields the short thermal quench time, which would enhance the hot-tail effect in ITER. It should be investigated as a future work.

Acknowledgments

The authors would like to thank Drs. T. Takizuka, A. Isayama, R. Hiwatari and Y. Ishii for useful comments. This work was supported in part by Grants-in-Aid for Scientific Research (23246163, 26820404, and 23561009). The computation was carried out using the HELIOS supercomputer system at IFERC-CSC.

References

- [1] P. Helander, et al, Plasma Phys. Control. Fusion 44 (2002) B247.
- [2] Y. Ishii, et al., Nucl. Fusion 43 (2003) 539.
- [3] S. Tokuda and R. Yoshino, Nucl. Fusion 39 (1999) 1123.
- [4] A. Matsuyama, et al., Nucl. Fusion (2014) 54 (2014) 123007.
- [5] M. Yagi, et al., Nucl. Fusion 45 (2005) 900.
- [6] N. Aiba, et al., Comput. Phys. Commun. 175 (2006) 269.
- [7] G. Papp, et al., Plasma Phys. Control. Fusion 54 (2012) 125008.
- [8] H. Nuga, et al., Plasma and Fusion Research, in press.
- [9] E. M. Hollmann, et al., Nucl. Fusion 53 (2013) 083004.

Progress of Integrated Modeling Code TASK

A. Fukuyama

Department of Nuclear Engineering, Kyoto University, Kyoto, Japan

The TASK code has been developed for integrated modeling of toroidal plasmas since 1992. It is composed of various components describing MHD equilibrium, transport, waves, instabilities and so on. The present structure is shown in Figure 1. In this presentations, recent progress in the development of full wave analyses in TASK.

Full wave analysis in TASK/WM and TASK/WF is to solve a boundary-value problem of Maxwell's equation to describe externally launched waves or internally excited instabilities:

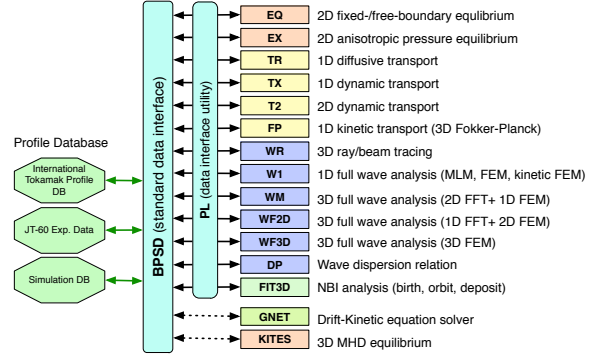


Figure 1 Present structure of the TASK code

$$[\nabla \times \nabla \times \mathbf{E} = \frac{\omega^2}{c^2} \overleftrightarrow{\epsilon} \cdot \mathbf{E} + i\omega\mu_0 \mathbf{j}_{\text{ext}} \quad (1)$$

where $\mathbf{E}(\mathbf{r}, \omega)$ is the wave electric field with angular frequency ω and $\overleftrightarrow{\epsilon}$ is the dielectric tensor representing the response of plasma. The merit of full wave analysis is that it can describe wave propagation with wave length longer than the scale length of the medium, wave penetration over an evanescent layer, coupling to realistic antenna, and formation of standing waves. There are three major numerical schemes for the full wave analysis: fast Fourier transform (FFT), finite difference method (FDM), and finite element method (FEM). The schemes presently used in the full wave components of TASK are summarized in Table 1.

Table 1 Numerical scheme in full wave analysis

component	system	scheme
WM	torus	toroidal & poloidal: FFT, radial: FDM
WMF	torus	toroidal & poloidal: FFT, radial: FEM
WF2D	torus	toroidal: FFT, poloidal and radial: FEM
WF3D	Cartesian	x, y, z : FEM

It has been recently recognized that, though FFT easily describes kinetic effects in hot plasmas, the description of short-wavelength waves in an inhomogeneous plasma requires very large computational resources because it causes coupling of all Fourier components and a large dense matrix equation has to be solved. On the other hand, since the coupling is localized in space in FDM and FEM, the matrix equation is sparse and tractable for parallel processing. FEM has a merit in flexibility of mesh compared with FDM. In

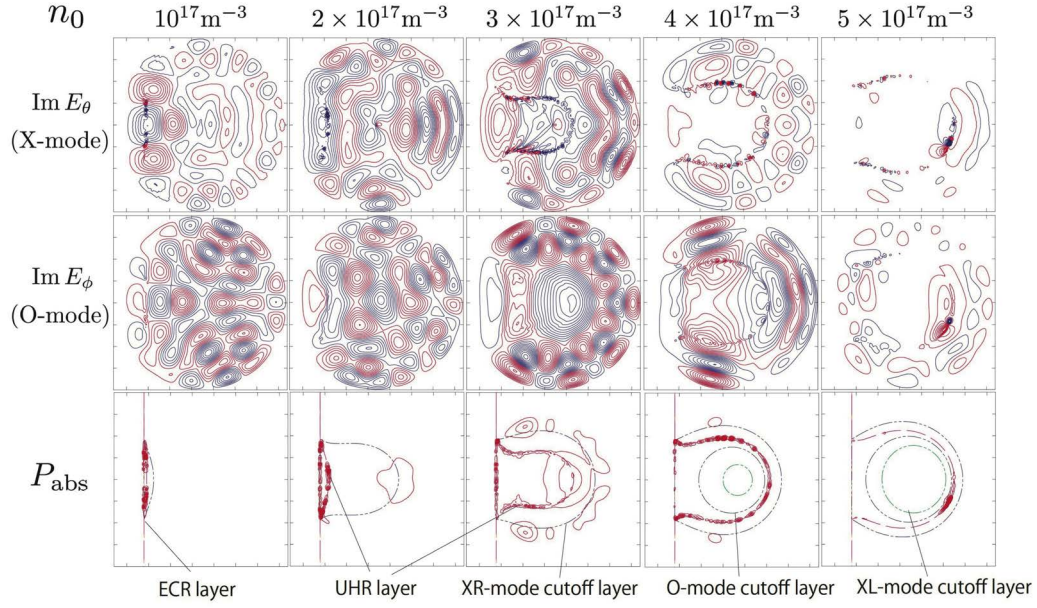


Figure 2 Density dependence of EC wave propagation and absorption

the three-dimensional (3D) version, WF3D, we use tetrahedron elements and the wave electric field is defined along an edge of a tetrahedron. In the two-dimensional (2D) version with axisymmetry, WF2D, triangular elements are used and the wave electric field is described by hybrid basis functions; the toroidal component is defined on a node and the poloidal and radial components on an edge of a triangle.

Using WF2D, we have carried out full wave analyses of electron cyclotron (EC) waves in a small-size spherical tokamak. For heating and current drive in high-density core plasmas of tokamaks, electromagnetic waves with EC range of frequencies have been extensively studied theoretically and experimentally. The propagation and absorption of EC waves are usually analyzed by the ray tracing method based on geometrical optics for waves with short wave length. In a plasma with high density or low magnetic field, however, the presence of cutoff layer may prevent the waves from penetrating into the central part from the low field side. In this case, the full wave analysis of EC waves is required for evaluating the absorption profile and optimizing the wave launching conditions. Figure 2 shows density dependence of propagation and absorption with $f = 5$ GHz and $B_0 = 0.072$ T.

The analysis in Fig. 2 employs dielectric tensor for a cold plasma with small amount of collision, $\nu/\omega = 0.003$. In the full wave analyses using FDM and FEM, it is necessary to describe kinetic effects without using wave number. For this purpose, we have developed an integral form of dielectric tensor in Maxwell's equation,

$$\nabla \times \nabla \times \mathbf{E}(\mathbf{r}, \omega) - \frac{\omega^2}{c^2} \int_V d\mathbf{r}' \overleftrightarrow{\epsilon}(\mathbf{r}, \mathbf{r}'; \omega) \cdot \mathbf{E}(\mathbf{r}', \omega) - i \omega \mu_0 \mathbf{J}_{\text{ext}}(\mathbf{r}, \omega) = \mathbf{0} \quad (2)$$

This form of dielectric tensor can be obtained by integrating along particle orbits and transforming velocity variables to spatial coordinates. There are two types of kernel functions in the kinetic dielectric tensor. One describes the Landau damping and the cyclotron

damping and is the Fourier transform of the plasma dispersion function. The other describes the finite gyroradius effects and is the Fourier transform of the modified Bessel functions.

The full wave analysis using the integral form of the dielectric tensor was applied to the one-dimensional (1D) modeling of the O-X-B mode conversion of EC waves in a tokamak configuration as shown in Fig. 3. The ordinary (O) mode excited at the low-field side propagates into the plasma, and is reflected at the cutoff. With an injection angle near the optimum, the O mode is converted to the extraordinary (X) mode which has also a cutoff near the O-mode cutoff. The converted X mode is reflected again near the upper-hybrid resonance and converted to the electron Bernstein (B) mode. The B mode is finally absorbed at the cyclotron resonance.

In summary, we are developing the integrated modeling code TASK. In order to analyze the propagation and absorption of short-wave-length waves in tokamak plasmas, full wave analysis using FEM has been developed. This scheme will indicate high performance for parallel processing. In order to include kinetic effects in the full wave analysis using FEM, integral formulation of the dielectric tensor has been developed. 1D full wave analysis using the integral formulation successfully described the propagation and absorption of the electron Bernstein waves.

Works in progress includes equilibrium with an isotropic pressure and rotation, multi-species version of 1D dynamic transport, parallelized version of full wave analysis of ion cyclotron and Alfvén eigenmodes, improvement of accuracy of full wave analysis using FFT, and 1D kinetic full wave analysis of O-X-B mode conversion.

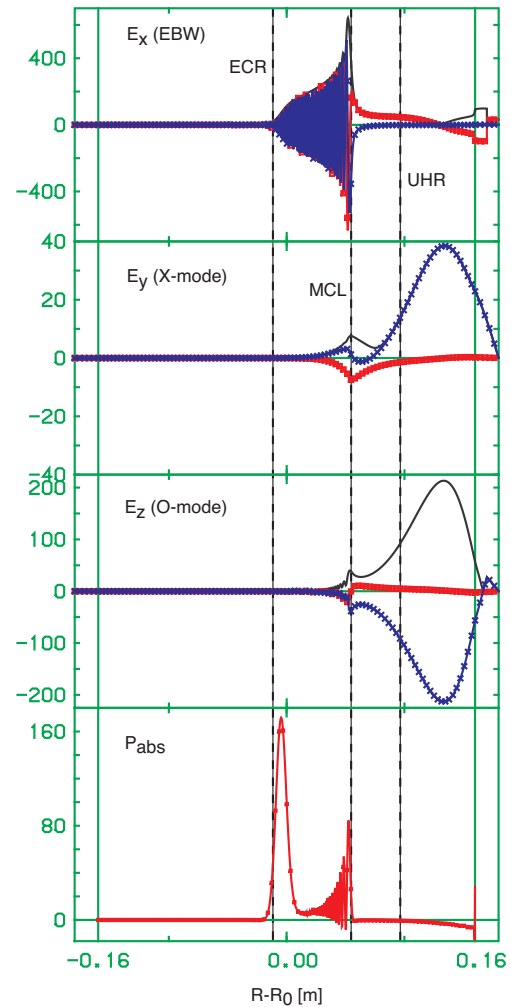


Figure 3 1D full wave analysis of O-X-B mode conversion of EC waves in a tokamak configuration

Statistical approach for predicting energy transport in LHD plasmas based on the TASK3D-a analyses database

M. Yokoyama^{1,2}

¹National Institute for Fusion Science, 322-6, Oroshi-cho, Toki-city, 509-5292, Japan

²Department of Fusion Science, The Graduate University for Advanced Studies, 322-6, Oroshi-cho, Toki-city, 509-5292, Japan

Recent development of the integrated transport analysis suite, TASK3D-a (analysis version for LHD experiment) [1], and its extensive application to a wide-ranging LHD plasmas have created the analysis-database including profile information such as of ion and electron temperatures (T_i and T_e), electron density (n_e), NBI heating deposition, and ion and electron heat diffusivities (χ_i and χ_e), etc. TASK3D-a, in brief, consists of modules for temperature/density profile fittings, VMEC [2] equilibrium specification, NBI deposition calculations [3] and steady-state/dynamic energy transport calculations, so that they are sequentially executed in an automated manner [1].

Conventionally, scaling laws for the global energy confinement time (τ_E) have been one of approaches to systematically grasp the energy confinement of fusion plasmas [4,5], and then also considered as one of guidelines to design/predict future devices. On the other hand, the physics-based transport models have been employed to predict the plasma performance such as expected temperature profiles for certain plasma operation scenario. In such predictions, it has been always problematic whether employed transport model(s) are actually responsible for governing energy confinement in plasmas to be forecasted, in other words, how to validate them.

Here, in this proceeding, let me propose an innovative consideration based on a statistical approach, to overcome such difficulties.

Accumulation of TASK3D-a analyses results has led to the attempt at deducing functional fittings for χ_e and χ_i with local parameters. Such deduced fitting expressions for heat diffusivities can be directly implemented into the predictive modelling, so that the transport model assumption (like a Gyro-Bohm) is no longer required. This approach may be considered to be the most relevant (“validated”) to the existing experiment database, because it is based on experimental data. Below, only a tiny part of the analysis-database (high- T_i plasmas) is utilized to describe an approach which is meant to be proposed.

Figure 1 shows radial profiles of fitted values of (a) T_i , (b) T_e and (c) n_e for analysed high- T_i plasmas [6]. The number of discharges considered here is 31. Multiple timings are analyzed in each discharge (corresponding to the timing of T_i -profile measurement, leading to about 200 timings), so that the evolution of T_i at core region from low- T_i to high- T_i phase can be tracked, not only at the timing with the highest values of T_i . The T_e profile is rather stiff compared to that of T_i in this database. The n_e profiles are flat to hollow. Figure 2 shows (a) χ_i and (b) χ_e , obtained from the dynamic transport analysis [7] which takes into account the NBI slowing down and temporal change of plasma parameters. The total number of data points (either ion or electron) shown in Figure 2 is around 3000.

On performing statistical analysis for TASK3D-a analysis-database, χ_i and χ_e are dimensionally normalized by Bohm diffusion coefficients, $T_{i,e}/(eB)$. Candidate predictive variables are also made into dimensionless, such as, for ions, the collision frequency normalized by that of plateau_Pfirsch-Schlüter boundary (ν_i^*), normalized Larmor radius (ρ_i^*) and the

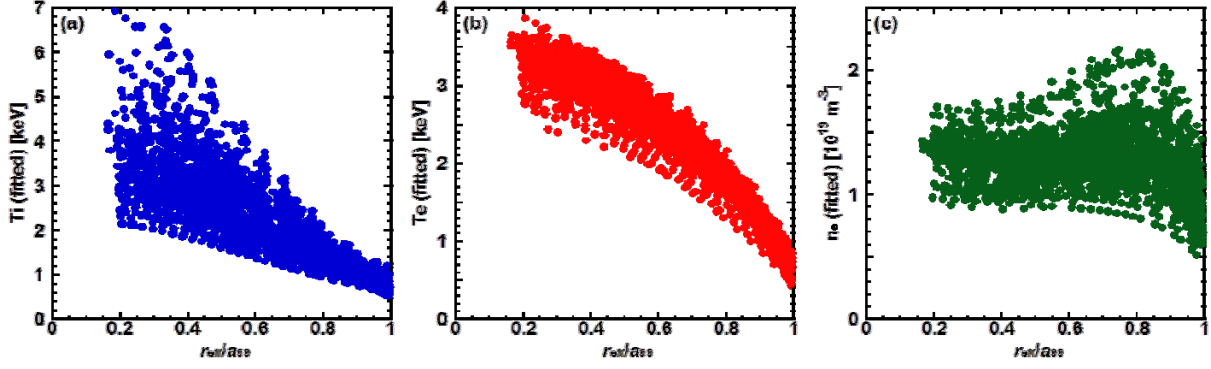


FIG. 1. Radial profiles (fitted) of (a) T_i , (b) T_e , and (c) n_e for analyzed cases.

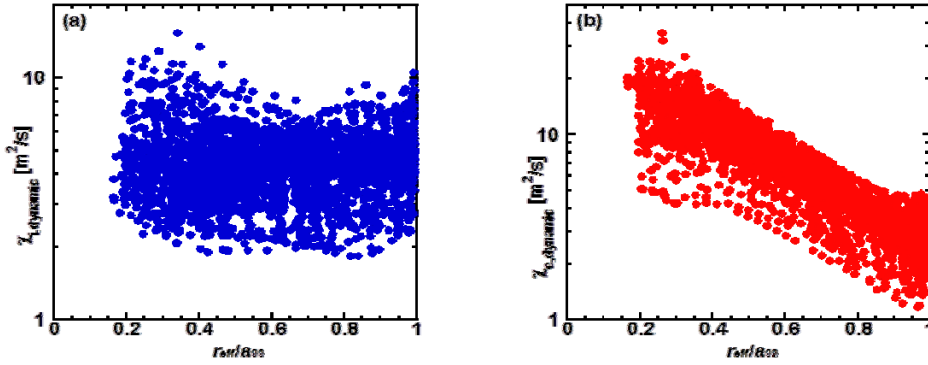


FIG. 2. Radial profiles of (a) χ_i and (b) χ_e for analysed cases.

The total number of data points of χ_i and χ_e is around 3,000, respectively.

temperature ratio (T_e/T_i). There are wide freedoms for the fitting model selection including choices and combinations of predictor variables. In addition to the above mentioned 3 variables (v_i^* , ρ_i^* , T_e/T_i), physically important variables such as E_r (radial electric field) shearing rate etc. do exist. However, the complete implementation of such variables into the analysis-database has not yet been done. Thus, let me limit myself here to propose an approach by employing available 3 variables.

Here, as a standard exercise in scaling studies, the assumed simple power-law scaling model has been transformed to the log-linear form. Multiple ordinary least squares (OLS) regression analysis has resulted in the fitting expression for $\chi_i/[T_i/(eB)]$.

$$\chi_{i,\text{fit}}/[T_i/(eB)] = 6.08 \times 10^{-9} v_i^{*-0.139} \rho_i^{*-2.29} (T_e/T_i)^{0.77} . \quad (1)$$

Figure 3 shows comparison of $\chi_i/[T_i/(eB)]$ values between TASK3D-a analysis-database and the predicted values, eq.(1). Around 3000 data points, corresponding in a wide range of T_i and radial positions, are reasonably aligned on the diagonal line in Fig. 3. An important statistical measure of the goodness of the model is the ratio R^2 of the variation explained by the model to the total variation. The obtained value is $R^2=0.84$, which is a relatively high value, indicating that the eq.(1) reasonably reproduces the response variable, that is, $\chi_i/[T_i/(eB)]$. The value of the root-mean-square-error (RMSE) is 0.27. There seems, at the most, $\pm 50\%$ difference between TASK3D-a and predicted values, seen from the horizontal width of the data cluster. This difference must be reduced, of course. However, the conventional transport model application for performance prediction is usually meant to predict for a case with a particular condition (eg., at a steady-state for certain operation scenario). On the other hand, the eq.(1)

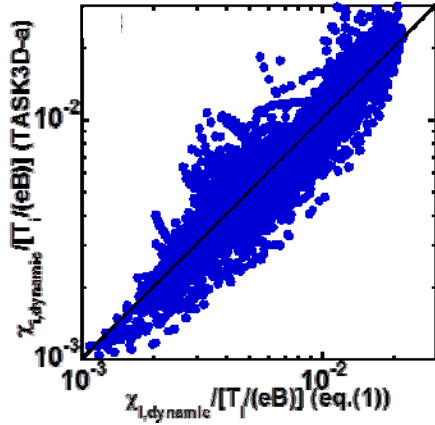


FIG. 3. (a) The comparison of $\chi_i/[T_i/(eB)]$ values between TASK3D-a analysis-database and the regression results.

covers the evolution of plasma parameters (from low- T_i to high- T_i as seen in Figure 1(a)) in high- T_i plasmas in LHD. Thus, such a deduced fitting expression can be directly implemented into the predictive simulation, so that the transport model assumption/selection (like gyro-Bohm, ion-temperature-gradient mode etc.) is no longer required. This approach may be considered to be the most relevant (“validated”) to the existing experiment database.

As for electrons, $\chi_e/[T_e/(eB)]$, the same set of predictor variables as ions, (ν_e^* , ρ_e^* , T_e/T_i), gives a fitting expression with only $R^2=0.21$. This poor confidence level of statistics may be attributed to the small range of T_e (cf., Fig. 1(b)) in the database causing smaller range of predictor variables compared to that for ions. Recently, trials have been made in LHD for increasing T_e in high- T_i plasmas (from $T_i > T_e$ towards $T_i \sim T_e$) by means of the increased available ECH power [8]. Corresponding increase of TASK3D-a analysis-database (inclusion of higher T_e cases in high- T_e plasmas) is foreseen, when it is anticipated to increase the confidence level of statistics for electrons as well.

In this proceeding, a statistical approach is proposed to predict thermal diffusivity profiles in fusion plasmas. The extensive application of the integrated transport analysis suite TASK3D-a to the LHD experiment has made this approach possible. It may be ultimately anticipated to elucidate the regression expression which is appropriate for ion and electron thermal diffusivities, separately, regardless of the confinement mode. Further application of TASK3D-a in a wider range of LHD plasmas and the resulting increase of analysis database will be performed in this direction. It should be emphasized that this approach is comprehensive for any other combinations of integrated transport analysis suits and fusion experiments.

Acknowledgements

The authors are grateful to continuous instructions from Dr. Andreas Kus (Max-Planck Institute for Plasma Physics, Greifswald) on statistical analysis. We also acknowledge TASK3D-UD (users and developers) colleagues for making extensive transport analyses of NBI-heated LHD plasmas possible. This work has been supported by the NIFS Collaborative Research Programs, NIFS11KNTT008 and NIFS11UNTT006, and by KEIN1107, NIFS/NINS (National Institutes of Natural Sciences) under the project, “Promotion of the International Collaborative Research Network Formation” for Coordinated Working Group Activity. One of authors (M.Y.) also appreciates a grant-in-aid from the Future Energy Research Association (Kyoto).

References

- [1] YOKOYAMA, M., et al., Plasma and Fusion Res. **9** (2014) 3402017 (5pp).
- [2] HIRSHMAN, S. P., and WHISTON, J.C., Phys. Fluids **26** (1983) 3553-3568.
- [3] MURAKAMI, S., et al., Trans. Fusion Technol. **27** (1995) 256.
- [4] ITER PHYSICS EXPERTS GROUPS ON CONFINEMENT AND TRANSPORT AND CONFINEMENT MODELLING AND DATABASE, Nucl. Fusion **39** (1999) 2175-2249.
- [5] YAMADA, H., et al., Nucl. Fusion **45** (2005) 1684-1693.
- [6] TAKAHASHI, H., et al., Nucl. Fusion **53** (2013) 073034 (7pp).
- [7] LEE, H., et al., Plasma Phys. Control. Fusion **55** (2013) 014011 (5pp).
- [8] NAGAOKA, K., et al., PPC/2-1, the 25th IAEA Fusion Energy Conference, St.Petersburg, Oct. 2014.